

# **Nanotribology of Metallic Glasses in Corrosive Environments**

**Dissertation**

**zur Erlangung des Grades**

**des Doktors der Naturwissenschaften**

**der Naturwissenschaftlich-Technischen Fakultät**

**der Universität des Saarlandes**

**von**

**Haoran Ma**

Saarbrücken

2021

Tag des Kolloquiums: 16. Juni 2021

Dekan: Prof. Dr. Jörn Walter

Berichterstatter: Prof. Dr. Eduard Arzt

Prof. Dr. Roland Bennewitz

Prof. Dr. Uwe Hartmann

Vorsitz: Prof. Dr. Rolf Pelster

Akad. Mitarbeiter: Dr. Anle Wang

## Zusammenfassung

Metallische Gläser (MG) sind vielversprechende Materialien für mikromechanische Systeme, in denen der mechanische Kontakt eine Kontrolle über Reibung erfordert. Mit Hilfe der Rasterkraftmikroskopie (AFM) wurden nanotribologische Experimente auf MG in korrosiven wässrigen Lösungen durchgeführt, wobei die Rolle von Oxidfilmen im Fokus stand. Eine neuartige Methode für die *in situ*-Untersuchung der Struktur der Oberflächenoxidfilme wurde entwickelt. Der Oberflächenoxidfilm weist eine zweilagige Struktur auf, die durch wiederholtes Rastern mit der AFM-Spitze nachgewiesen wurde. Die Abhängigkeit der Reibung vom elektrochemischen Potential zeigt die Wachstumsmechanismen der Oxidfilme an. Reibung und Adhäsion nach verschieden langer Immersion erlauben den Vergleich der physikochemischen Prozesse der Oberflächenauflösung an der Grenzfläche der beiden Lagen. Es wurde eine unregelmäßige stick-slip Reibung auf atomarer Skala beobachtet und auf die amorphe Natur der korrodierten Oberflächen zurückgeführt. Schließlich beschreiben wir drei verschiedene Reibungsprozesse, die mit zunehmender Normalkraft auftreten: die Abtragung der abgeschiedenen Lage bei niedrigen Auflagekräften, eine durch mechanische Spannung unterstützte Tribo-Oxidation bei mittleren Kräften sowie tribochemischen Verschleiß bei hohen Kräften. Die chemische Empfindlichkeit der nanotribologischen Studien zeigt eine neue Möglichkeit auf, grundsätzliche Mechanismen der Korrosion auf der mikroskopischen Skala zu erforschen.

## Abstract

Metallic glasses (MGs) are promising materials for micromechanical systems, where miniaturized components involving mechanical contact require control of friction. Nanotribological experiments on MGs in corrosive aqueous solutions are carried out using atomic force microscopy (AFM), focusing on the role of surface oxide films formed during corrosion. A new method is developed to study *in situ* the structure of surface oxide films. The surface oxide film has a bilayer structure as revealed by repeated scanning with the AFM tip. The dependence of friction on electrochemical potential reveals the growth mechanism of the oxide film. Friction and adhesion after different immersion times in different solutions allow to compare the physicochemical processes of surface dissolution at the interfaces of the two layers of surface films and elucidate their influence on friction. An irregular atomic-scale stick-slip friction is observed and attributed to the amorphous nature of corroded surfaces. Finally, we show three different friction processes occurring at increasing normal loads: removal of the dissolution layer at low-load regime; stress-assisted tribo-oxidation in intermediate-load regime; and tribochemical wear in high-load regime. The chemical sensitivity of nanotribology studies demonstrates a novel route to explore fundamental mechanisms of corrosion at the microscopic scale.



### **Statement on publications and contributions:**

Parts of this thesis have been published or have been submitted for publication:

1. Ma, H. R.; Bennewitz, R., Nanoscale friction and growth of surface oxides on a metallic glass under electrochemical polarization. *Tribology International* **2021**, 158, 106925.

2. Ma, H. R.; Bennewitz, R., Relationship between corrosion and nanoscale friction on a metallic glass. *Friction* (submitted)

Section 1.3.2 and Chapter 3 are duplicates of Reference 1. Chapter 4.1 is a duplicate of Reference 2. The text has been modified to fit the format of this thesis.

The contributions of the co-authors to these two publications were as follows: HM performed all experiments, analyzed the data, and wrote the manuscript draft. RB and HM designed the experiments and finalized the manuscript. RB supervised the project.

# Contents

<b>Chapter 1: Introduction.....</b>	<b>1</b>
1.1 Metallic Glasses.....	1
1.1.1 Introduction of Metallic Glasses.....	1
1.1.2 Micro/nanofabrication of Metallic Glasses.....	3
1.2 Corrosion.....	5
1.2.1 Introduction of Corrosion.....	5
1.2.2 Corrosion of Metallic Glasses.....	7
1.3 Nanotribology.....	8
1.3.1 Introduction of Nanotribology.....	8
1.3.2 Nanotribology of Metallic Glasses.....	12
1.4 Research Objectives.....	15
<b>Chapter 2: Experimental.....</b>	<b>17</b>
2.1 Atomic Force Microscopy.....	17
2.2 Force Distance Curve.....	20
2.3 Force Calibration of AFM Cantilevers.....	22
2.4 Materials.....	24
2.5 Electrochemical Cell.....	27
2.6 Experimental Procedure.....	28
<b>Chapter 3: Nanoscale Friction after Electrochemical Polarization.....</b>	<b>32</b>
3.1 Experimental Details.....	32

3.2 Results and Discussion.....	34
3.3 Conclusion.....	52
<b>Chapter 4: Effect of Corrosive Electrolytes.....</b>	<b>54</b>
4.1 The Time Evolution of Nanoscale Friction.....	54
4.1.1 Experimental Details.....	55
4.1.2 Results and Discussion.....	56
4.1.3 Conclusion.....	67
4.2 Atomic-scale Stick-slip Motion.....	69
4.2.1 Experimental Details.....	69
4.2.2 Results and Discussion.....	70
4.2.3 Conclusion.....	85
4.3 Tribochemical Processes at High Loads.....	86
4.3.1 Experimental Details.....	86
4.3.2 Results and Discussion.....	86
4.3.3 Conclusion.....	96
<b>Chapter 5: Conclusions and Outlook.....</b>	<b>98</b>
5.1 Conclusions.....	98
5.2 Outlook.....	100
<b>References.....</b>	<b>102</b>
<b>Acknowledgments.....</b>	<b>118</b>
<b>Personal Resume.....</b>	<b>120</b>

# Chapter 1: Introduction

## 1.1 Metallic Glasses

### 1.1.1 Introduction of Metallic Glasses

Metallic glasses (MGs) are amorphous structurally and typically produced by rapid cooling of a liquid melt to avoid crystallization and into a glassy state. Distinct from crystalline metals with a periodic atomic structure, the atomic arrangements in MGs present a unique structure of long-range disorder (that is, no translational periodicity) and only short- to medium-range order<sup>1,2</sup>. The formation of the first MG was reported by Duwez et al. in 1960<sup>3</sup>. They synthesized an Au-Si amorphous film by a rapid solidification technology with a cooling rate of  $10^6$  °C/s. Henceforth, numerous studies on the formation and properties of MGs have been performed accompanied by various processing routes<sup>4,5,6</sup>. A large number of glass-type alloys with high glass-forming ability were successfully found and produced in large-scale bulk form by casting processes in Fe-, Co-, Ni-, Cu-, Zr-, Mg-, Ti-, Pt-, Pd-, Au-, Ln-, Ca-, Ce-based multi-component alloy systems<sup>5</sup>. For example, Johnson et al.<sup>7</sup> developed Zr-Ti-Ni-Cu-Be MGs, which can be formed at a cooling rate of only  $\sim 1$  K/s and in a  $\sim 1$  m<sup>2</sup> glassy plate.

MGs have attracted wide scientific and technological interest because of their special combination of excellent properties including high hardness and strength<sup>8,9</sup>, high elasticity<sup>10,11</sup>, excellent corrosion<sup>12,13</sup> and wear resistance<sup>14</sup>, and good magnetic

properties<sup>15,16</sup>. Such exceptional properties are attributed to their homogeneous monolithic nature with the absence of crystal defects such as dislocation, segregation or vacancy, and grain boundaries. Unfortunately, MGs are macroscopically less plastic at room temperature<sup>9,17</sup>. Plastic deformation in crystalline metals occurs by multiplication and motion of homogeneously distributed dislocations<sup>18,19</sup>. In the case of MGs, deformation takes place inhomogeneously through plastic strains highly localized in narrow zones called shear bands. The rapid propagation of shear bands throughout a sample causes catastrophic failure<sup>20,21,22</sup>. Moreover, different from conventional metals with strain-induced hardening and annealing-induced softening, MGs present the opposite behavior, i.e. strain softening and thermal hardening<sup>23,24,25</sup>. The limited plasticity and brittle nature have seriously restricted the widespread applications of MGs.

Extensive efforts have been made to improve the plastic deformation of MGs. One strategy is to introduce MG-based composites with crystalline dendrites as reinforcements embedded in a glassy matrix that blocking shear band propagation while maintaining high strength<sup>26</sup>. Mechanical pre-treatments can also be developed effectively to strengthen the plasticity of MGs by creation of a heterogeneous microstructure, for example, shot-peening<sup>27</sup>, channel-die compression<sup>28</sup> and cold rolling<sup>29</sup>. Additionally, amorphous coatings fabricated on different substrates are thought to be an attractive way to mitigate the drawbacks and carry forward superior properties of MGs, as the brittleness of these alloys becomes non-significant when it is in the form of coating with the thickness of several hundreds micrometers<sup>30</sup>. Most

extensive use methods for preparing amorphous coatings are thermal spray-based processing and laser-based techniques.

### 1.1.2 Micro/nanofabrication of Metallic Glasses

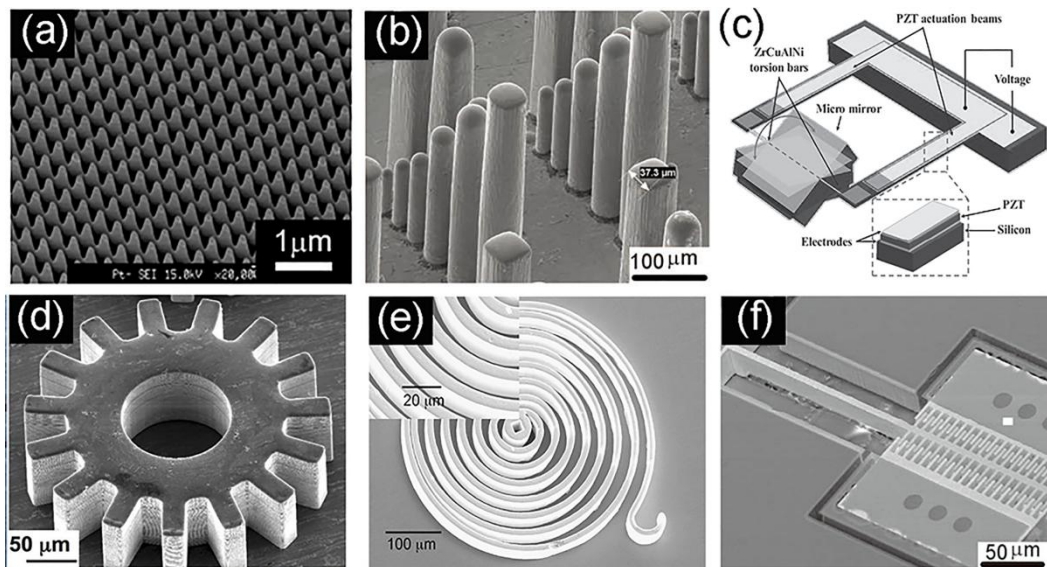


**Figure 1.1.** Examples of micro/nanofabrication of MGs: (a) nanostructured surface of Pt-based MG with periodic interval of 400 nm<sup>31</sup>; (b) micropillars of Pt-based MG with diameter of 10-50 μm<sup>32</sup>; (c) piezoelectric-driven MG microscanning mirror with a Zr-based MG as the tension bar material for mechanical motion<sup>33</sup>; (d) Zr-based MG microgear<sup>34</sup>; (e) coil-shaped Zr-based MG spring<sup>35</sup>; (f) Pt-based MG linear comb-drive actuator<sup>32</sup>.

The intensive researches on the mechanical deformation of MGs reveal that mechanical responses of MG samples are sensitive to the sample size and geometry<sup>32,36</sup>. Large tensile strains were observed for monolithic MGs with dimensions of the order of 100 nm<sup>37</sup>. Jiang et al. reported that Zr-based MG nanopillars show significant homogeneous plasticity while maintaining its high strength<sup>38</sup>. Although MGs are macroscopically less plastic than crystalline metals, their plasticity is greatly enhanced at the microscale. Moreover, MGs are

microscopically homogeneous and isotropic without grains and other crystal defects. These suggest that applications at micro- and nanometer scale would benefit the most from MGs.

The temperature interval between the glass transition and crystallization is identified as the supercooled liquid region and is a manifestation of the glass forming ability of MGs<sup>39</sup>. In this temperature region, MGs become significantly soft and show superplasticity, which can be formed very similar to plastics under comparable forming pressure and temperature, called thermoplastic forming or superplastic forming<sup>35,40,41,42</sup>. This technology allows precise and versatile replication of small features with MGs at length scales ranging from nanometers to centimeters. **Figure 1.1** presents several of recently reported MG-based micro-patterns and micro-parts. A nanoscale imprinting technology in the supercooled liquid region has been demonstrated to achieve nanotextured and multiscale patterned surfaces on MGs. **Figure 1.1a** shows a nano-imprinted pattern with periodic interval of 400 nm for Pt-based MGs<sup>31</sup>. The reflectance ratio of light on these nano-structured surfaces changes in a wide range from 1% to >50%, which is useful for optical applications<sup>31</sup>. **Figure 1.1b** presents micropillars with diameter of 10-50  $\mu\text{m}$  formed by pressing the Pt-based MG into a silicon mold<sup>32</sup>. The micropillars have been successfully commercialized as electrode materials<sup>5</sup>. MG-based microparts can also be produced by micromolding, with various generic shapes at a wide range of length scales. For example, a developed microscanner was reported with MG as the material for the moving torsion bars, which offers a large rotating angle with lower power

consumption, better sensing and actuation performance, as compared to conventional single and polycrystalline silicon<sup>33</sup>, as shown in **Figure 1.1c**. A microgear<sup>34</sup> and coil-shaped spring<sup>35</sup> of Zr-based MGs are given in **Figure 1.1d** and **e**, showing excellent mold replication and high accuracy. **Figure 1.1f** shows a MG linear comb-drive actuator<sup>32</sup>. The comb moves when applying an alternating voltage. Exhibiting homogeneous isotropic structure, superior properties over conventional materials and the exceptional thermoplastic formability, MGs are therefore considered promising materials for miniature applications in micro- and nanoelectromechanical systems (MEMS and NEMS), biomedical implants, precision microparts, surgical tools, and micromachine.

For engineering applications of MGs, friction and wear on mechanical components subjected to contact sliding are significant factors in limiting their effectiveness and durability, therefore the tribological properties of MGs are of crucial importance. Since most metals and alloys are susceptible to corrosion when exposed to environmental conditions, corrosion degradation of MGs must also be taken into account.

## **1.2 Corrosion**

### **1.2.1 Introduction of Corrosion**

Corrosion is a natural phenomenon and refers to the physical dissolution and chemical reaction between the metal and environmental medium, which causes part or



the whole of the metal to be damaged or deteriorated. Thus, corrosion is an important issue in many industrial applications of metallic materials.

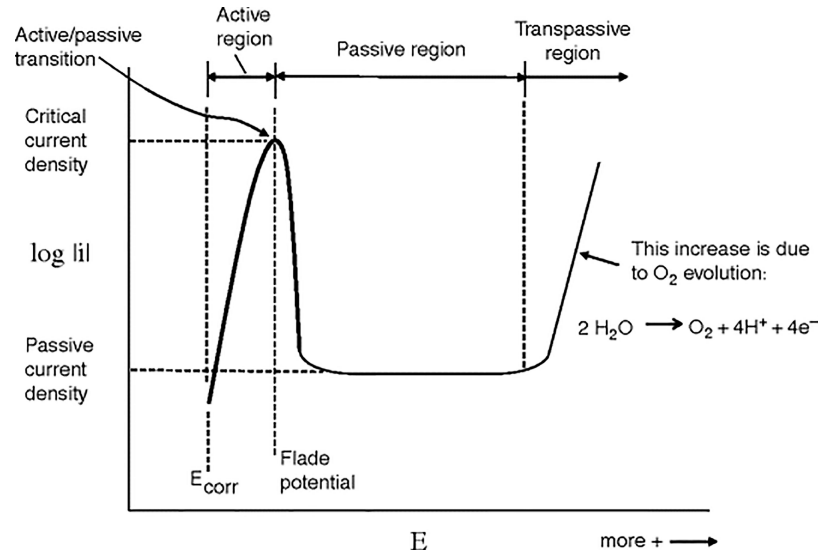


**Figure 1.2.** Typical anodic polarization curve<sup>43</sup>, determined by recording the current density  $i$  with increasing the applied electrode potential  $E$  and plotted as  $\log |i|$  versus  $E$ .

Protective oxide films form on most metal surfaces and act as a barrier to the corrosive environment, thus impeding further corrosion. This is called spontaneous passivity. Measuring the polarization curves of metals is an important method to discover the electrochemical mechanism of passivity. A typical anodic polarization curve<sup>43</sup>, recording the current density with increasing the applied potential, is illustrated in **Figure 1.2**. The curve can be divided into three regions. Firstly, as the applied potential increases, the corrosion current increases rapidly, which is called active dissolution. When the potential reaches a certain value called the Flade potential, the current rises to the maximum. As the potential becomes more positive, the current density decreases caused by the formation of the passive oxide film on the

metal surface, called active/passive transition. Then current density reaches a relatively steady value, regarded as the passive region. Further increases in potential cause a significantly increased current density, indicating the transpassive breakdown of the passive film. This increase in current density can also arise from the evolution of oxygen.

### **1.2.2 Corrosion of Metallic Glasses**

The study of formation and dissolution of passive films contributes to the understanding of corrosion mechanisms on MGs for practical applications. The passivity and breakdown behavior of MGs have been addressed in many studies. Duarte et al.<sup>12</sup> dissected a detrimental transition from Cr-controlled passivity to Mo-controlled breakdown on a Fe-based MG with near-atomistic insights. Si et al.<sup>13</sup> reported that Cr-based MGs can be passivated with a wide range of potentials even in 6 M HCl. Compared with the single crystal counterpart, passive films formed on Zr<sub>2</sub>Ni MGs were more compact and less defective<sup>44</sup>.

The passive films are known to form as a bilayer structure on many metals, with a compact, harder barrier inner layer underlying a porous, softer outer layer<sup>45,46,47,48,49,50,51,52</sup>. Wang et al.<sup>53</sup> found that passive films of Fe-based MGs in neutral solutions (Na<sub>2</sub>SO<sub>4</sub> and NaCl) consist of a bi-layer structure with a inner layer of the low-valence Fe(II), Cr(III), and Mo(IV) species and a defective outer layer of high-valence Fe(III), Cr(VI), and Mo(VI) species. Kawashima et al.<sup>54</sup> reported that the exterior part of passive films on Zr-based MGs in NaCl solutions consist exclusively

of zirconium oxyhydroxide.

## 1.3 Nanotribology

### 1.3.1 Introduction of Nanotribology

Tribology is a multi-disciplinary study of friction, lubrication and wear between interacting surfaces with relative movements. Three empirical laws of macroscopic friction are known for us:

- (1) The friction is independent of the geometric contact area;
- (2) The friction is proportional to the normal force:

$$F_f = \mu \cdot F_N \quad (1.1)$$

The proportional factor  $\mu$  is called the friction coefficient.

- (3) The friction is independent of the sliding speed.

Although the exact characteristics of the sliding surfaces are unknown, these classical friction laws can describe the properties of macroscopic tribo-systems well.

Bowden and Tabor stated<sup>55</sup> that the actual contact area of the interacting surfaces is much less than the apparent contact area (less than one ten-thousandth of the apparent area) and the friction force is proportional to the real contact surface area  $A_r$  :

$$F_f = \tau \cdot A_r \quad (1.2)$$

where  $\tau$  is the interfacial shear strength. **Figure 1.3** presents a schematics of

interacting surfaces at three different length scales<sup>56</sup>. Even if polished very carefully and made as flat as possible, almost all surfaces are rough and the contact interfaces contain a number of smaller individual asperities at the microscale. As  $F_N$  increases,  $A_r$  increases due to an increase in number and size of the contacting asperities<sup>55</sup>.

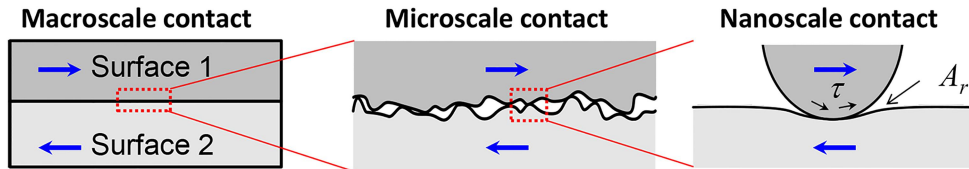


**Figure 1.3.** Schematics of interacting surfaces at the macro-, micro-, and nanoscale<sup>56</sup>.

During the last three decades, the development in scanning force microscopy and computational simulation allow scientists examine the tribological behavior of single-asperity contacts at the nanoscale (**Figure 1.3**) with extremely high resolution of force and displacement to better understand the fundamental mechanisms<sup>57</sup>. The study of tribology has evolved to the contacts of micro- and nanometre sizes, as a relatively new field called “nanotribology”.

In nanotribology, the microscopic single-asperity contacts can be considered approximatively as a sphere (single asperity) pressed against a plane surface, applied by the contact theories of Hertz, Derjaguin-Müller-Toporov (DMT), and Johnson-Kendall-Roberts (JKR) models<sup>58</sup>.

The Hertz model describes the non-adhesive elastic contact:

$$a^3 = \frac{3F_N R}{4E^*} \quad (1.3)$$

$$A_r = \pi a^2 \quad (1.4)$$

$$h = \frac{a^2}{R} \quad (1.5)$$

$$\frac{1}{E^*} = \frac{1-\nu_1^2}{E_1} + \frac{1-\nu_2^2}{E_2} \quad (1.6)$$

where  $a$  is the contact radius,  $R$  the radius of the sphere,  $h$  the penetration depth (surface deformation),  $E^*$  the effective elastic modulus of the contact,  $E_1$ ,  $\nu_1$  the elastic moduli and Poisson's ratio of the surface,  $E_2$ ,  $\nu_2$  the elastic moduli and Poisson's ratio of the sphere.

The JKR model considers adhesion inside the area of contact:

$$a^3 = \frac{3R}{4E^*} \left( F_N + 3\gamma\pi R + \sqrt{6\gamma\pi R F_N + (3\gamma\pi R)^2} \right) \quad (1.7)$$

$$F_{ad} = \frac{3}{2} \gamma\pi R \quad (1.8)$$

where  $F_{ad}$  is the adhesion force (also called the pull-off force),  $\gamma$  is the adhesion work per unit area.

The DMT model considers adhesion outside the area of contact:

$$a^3 = \frac{3R}{4E^*} (F_N + 2\gamma\pi R) \quad (1.9)$$

$$F_{ad} = 2\gamma\pi R \quad (1.10)$$

Hertz model is valid for a much lower adhesion force compared to the maximum normal force. JKR model is valid for contacts of the large sphere and soft surface with

a large adhesion, and DMT model for small sphere and stiff surface with a low adhesion<sup>58</sup>.

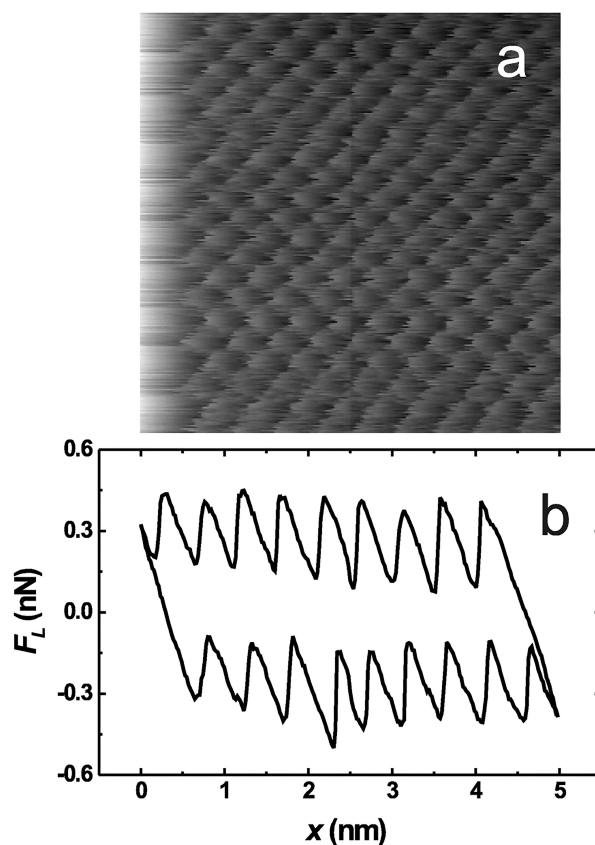


**Figure 1.4.** (a) Lateral force image of NaCl(100) measured in ultrahigh vacuum; (b) Friction loop obtained from the line profile of the corresponding trace and retrace lateral force images.<sup>59</sup>

Nanoscale single-asperity friction on well-defined surfaces can exhibit atomic-scale features. For example, **Figure 1.4a** shows a lateral force map recorded for a Si tip on the NaCl(100) surface in ultrahigh vacuum<sup>59</sup>. The map reveals the regular cubic symmetry lattice of the NaCl(100) surface. A sawtooth-like behavior is observed with the periodicity of the surface lattice, as showed in the friction loop (**Figure 1.4b**). This phenomenon is called atomic-scale stick-slip. Atomic-scale stick-slip is one of the fundamental friction processes for a single-asperity contact and

has been observed on a wide range of materials<sup>57</sup>. This phenomenon contains a wealth of physical information underlying friction, although some of it is not entirely clear. The study of stick-slip motion contributes to a deeper understanding of the origins of friction and has attracted wide interest of scientists.

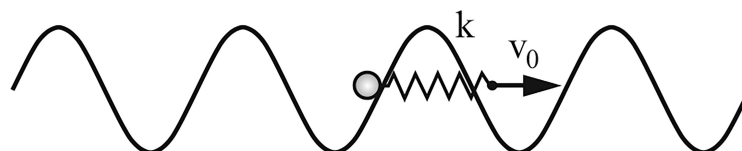


**Figure 1.5.** The Prandtl model: A point mass dragged in a periodic potential.<sup>60</sup>

The Prandtl-Tomlinson (PT) model<sup>60</sup> is widely used to explain atomic stick-slip motion, schematically depicted in **Figure 1.5**. In this model, the sliding tip is simplified as a single spring with a stiffness  $k$  pulling a point mass. The surface with periodically arranged atoms is modeled as a series of periodically-arranged energy barriers that the tip must overcome as it slides over the surface. This results in an equilibrium position (the potential minimum between atoms) for the tip, in which it remains (stick) until the surface potential has shifted due to the friction movement so that the tip suddenly jumps into the next potential minimum (slip), i.e. advances one atomic lattice position.

### 1.3.2 Nanotribology of Metallic Glasses

This section is a duplicate of the “introduction” part in the following publication with a few modifications: Ma, H. R.; Bennewitz, R., Nanoscale friction and growth of surface oxides on a metallic glass under electrochemical polarization. *Tribology*

*International* **2021**, 158, 106925.

While the macroscopic tribology of MGs has been studied extensively<sup>14,61,62,63</sup>, a detailed understanding of mechanisms of friction and wear at the microscopic length scale is still lacking, which is of great importance required for miniature applications of MGs, such as in micro- and nanoelectromechanical systems (MEMS and NEMS) (see **Chapter 1.1.2**). Togashi et al.<sup>64</sup> reported the wear resistance of micro-load bearings prepared by Ni-based MGs to be superior to steel with a four times higher durability. Comparing a Pt-based metallic glass with a Pt single crystal, Caron et al.<sup>65</sup> discovered that wear-less friction depends on chemistry through interfacial alloying, while wear is determined by structure through plasticity mechanisms. Brittle fracture was found to dominate the nanoscale scratching of Zr-based MGs in the plastic regime, where the friction coefficient increased with normal force<sup>66</sup>.

A thin oxide film with a typical thickness of a few nanometers is known to form on most MGs when exposed to environmental conditions<sup>53,67,68</sup>. With a size reduction of mechanical components into the micro- and nanometer scale and the corresponding high surface-to-volume ratio, the surface oxide layer strongly affects applications involving mechanical contact. Recent studies have addressed the role of surface oxide layers formed in ambient conditions for nanoscale friction and wear of MGs. It was discovered that the native oxide layer grown on a Ni-Nb MG can effectively reduce the wear rate<sup>69</sup>. The surface oxide layer formed upon annealing of Ni<sub>62</sub>Nb<sub>38</sub> glasses significantly increases the nanoscale friction coefficient<sup>70</sup>. The friction coefficient of



the Zr-based MG during nanoscale scratching was found to decrease with the increase of oxidation temperature<sup>71</sup>. Kang et al.<sup>67</sup> reported that the thermal growth of an oxide layer leads to a decrease in the friction coefficient compared to its native condition, where an increase in oxidation time increased the contribution of shearing and decreased the contribution of ploughing to friction.

Surface chemistry in corrosion environments also plays a crucial role for friction. Nanoscale friction on a gold surface changes dramatically upon electrochemical oxidation and fast, reversible switching between the two states of friction was achieved by potential control<sup>72,73</sup>. The friction response of a copper crystal was shown to be correlated to the compositional changes in the oxide layer with the applied potential<sup>74</sup>. Shockley et al.<sup>75</sup> reported that the anodic potential applied under potentiostatic control influences the re-passivation behavior and thereby the tribocorrosion properties of superduplex stainless steel. To the best of our knowledge, the influence of oxide layers grown under corrosive conditions on the nanoscale friction and wear of MGs has not yet been investigated. It must be considered for miniature applications of MGs exposed to wet environments containing corrosive solutes.

Tribological properties of nanometre-scale contacts can be studied by friction force microscopy (FFM) with high resolution of force and displacement<sup>76</sup>. Extensive experiments of FFM were carried out in different controlled conditions, e.g., in an electrochemical environment, and demonstrated its chemical sensitivity to the changes

in surface<sup>72,73,77,78</sup>. A large friction contrast between the native and oxidized state of gold in perchloric acid was observed by FFM<sup>72,73</sup>. Sweeney et al.<sup>77</sup> found that friction forces vary with the applied potential on gold in an ionic liquid due to the change in composition of a confined surface ion layer. FFM experiments indicated the two-phase nature of W-S-C coatings presented a two-phase structure of the coatings corresponding to nanocrystalline WS<sub>2</sub> (low-friction) embedded in the amorphous matrix of WS<sub>2</sub> and C (high-friction)<sup>78</sup>. Therefore, FFM is employed in this work as the main tool to investigate the effect of surface chemistry on friction.

## 1.4 Research Objectives

MGs are excellent materials for miniature applications in micromechanical systems, where friction and wear between the component surfaces have a significant impact on limiting their effectiveness and durability. Meanwhile, MGs are susceptible to corrosion when exposed to environmental conditions. Therefore, the objective of this work is to understand the mechanisms controlling friction and wear of MGs in corrosive environments at the microscopic scale. Towards this goal, nanotribological experimental results using FFM are structured as follows:

A thin surface oxide film (passive film) with a typical thickness of a few nanometers is known to form on MGs during corrosion. We provide a new method to investigate *in situ* the structure of passive films in aqueous solutions using FFM. Based on this method, firstly the growth mechanism of oxide films with electrochemical polarization potential and their role in nanoscale friction on MGs are

elucidated.

Then we investigate nanoscale friction of MGs after different immersion times, to clarify the correlation of corrosion with nanoscale friction. Two different corrosive solutions are selected as the test solutions, in which MG samples show completely different corrosion properties. Friction results reveal the interrelation of relevant physicochemical processes at the interfaces of oxide films and their connection with the frictional response of MGs.

To further study the fundamental mechanisms of friction on MGs in corrosive solutions, we investigate atomic-scale stick-slip processes on the corroded surfaces of MGs. Due to the amorphous nature of the corroded surfaces, friction results contribute to a deeper understanding of atomic-scale friction on amorphous surfaces.

Finally, high-load friction experiments are performed to study the effect of load on friction of MGs. We find two different load-dependent friction processes: stress-assisted tribo-oxidation and tribochemical wear. Combined with friction results above, we delineate a complete friction process on MGs in corrosive solutions with the increase in load.

## **Chapter 2: Experimental**

This chapter describes the most important basics for understanding the work. Firstly, a short introduction to the working principle of atomic force microscope (AFM) used in this work is presented. The force distance curve and the force calibration of AFM cantilevers are then explained. This is followed by the presentation of the investigated materials. After listing electrochemical cells for experiments under electrochemical conditions, the chapter concludes with a description of the experimental procedure.

### **2.1 Atomic Force Microscopy**

Binnig et al. invented AFM in 1986<sup>79</sup>, as a type of scanning probe microscopy (SPM). The great advantage of this approach is the ability to investigate different interactions, chemical or physical in nature, with spatial resolution down to the nanometer range. The scanning tunneling microscope (STM) can only examine the surface properties of electrically conductive samples, however, AFM can be used to image any kind of materials including both conductive and non-conductive samples. At present, AFM has been widely used in micromorphological characterization<sup>80</sup>, nanomanipulation<sup>81</sup>, nanofabrication<sup>82</sup>, biomedicine<sup>83</sup>, molecular mechanics<sup>84</sup> and many other fields.

Within the scope of this chapter, only a few properties of AFM are discussed, which are required to understand the experiments carried out. The basic working

principle of AFM is shown in **Figure 2.1**. An ultra-sharp tip on the free end of a flexible cantilever is touched to the sample surface. The various force interactions, both attractive and repulsive, between atoms of the tip and the surface result in a twist of the cantilever, which is measured by an optical beam deflection method. In this method, a light beam is reflected by the back of the cantilever to a position-sensitive four-quadrant photodiode detector. With the twist of the cantilever, the position of the reflected spot changes, so that the movement of the cantilever can be traced very precisely. The recorded signal by the detector is the Deflection, in volts.

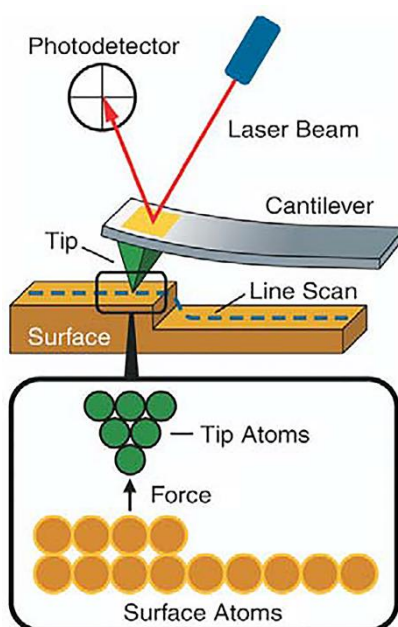


**Figure 2.1.** Schematic of the basic principle of AFM<sup>85</sup>.

In imaging, two modes of operation are commonly used in AFM: contact mode and non-contact mode (also called tapping mode). In contact mode, the tip is in continuous contact with the sample surface. The topography of the surface is obtained via maintaining a constant normal deflection of the cantilever according to the

Setpoint voltage set by the user and the normal force applied on the surface thus remains constant. A deflection of the cantilever from its equilibrium position can take place in different directions, for example, vertical to the cantilever due to interaction forces in the normal direction and perpendicular to the long axis of the cantilever as a result of the lateral friction force. Therefore, the contact mode AFM can simultaneously monitor the normal force and record the lateral friction force, which thus is also known as “Friction force microscope (FFM)” or “Lateral force microscope (LFM)” in the field of nanotribology. These terms basically refer to the same instrument. On the other hand, in tapping mode, the cantilever is driven to oscillate, typically in sinusoidal motion, at or near one of its resonance frequencies, and periodically contacts with the sample surface. Aside from the topography of the sample surface, the amplitude and phase of the oscillating cantilever can be collected simultaneously, which may highlight physical properties that are not readily discernible in the topography image.

In this work, an Agilent 5500 AFM is used for all experiments, as shown in **Figure 2.2**. It is specially designed for experiments in different gases and liquids. For this purpose, it offers a closed environmental chamber, which allows imaging in controlled atmosphere. The sample is mounted on a sample plate and then inserted into this chamber. The entire measurement setup is located on a granite block, which hangs on elastic ropes to decouple mechanical vibrations. Further disturbances due to vibration, air turbulence and acoustic noise are reduced by a foam-lined isolation chamber. The video system can view the cantilever and sample and allows us to locate

regions of interest on the sample. A scanner with a maximum scan area of  $10\ \mu\text{m} \times 10\ \mu\text{m}$  is used (**Figure 2.2b**). The cantilever is secured via a spring clip on the nose assembly. Important components such as superluminescent diode and piezo elements are integrated into the scanning head. All components in this design are located above the sample and the risk of damage to components due to leaking liquid is avoided. In addition, a potentiostat is integrated in this system, which controls and records the electrochemical potential and current.

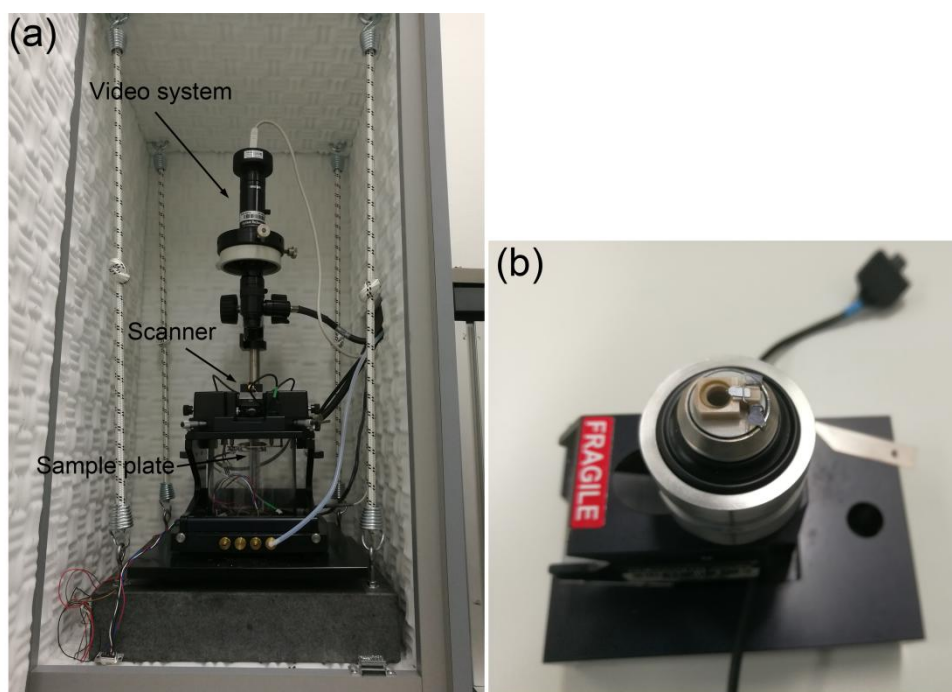


**Figure 2.2** (a) Agilent 5500 atomic force microscope; (b) AFM scanner.

## 2.2 Force Distance Curve

The distance dependency of the force is determined in the force distance (FD) curve. At the beginning of a FD measurement, the tip is placed with large tip-surface separation where there is no interaction between them (equilibrium state). The AFM

tip is then approached to the surface and retracted, and the deflection of the cantilever is recorded simultaneously. This generates a plot of the cantilever deflection signal (normal force) against the tip-sample displacement. **Figure 2.3** presents a typical FD curve, which is recorded on a MG sample in air. The red curve is the approaching portion, and the blue curve is the retraction portion.

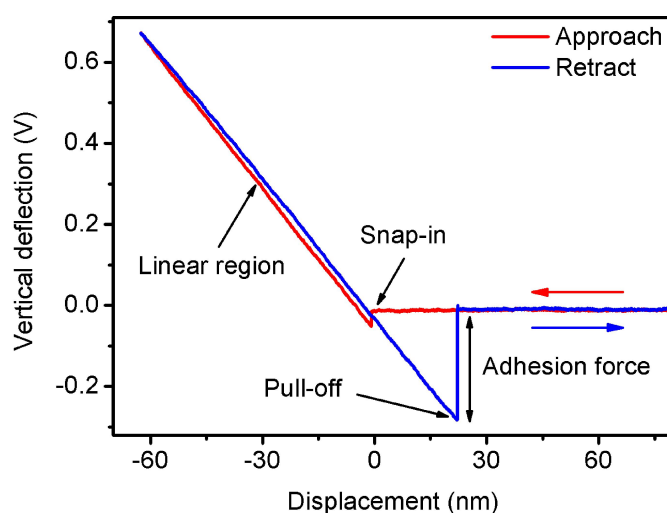


**Figure 2.3.** A typical force distance curve measured on  $Zr_{63}Ni_{22}Ti_{15}$  MG ribbon in air.

When the tip and the surface come close enough, the attractive force causes the cantilever to press on the surface associated with a sudden vertical jump in the FD curve, which is called snap-in or jump-to-contact (indicated by the arrow). The cantilever is deflected in the direction of the sample and they come into contact. As the cantilever approaching the surface, the deflection of the cantilever increases. The inverse slope in this linear region is used as the sensitivity in the conversion of the photodiode signal into a force (see **Chapter 2.3**). Then the cantilever retracts from the surface and the cantilever deflection decreases. The tip remains in contact with the



surface until the restoring force of the cantilever exceeds the attractive interactions. At this moment, there is another sudden jump in the FD curve (pull-off event) corresponding to the contact separation. The numerical value of the adhesive force (or pull-off force) can be determined as the absolute force difference between the pull-off event and the equilibrium state. The cantilever returns to its undeflected state, in which it remains with further withdrawal.

The occurrence of certain interactions depends largely on the environmental conditions. The hysteresis caused by attractive interactions in FD curves in liquids is much weaker than that in air. The reason for this behavior is the absence of capillary force and a weakening of van der Waal's force. All measurements in this work take place in aqueous solutions.

### 2.3 Force Calibration of AFM Cantilevers

A reliable determination of the force constants of AFM cantilevers is of primary importance in AFM applications. We adopt the beam geometry method<sup>76</sup> to calibrate the force constants of cantilevers experimentally. The normal spring constant  $k_N$  and the lateral spring constant  $k_L$  of a cantilever are given by:

$$k_N = \frac{Ewt^3}{4l^3} \quad (2.1)$$

$$k_L = \frac{Gtw^3}{3h^2l} \quad (2.2)$$

Where  $w$  is the width,  $l$  the length,  $t$  the thickness,  $h$  the height of the cantilever and  $E$

the Young's modulus,  $G$  the shear modulus of the material. The resonance frequency  $f$  of the cantilever at the first normal oscillation mode measured in air was used to calculate the cantilever's thickness  $t$  :

$$t = \frac{2\sqrt{12}\pi}{1.875^2} \sqrt{\frac{\rho}{E}} fl^2 \quad (2.3)$$

where  $\rho$  is the mass density. In the case of silicon,  $E = 1.69 \times 10^{11}$  N/m<sup>2</sup>,  $G = 0.68 \times 10^{11}$  N/m and  $\rho = 2330$  kg/m<sup>3</sup>.

The resonance curve of the cantilever, which involves the dependence of the amplitude upon the excitation frequency, is used to identify the free resonance frequency  $f$ . The AFM can record the resonance curve by deliberately exciting the cantilever with sweeping through a range of frequencies. Cantilever dimensions (width  $w$ , length  $l$  and height  $h$ ) are obtained from the manufacturer. The Sader method is another common calibration method<sup>86</sup>. In this method, the force constants are calculated from the resonance frequency  $f$  and quality factor  $Q$  of the cantilever, determined by the cantilever thermal noise spectrum. We have checked that the calibrated force constants are similar using both methods, which confirms the accuracy of the beam geometry method in this work.

The cantilever deflection is first measured and stored as a voltage in volts, due to the way in which the AFM works (see **Chapter 2.1**). The recorded voltage signal is then converted to nanometers by the sensitivity of the photodetector  $S_N$ , which is calculated as the slope of the linear region in a FD curve (indicated in **Figure 2.3**).

The inverse slope of the curve is given in a unit of nm V<sup>-1</sup>. The voltage is converted into a force in the unit of nN for the normal force  $F_N$  and the lateral force  $F_L$  according to the formulas:

$$F_N = S_N \cdot V_N \cdot k_N \quad (2.4)$$

$$F_L = \frac{3}{2} \cdot \frac{h}{l} \cdot S_N \cdot V_L \cdot k_L \quad (2.5)$$

where  $V_N$  and  $V_L$  are the normal and lateral voltage signal of the photodiode. After the determination of the sensitivity of the system and the spring constants of the cantilever, the voltage signals of the photodiode can be translated into the normal and lateral force. In this work, the series of friction experiments are performed with the same cantilever and the same optical alignment, so that the influence of calibration errors can be avoided as much as possible for the relation between friction results.

## 2.4 Materials

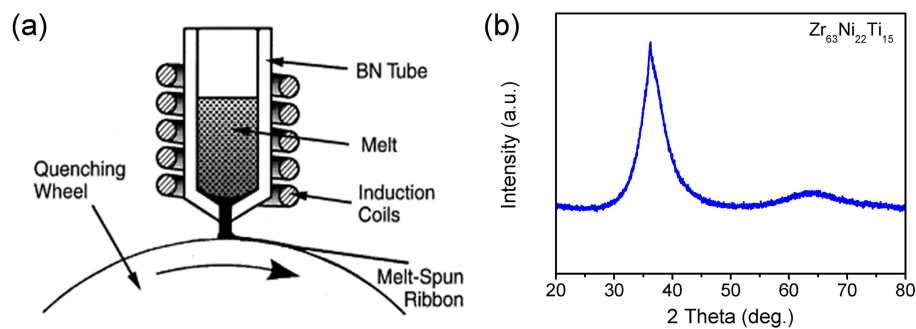


**Figure 2.4.** (a) schematic view of the melt-spinning technique<sup>87</sup>; (b) XRD patterns of Zr<sub>63</sub>Ni<sub>22</sub>Ti<sub>15</sub> MG ribbon.

Zr-based MGs are one of the most important MGs for practical use. The

outstanding glass forming ability, excellent mechanical properties and unique superplastic forming ability<sup>5,9,42</sup>, make Zr-based MGs ideal candidates for miniature applications. At present, micro/nanofabrication of Zr-based MGs has been addressed in many studies<sup>32,35,41,42</sup>.

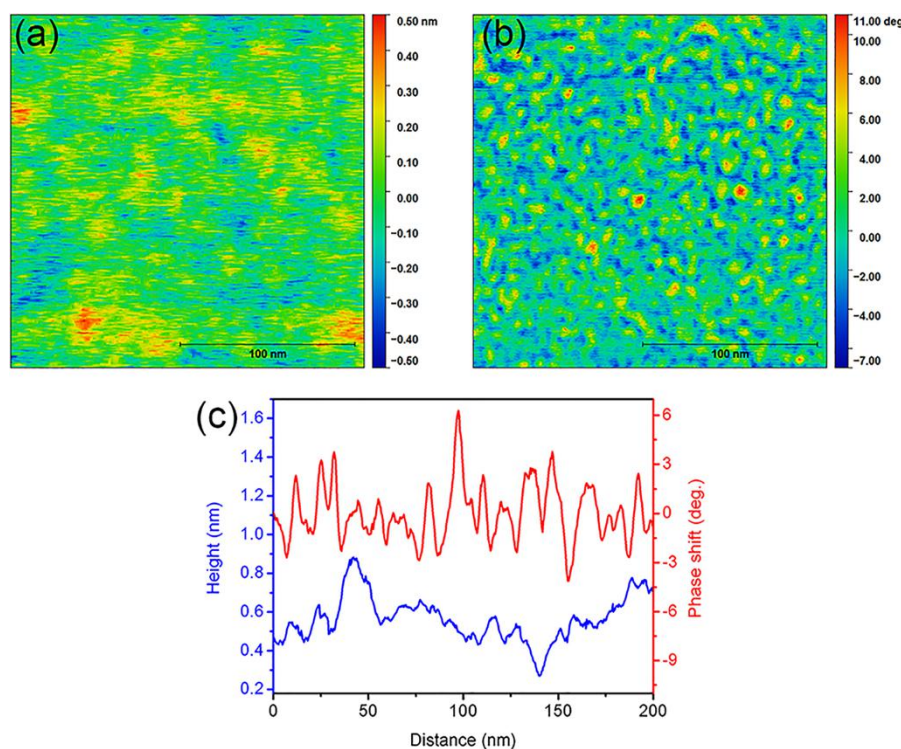


**Figure 2.5** (a) Topography and (b) phase shift image of ZrNiTi MG ribbon in the air; (c) line-scan results obtained at the same area of (a) and (b).

MG ribbons with the chemical composition of  $Zr_{63}Ni_{22}Ti_{15}$  (ZrNiTi) in at. %, are selected as the model material. They were produced by the single roller melt-spinning technique provided by the *Physics Institute at the University of Basel (Switzerland)*. The melt-spinning technique has been one of the most commonly used methods of rapid solidification processing to synthesize MGs<sup>87</sup>, as shown in **Figure 2.4a**. In a typical melt-spinning process, a rotating wheel is cooled internally, usually by water

or high thermal conductive materials, such as copper. A thin stream of molten metal liquid is then dripped onto the surface of the rotating wheel and the heat of the molten liquid is absorbed into the roller causing rapid solidification and forming a thin amorphous ribbon. The X-ray diffraction with Cu K $\alpha$  radiation (XRD, D8 Advance, Bruker AXS, Germany) verified the amorphous structure of the ribbons, as shown in **Figure 2.4b**.

The nano-scale structural heterogeneity of MGs can be mapped experimentally by amplitude-modulation dynamic atomic force microscopy (AM-AFM)<sup>88</sup>. In AM-AFM<sup>89</sup>, the cantilever oscillation is driven at a fixed amplitude and a fixed frequency. When the tip scans across a surface, the tip-surface interactions cause a change in both the amplitude and phase (relative to the driving signal) of the cantilever. These changes can be related to variation in the energy dissipated in a local region of the sample surface. The topography and phase shift image simultaneously measured on the free surface (in contrast to the copper wheel-contacted surface) of ZrNiTi MG ribbon are presented in **Figure 2.5**. **Figure 2.5a** shows that the free surface is flat with surface roughness less than  $\sim 1$  nm, which can also be revealed by the line-scan height profile in **Figure 2.5c** with a  $\sim 0.7$  nm height variation. The large variation of phase shift in **Figure 2.5b** indicates the structural heterogeneity of the MG sample. **Figure 2.5c** displays the line-scan profiles across the same area, from which it can be easily seen that, the phase shift is independent of the surface topography and mainly reflects intrinsic surface properties. The copper wheel-contacted surfaces of MG ribbons are visually rough. Therefore, the free

surfaces of MG ribbons with sub-nano-scale roughness are directly used for AFM measurements without any polishing or surface processing.

## 2.5 Electrochemical Cell

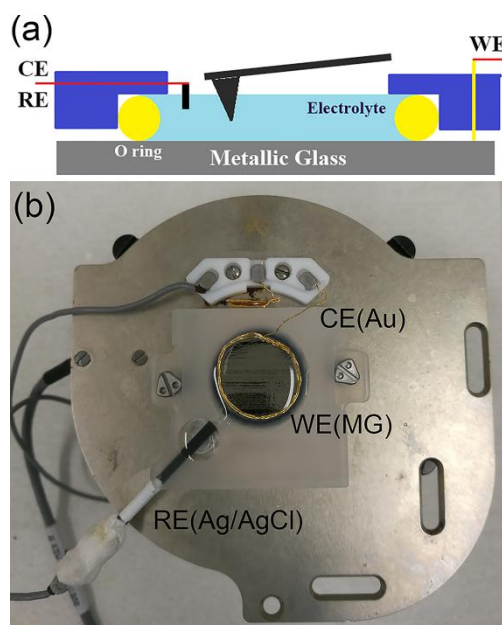


**Figure 2.6** (a) Schematic cross-sectional view and (b) optical image top view of electrochemical AFM cell with three-electrode arrangement: the MG ribbon served as the working electrode (WE), a Ag/AgCl electrode as the reference electrode (RE) and a Au wire as the counter electrode (CE).

A home-made electrochemical liquid cell with three-electrode setup is employed in all AFM measurements, as shown in **Figure 2.6**. The MG ribbon is electrically connected to a Au wire on the bottom of the cell, as the working electrode (WE). The exposure area of the MG ribbon is  $\sim 2.0 \text{ cm}^2$ . A miniature Ag/AgCl electrode is used as the reference electrode (RE). To accommodate the reference electrode, the cell has a separate, smaller electrolyte compartment, which can be separated from the main compartment via a channel. A Au wire with a purity of 99.9 % is located within the electrolyte, served as the counter electrode (CE). It encompasses as much of the inner

rim of the cell as possible but does not contact the sample surface. This three-electrode setup offers the advantage that the potential can be precisely determined, because the current flows through the working electrode and the counter electrode, while the reference electrode remains currentless due to its high intrinsic resistance. The electrochemical potential can only be specified relative to the reference electrode. The cell is made from chemical-resistant polychlorotrifluoroethylene (PCTFE). A Viton O-ring gasket is used to avoid leakage.

## **2.6 Experimental Procedure**

When aiming for precise measurements, any form of contamination can have detrimental consequences. Before starting an experiment, it is therefore necessary to ensure all the utensils used are thoroughly cleaned. Au wires, tweezers and the AFM cell are boiled in Milli-Q water for about 30 minutes and dried under a nitrogen flow. The sample plate and the nose assembly of AFM scanner are cleaned with isopropanol and Milli-Q water. The MG ribbon is ultrasonically cleaned in Milli-Q water, isopropanol and Milli-Q water sequentially (each for 10 min), then dried under a nitrogen flow and mounted into the AFM cell. Then the counter and reference electrodes are fixed, and the electrolyte is added to the cell. The liquid level is roughly equal to the height of the cell, so that the cantilever can be completely immersed into the electrolyte. This process must be carried out as soon as possible, as the sample surface may adsorb impurities on the laboratory air. Gloves are worn at all times.

All experiments are carried out at room temperature. At the beginning of each

experiment, the resonance curve of the cantilever in air is recorded to identify the free resonance frequency of the first normal oscillation mode, in order to yield the spring constant of the cantilever. After the tip has reached the sample surface, FD curves are measured to determine the sensitivity of the photodetector. In order to exclude topographical effects, the experiments are carried out on atomically smooth surfaces with rms roughness less than 1 nm as far as possible.

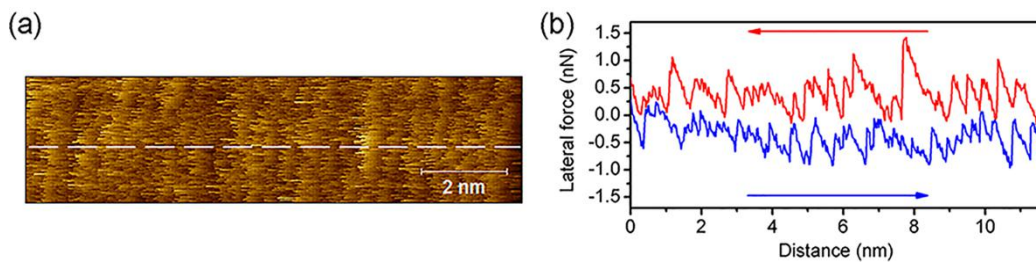


**Figure. 2.7.** (a) Lateral force image of ZrNiTi MG in 0.2 M phosphate buffer (pH~7) (retrace); (b) Friction loop obtained along the line shown in (a), reflecting a stick-slip pattern. Arrows indicate the scan direction.

During the tip scanning over the sample surface, two images are simultaneously recorded side-by-side. One is measured as the lateral deflection signal during the trace (left-to-right tip motion) of each line in the raster scan, and the other is mapped during retrace (right-to-left tip motion). A typical example of a silicon tip scanning on ZrNiTi MG ribbon is shown in **Figure 2.7a**. **Figure 2.7b** displays a friction loop, enclosed by the trace and retrace lateral signals obtained along the line in **Figure 2.7a**. The actual friction force  $F_f$ , as a measure of the dissipated energy, is determined by the formula:

$$F_f = \frac{F_{L,retrace} - F_{L,trace}}{2} \quad (2.6)$$



where  $F_{L,trace}$  and  $F_{L,retrace}$  is the lateral force in the trace and retrace direction, respectively. The average lateral force can be calculated according to Eq. (2.6) for this line. The determination of the friction force of an entire LFM image is carried out over all rows of the image as the average value of all lines. The friction loop in **Figure 2.7b** exhibits an atomic stick-slip pattern.

**Table 2.1.** Information about cantilevers used in this work from the manufacturer.

Type	Tip	Tip Radius	Force Constant	Manufacturer
PPP-CONT	Highly doped Si	< 10 nm	~ 0.2 N/m	Nanosensors
CDT-FMR	Diamond Coated	100-200 nm	~ 6.2 N/m	Nanosensors

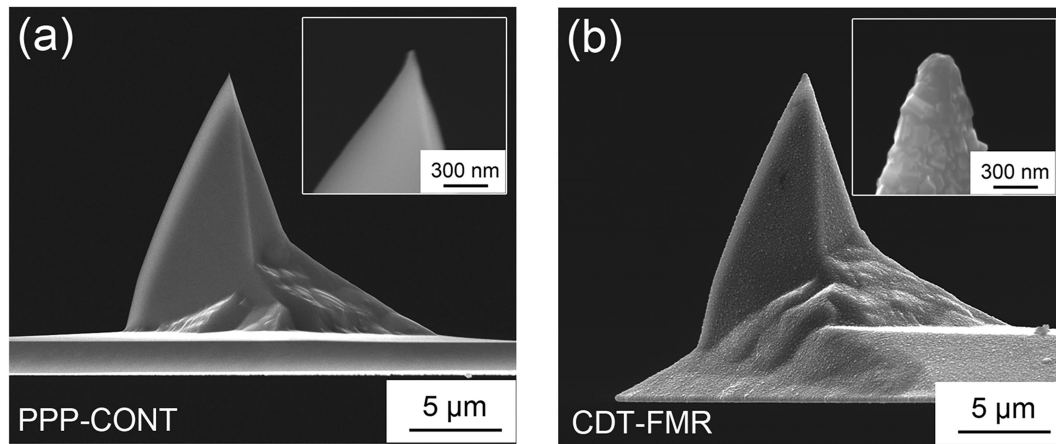


**Figure 2.8.** SEM images of different types of AFM cantilevers used in friction measurements: (a) PPP-CONT; (b) CDT-FMR. The insets show the magnified images of the tips.

Two types of AFM cantilevers are used in friction measurements. The information about AFM cantilevers obtained from the manufacturer is given in **Table 2.1**. **Figure 2.8** presents typical images of the side view of unused AFM cantilevers by scanning electron microscopy (SEM). The insets show the magnified images of the

tips. The tip radius can be estimated based on these figures. No contamination from storage is visible.

After the experiments, the individual elements such as Au wires, the AFM cell, the sample plate and the nose assembly of AFM scanner are again thoroughly cleaned. The Au wires are stored in isopropanol to avoid contamination.

## **Chapter 3: Nanoscale Friction after Electrochemical**

### **Polarization**

The surface oxide film strongly affects the friction behavior of micromechanical components subjected to contact sliding. As discussed in the first chapter, the influence of oxide films grown under corrosive conditions on the nanoscale friction of MGs has not yet been investigated. In this Chapter, we investigated the temporal development of friction on oxidized surfaces of MGs after potentiostatic polarization by electrochemical atomic force microscope (ECAFM). Through these studies, we aim to understand the structure of oxide films on MGs in corrosive environments and their role in nanoscale friction. Results for different polarization potentials were compared to elucidate the connection between friction and growth mechanisms of surface oxide films.

This chapter is a duplicate of the following publication with a few modifications:  
Ma, H. R.; Bennewitz, R., Nanoscale friction and growth of surface oxides on a metallic glass under electrochemical polarization. *Tribology International* **2021**, *158*, 106925.

### **3.1 Experimental Details**

ZrNiTi MG ribbons were selected as the experimental material (see **Chapter 2.4**). All electrochemical and friction experiments were performed in 0.2 M phosphate buffer ( $\text{Na}_2\text{HPO}_4 + \text{NaH}_2\text{PO}_4$ , pH~7) at room temperature with an Agilent 5500 AFM.

A home-made electrochemical cell with three-electrode arrangement (see **Chapter 2.5**) was employed. Polarization curves were recorded by sweeping the potential from -0.5 to 1.5 V at a sweep rate of  $1.0 \text{ mV s}^{-1}$ .

Each series of friction experiments was started by immersing a new sample into the solution for 1 h equilibration at open-circuit potential (OCP). Prior to the friction measurements, each sample was polarized at a constant potential (0.2, 0.6, 1.0 or 1.5 V, respectively) for 80 minutes to produce an oxide film on the surface. Then the potential control was disconnected, and the friction measurements were carried out at OCP on the oxidized surface with the oxidized tip (radius of  $\sim 25 \text{ nm}$ ) of a single crystalline Si cantilever (PPP-CONT, see **Chapter 2.6**). The friction force was recorded by repeatedly scanning the AFM tip over a  $1.0 \times 0.125 \text{ }\mu\text{m}^2$  area (64 lines per scan, 16 scan cycles) at a constant normal load and sliding velocity of  $8.0 \text{ }\mu\text{m s}^{-1}$ . These measurements were repeated with varying normal loads on different surface areas. Each series of friction measurements on the oxidized surface after polarization at a selected potential were carried out on a new sample surface. For comparison, the series of friction experiments was also performed on the original sample surface without applying an oxidizing polarization potential. For selected experiments, the AFM tips were analyzed by scanning electron microscopy (SEM) after friction experiments. No tip wear was noticed within the resolution of the SEM.

### 3.2 Results and Discussion

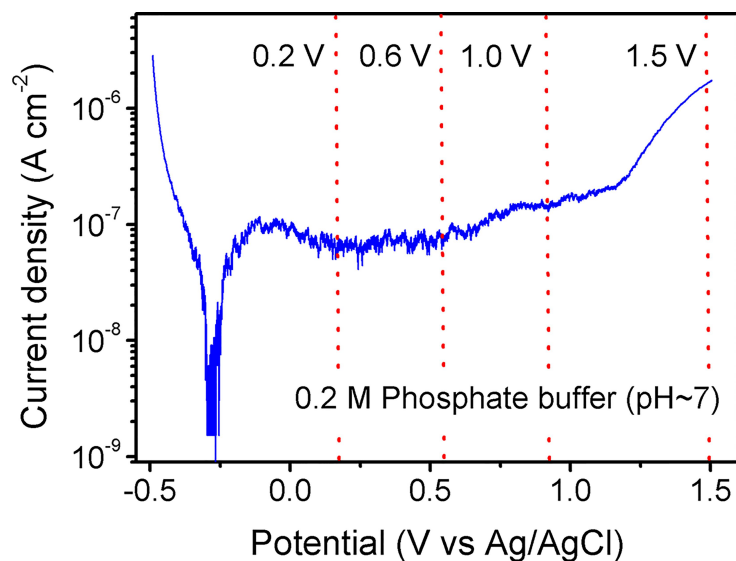


**Figure 3.1.** Potentiodynamic polarization curve of ZrNiTi MG in 0.2 M phosphate buffer (pH~7) recorded in the ECAFM cell. The dotted lines indicate the film-formation potentials chosen for friction experiments.

**Figure 3.1** presents the potentiodynamic polarization curve of ZrNiTi MG in 0.2 M phosphate buffer (pH~7) recorded in the ECAFM cell. The sample was passivated with a wide passivation region ranging from -0.05 to 1.2 V. The passivation region is identified by a low and approximately constant current density when increasing the potential. A protective passive oxide film is formed on the sample surface and acts as a barrier separating the substrate from oxygen and corrosive ions in the chemically aggressive aqueous environment and, consequently, reduces the corrosion rate. The film-formation potentials selected for friction experiments are marked with dotted lines in the polarization curve. The values of 0.2, 0.6 and 1.0 V are in the passivation region. For the value of 1.5 V, the transpassive breakdown of the passive film is reflected by a sharp increase of the current density.

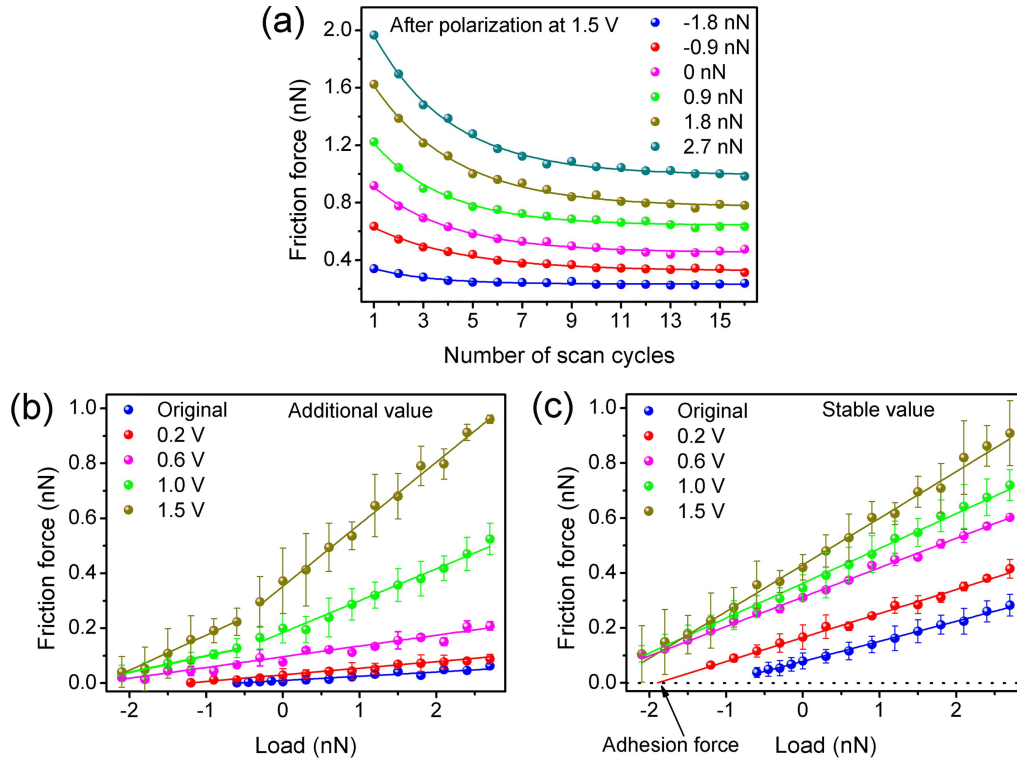


**Figure 3.2.** (a) Friction force as a function of number of scan cycles for the oxidized surface of ZrNiTi after polarization at a film-forming potential of 1.5 V in 0.2 M phosphate buffer. The smooth curves are fits of Eq. (3.1) to the data. (b) additional value and (c) stable value of friction force as a function of the load applied to the AFM tip during the repetitive scans for the surface oxidized at different film-forming potentials. Solid lines are linear fits and data of the original surface are shown for comparison. Negative forces were applied to realize low effective load on the contact by partial compensation of the tip-surface adhesion.

The friction force on the oxidized surface after polarization at 1.5 V is shown in **Figure 3.2a** as a function of the number of scan cycles at different normal loads. Each data point is the average value of a friction force map ( $1.0 \times 0.125 \mu\text{m}^2$ ). The friction force decreases with the number of scan cycles and approaches a stable value at all loads. Similar results for the decay of friction are also obtained for the original surface and for surfaces oxidized at polarization potentials of 0.2, 0.6 and 1.0 V. Please note

that the total normal force acting on the tip-surface contact is the sum of the applied normal force derived from the cantilever bending and the tip-surface adhesion force. In order to access a low-load regime for imaging or friction measurements, adhesion forces were partially compensated by applying a negative normal force.

The decay of friction force with the number of scan cycles can be described by the following equation:

$$F = F_{stable} + F_{add} e^{-\frac{N-1}{\nu}} \quad (3.1)$$

where  $F$  is the friction force,  $F_{stable}$  is the stable value of friction force which is approached after many scan cycles,  $F_{add}$  is the additional friction force at the beginning of each series,  $N$  is the number of scan cycles, and  $\nu$  is the characteristic number of cycles for the decay of friction force. The friction force for the 1<sup>st</sup> scan cycle ( $N = 1$ ) is given by the initial value:  $F_{initial} = F_{stable} + F_{add}$ .

The additional and stable value of friction force obtained from curve fits of Eq. (3.1) are plotted against the load applied to the AFM tip during the repetitive scans for the surface oxidized at different film-forming potentials in **Figure 3.2b** and **c**. After polarization of 1.5 V, for the additional value, two distinct linear regimes of increase of the friction force with increasing load could be identified. The corresponding friction coefficients are calculated as slopes of linear fits of the data. The friction coefficient is  $\mu_1 = 0.13$  in the low-load regime (-2.1 to -0.6 nN) and  $\mu_2 = 0.23$  in the high-load regime (-0.3 to 2.7 nN). Similarly, Caron et al.<sup>69</sup> reported two clearly

separated linear regimes of friction force versus load on a Ni-Nb MG with an air-formed native oxide layer, explained by indentation of the tip through the oxide layer and direct sliding contact between the AFM tip and MG substrate in the high-load regime. We attribute the difference in the friction coefficient between two load regimes to the different contact positions of the tip. In the high-load regime, the tip fully penetrates the outer layer of the oxide film and slides on the inner layer. We will discuss these attributions in detail below. Two distinct linear regimes are also found for a film-forming potential of 1.0 V. For the original surface and film-forming potentials of 0.2 and 0.6 V, only one single linear regime is observed. For the stable friction values, there is no difference between the friction coefficients of the two load regimes but one linear increase at all film-forming potentials.

After the 16 scan cycles, each slide track was imaged by subsequently scanning a wider area of  $2 \times 0.5 \mu\text{m}^2$  at a velocity of  $4 \mu\text{m s}^{-1}$  and a low imaging load. **Figures 3.3a and b** display the topography and friction force images recorded on the surface oxidized at 1.5 V after exposing the central area to 16 scan cycles at a normal load of 2.7 nN. **Figure 3c and d** show cross section of the topography and friction image corresponding to the lines drawn in **Figure 3a and b**. The topography image in **Figure 3.3a** was recorded at an imaging load of -2.4 nN. There is a noticeable difference in height between the central slide track and the surrounding area with pile-up of displaced materials on both sides of the track. The depth of the slide track is  $\sim 0.23$  nm extracted from the line-scan height profile in **Figure 3.3c**. We conclude that during the repetitive scanning of the friction experiment, an atomically thin layer of material



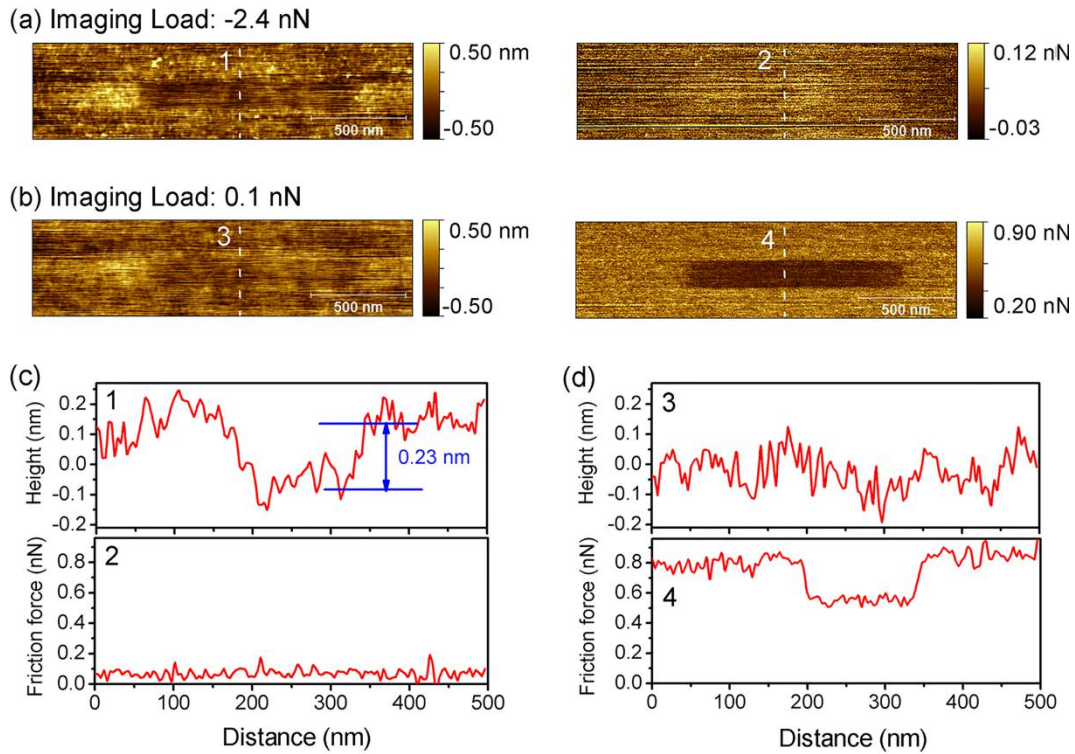


**Figure 3.3.** (a) and (b) AFM topography (left frame) and friction force (right frame) images recorded on the oxidized surface of ZrNiTi MG after polarization at 1.5 V and after scanning the central area ( $1 \times 0.125 \mu\text{m}^2$ ) 16 times at a normal load of 2.7 nN (imaging load: (a) -2.4 nN; (b) 0.1 nN). (c) and (d) Cross section of the topography and friction image corresponding to the lines drawn in (a) and (b).

was removed from the surface. Results of imaging the slide track and its surrounding area depend critically on the imaging load. When increasing the imaging load to 0.1 nN (**Figure 3.3b**), position and depth of the slide track become unclear in the topography image. However, there is now a significant contrast between the central and surrounding area in the friction force image, indicating the existence and position of the slide track. The line-scan friction profile in **Figure 3.3d** reveals that the friction force on the slide track is lower than that on the surrounding area, though the height difference between them cannot be detected in the height profile. These results

indicate that the removal of a compliant, ultrathin oxide layer leads to the decrease of friction force observed in **Figure 3.2a**. At low imaging load (**Figure 3.3a**), we observe a height difference between the previously scanned area and surrounding area but no friction contrast. The lack of friction contrast can be understood considering the extremely low imaging load which makes it difficult to discern the difference in friction. There is a friction contrast at higher imaging load (**Figure 3.3b**), but no height contrast. The lack of height contrast can be understood as penetration of the AFM tip into the soft layer surrounding the slide track. These observations will be discussed in more detail below.

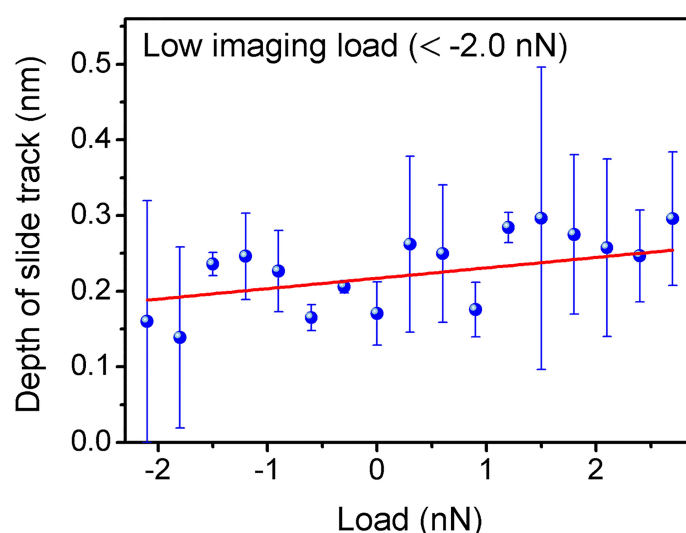


**Figure 3.4.** Depth of slide track as a function of the load applied to the AFM tip during 16 repetitive scans. Depth data were extracted from images recorded at low imaging loads below -2.0 nN.

The depth of slide track after 16 repetitive scans is plotted as a function of the applied normal load in **Figure 3.4**. The depth data was extracted from images recorded at low imaging loads below -2.0 nN, like the one shown in **Figure 3.3a**. The

thickness of the removed layer depends weakly on the applied load and increases from 0.18 nm for repeated friction experiments at low load to 0.24 nm for those at high load. Furthermore, the stable friction value is always higher than the friction force of the original surface (**Figure 3.2c**). We conclude that the surface, which is scanned by the tip when the friction reaches its stable value, is not the original surface of the MG substrate. In other words, the scanning tip does not remove the entire oxide film. The passive films on many metals and alloys are known to have a bilayer structure with a compact, harder barrier inner layer underlying a porous, softer outer layer<sup>46,47,48,49,50,51,52,53,90,91,92,93,94</sup>. Corrosion resistance is provided mainly by the continuous inner layer<sup>51,90,92,93,94</sup>, normally composed of the low-valence insoluble oxide species<sup>46,47,48,49,50,52,53,91,93</sup>. The outer, non-protective layer exhibits a porous structure formed through the mutual dissolution-precipitation processes of the inner oxides and substrate<sup>46,47,50,51,90,91,92,93</sup>, usually comprised of hydrated high-valence oxides and hydroxides<sup>46,47,49,50,52,53,91,93</sup>. Our friction results are in full agreement with a bilayer structure for the oxide film on ZrNiTi MG, depicted schematically as the inset in **Figure 3.5a**. The deposited precipitates that form the outer layer are bound only weakly to the surface, as compared to the inner oxides which grow through direct oxidation of the MG substrate. As scanning proceeds, the outer, highly porous layer is ploughed off by the tip while the inner layer remains on the surface. Given the two distinct linear regimes and the different imaging results of the slide track, we further conclude that the tip penetrates the outer layer and contacts the surface of the inner layer in the high-load regime while the tip does not fully penetrate the outer

layer in the low-load regime. This difference in penetration depth causes the difference in the friction coefficients in **Figure 2b**.

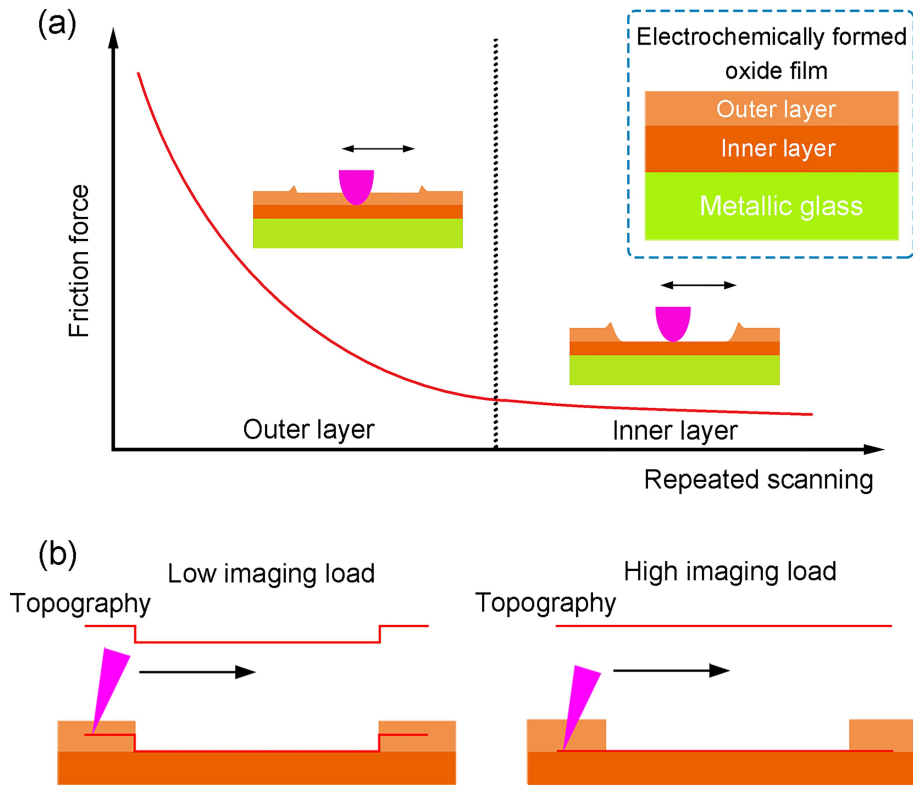


**Figure 3.5.** (a) Schematic explanation of the decrease of friction as a function of number of scan cycles. The outer layer with its additional friction is removed in the course of repeated scanning. The inset shows the bilayer structure of the electrochemically formed surface oxide film. (b) Illustration of the influence of the imaging load on the height measurement of slide tracks.

Based on the discussion above, **Figure 3.5a** provides a schematic explanation of the development of friction during continuous scanning. In our experiments, the outer layer is susceptible to removal by the sliding tip, while the inner layer is ploughing-resistant and remains stable under the scanning tip. In the 1<sup>st</sup> scan cycle, the tip penetrates the outer layer and slides on the inner layer. The total friction force is the sum of two contributions:  $F_{inner\ layer}$  is the force required to shear the contact

between the tip and inner layer;  $F_{outer\ layer}$  is the ploughing force required to displace the outer layer ahead of the sliding tip. Eq. (3.1) can now be interpreted as follows:

$$F = F_{inner\ layer} + F_{outer\ layer} \quad (3.2)$$

$$F_{outer\ layer} = F_{outer\ layer}^{N=1} e^{-\frac{N-1}{\nu}} \quad (3.3)$$

where  $F_{outer\ layer}^{N=1}$  is the ploughing force during the 1<sup>st</sup> scan cycle. By continuous scanning, the outer layer is gradually removed by the tip and  $F_{outer\ layer}$  decays with number of scan cycles to eventually approach zero.  $F_{inner\ layer}$  remains unchanged and defines the steady state of friction after the tip has removed the outer layer completely. In addition,  $F_{outer\ layer}^{N=1}$  is shown to increase linearly with the applied normal load (**Figure 3.2b**). The real contact area of the tip apex and the surface is known to increase with the load<sup>57,95</sup>. As a result, the tip presses deeper into the surface of the inner layer at a higher load, which also leads to an increase in the contact area between the tip and the outer layer due to the cone shape of the tip, and hence to a higher ploughing force. Hereafter,  $F_{inner\ layer}$  and  $F_{outer\ layer}^{N=1}$  are directly referred to as the friction force of the inner and outer layer.

The lifetime constant  $\nu$  of the friction force decay indicates the number of scans required to remove the outer layer. For original surface and the surface oxidized at different film-forming potentials, the values of  $\nu$  are independent of the applied normal loads, as shown in **Figure 3.6a-e**. The average value of  $\nu$  at different loads is plotted against the film-formation potential in **Figure 3.6f**. The lifetime constant  $\nu$

depends only weakly on the potential, decreases from 4.13 for original surface to 3.80 for the potential of 1.5 V. We conclude that the amount of material displaced in each cycle is determined not by a penetration depth of the tip but rather by the geometry of material moved in front of the tip. Although pile-up is observed at the edges of the slide track in **Figure 3.3a**, most images of the scanned areas do not exhibit clear indication for the disposition of removed material. It probably diffuses preferentially into the solution.

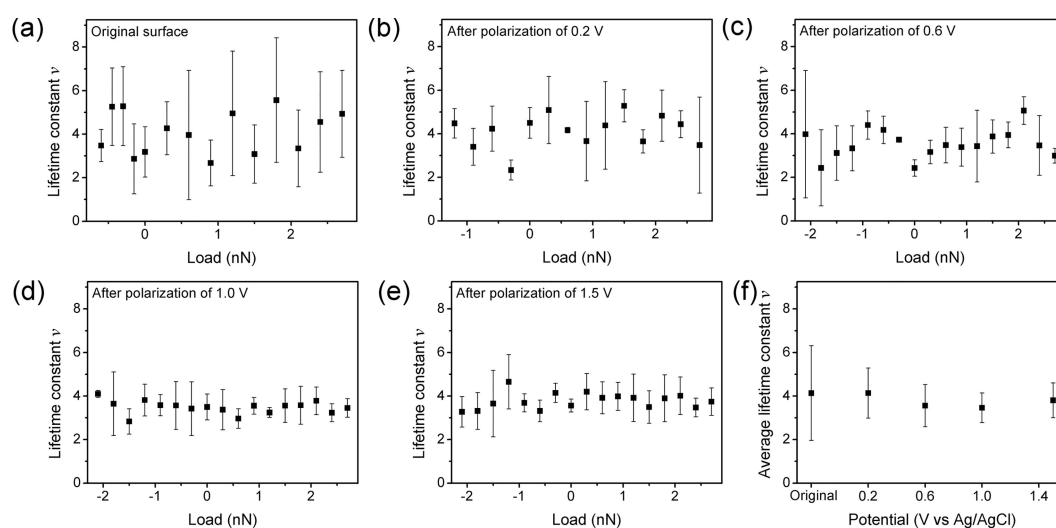


**Figure 3.6.** (a)-(e) Lifetime constant of the friction force decay as a function of applied normal loads on surfaces oxidized at different film-forming potentials; (f) Average value of lifetime constant  $\nu$  at different normal loads as a function of film-formation potentials. Data of the original surface are shown for comparison.

**Figure 3.5b** illustrates how the imaging load affects the characterization of slide track. At a high imaging load (i.e. 0.1 nN in **Figure 3.3b**), the tip scans directly on the inner layer, so that the height differences between track and surrounding area are not detected. However, the difference in friction between areas covered with outer layer

and areas free of outer layer are detected. At low imaging load (i.e. -2.4 nN in **Figure 3.3a**), the tip slides on the outer layer and is sensitive to changes in its topography. Because of the soft, porous nature of the outer layer, it is not guaranteed that the contact position of the tip is on the topmost surface even at a very low load. Therefore, the values in **Figure 3.4** are a lower estimate for the real thickness of the outer layer. Passive oxide films are very thin with thickness in the range of 1-3 nm<sup>46,48,48,53,84,92,96,97</sup>, and the inner layer is usually thicker than the outer layer<sup>49,96</sup>. The outer layer on stainless steel surfaces in sulfuric acid was found to be 0.5~0.6 nm thick from XPS analysis<sup>49</sup>. Skal et al.<sup>96</sup> estimated the thickness of the outer layers formed on a Ni-based alloy in polluted phosphoric acid at 0.26~0.44 nm. Our results in **Figure 3d** in good agreement to these reported values when considering the quantitative limitations of the method.

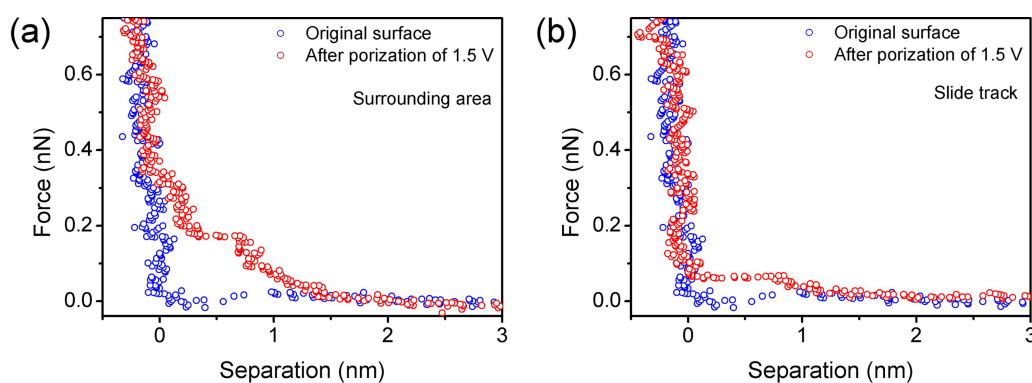


**Figure 3.7.** Typical force versus separation profile for the AFM tip approaching the sample surface: original surface and oxidized surface after polarization of 1.5 V: (a) surrounding area outside the slide track; (b) area inside the slide track. The tip-sample separation was calculated by subtracting the cantilever deflection from its approach distance.

Please note that the existence of a deformable outer layer can also be revealed by

force-distance curves using AFM. **Figure 3.7** compares force versus separation curves for the AFM tip approaching the surface of an original surface and an oxidized surface after polarization at 1.5 V. On the surrounding area covered with outer layer (**Figure 3.7a**), two steps of the repulsive force in front of the surface are observed, one at a separation of about 0.9 nm with a force of 0.18 nN and one at a separation of about 0.3 nm with a penetration force of about 0.32 nN. In **Figure 3.7b**, recorded within the slide tracks after repetitive scans, we observe only the step at a separation of 0.9 nm with a small repulsive force of  $\sim 0.06$  nN. We propose that the step at a separation of 0.3 nm, which is found on the surrounding area, is caused by the outer layer of the passivated surface. The height of the step is in good agreement with the height range reported for the outer layer in **Figure 3.4**. The force required to penetrate this layer is higher than the force required to remove it in friction experiments. The difference can be explained by the ease to remove the weakly bound precipitates forming the outer layer by a scanning tip, as compared to its compression by an approaching tip.

The steps at 0.9 nm separation probably represent the thickness of an electrochemical double layer of hydrated ions in front of the charged surface, where the hydrated ions originate from the buffer or from the dissolution process. For comparison we also show force-separation curves for the original surface. For the original surface, the step corresponding to the outer layer cannot be detected, while the step corresponding to a double layer of hydrated ions can be derived from a low density of data points between 0.9 nm and 0.4 nm, indicating jump in the tip-sample separation.



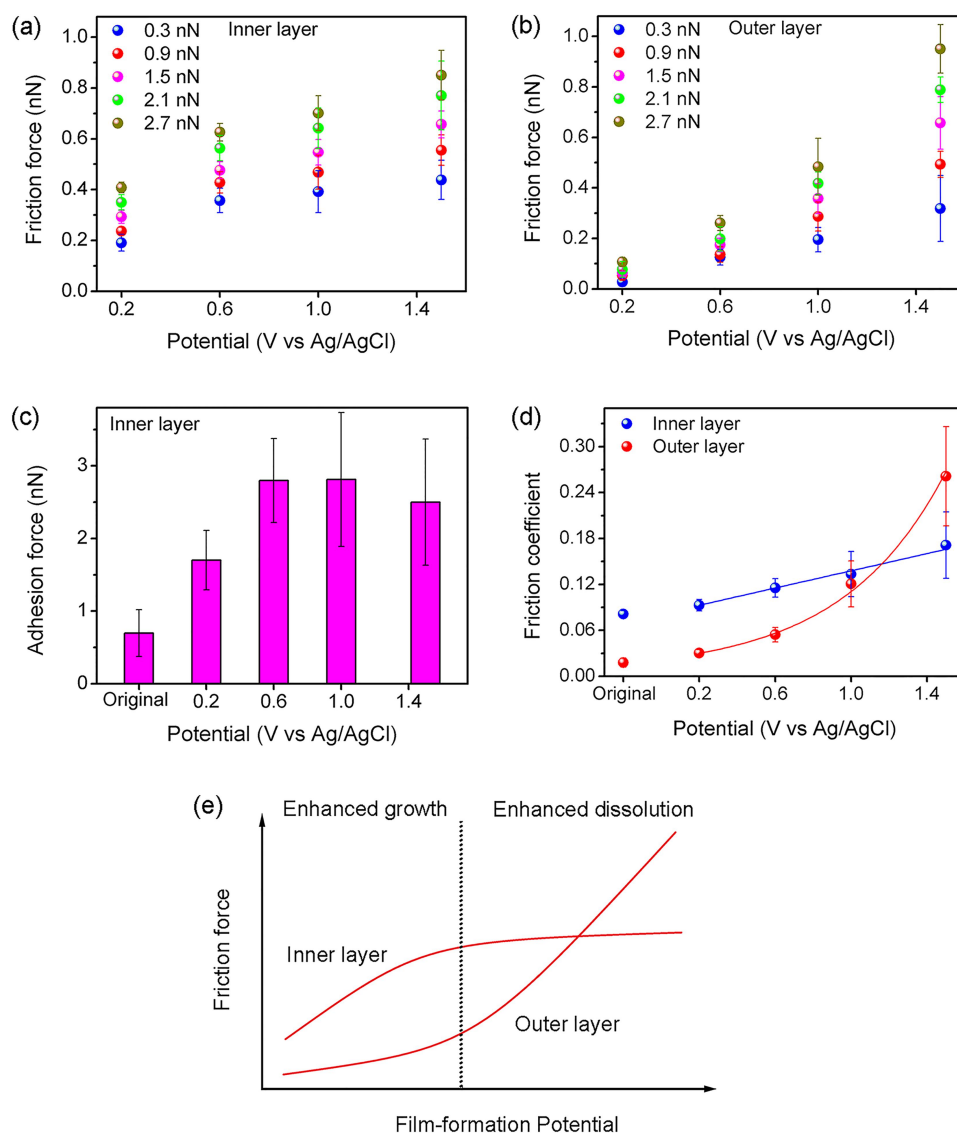


**Figure 3.8.** The dependence on film-formation potential of: (a) friction force of the inner layer; (b) friction force of the outer layer; (c) adhesion force of the inner layer; (d) friction coefficients, the smooth curves show fit of the data to a linear (inner layer) and exponential (outer layer) function. In (c) and (d), data of the original surface are shown for comparison. (e) Schematic explanation of the potential dependence of friction force.

In corrosion research, the inner and outer layer of passive films are distinguished by composition and structure, usually revealed by surface analytical techniques such as X-ray photoelectron spectroscopy (XPS) and scattering ion mass spectrometry

(SIMS)<sup>49,50,52,53</sup>. The inner and outer layers described in this work are revealed by their response to the ploughing tip: the part removed is the outer layer and the remaining part is the inner layer. We propose that these layers correspond closely to the inner and outer layer discussed in corrosion research. The difference in ploughing resistance between inner and outer layer can be rationalized in terms of their different structure, oxidation status, and formation mechanism. We will now discuss how the nonlinear change of film dissolution with potential is also reflected in friction and ploughing differences between the two layers.

**Figure 3.8a** and **b** shows the dependence of friction force on film-formation potential for the inner and outer layer at different loads. For the inner layer, the friction force increases sub-linearly as the film-forming potential increases. For the outer layer, the friction force increases super-linearly with film-forming potential. We remind the reader that all friction data are recorded at open-circuit potential after surface oxidation at the film-forming potential.

We have already mentioned that tip-surface adhesion causes finite friction even at zero externally applied load. We can estimate the adhesion force as function of film-forming potential by extrapolating the respective friction vs. load curves to zero friction (see the adhesion force indicated as intercept in **Figure 3.2b**). The friction force of the inner layer (the stable value in **Figure 3.2c**) is measured for the tip sliding on the inner layer after removal of the outer layer and, therefore, the adhesion force of the inner layer can be estimated without distortions from the outer layer. The adhesion

force of the inner layer increases with increasing potential up to 0.6 V and remains constant within errors above that value (**Figure 3.8c**). The total normal force acting on the tip-surface contact is the sum of the force externally applied to the AFM tip and the adhesion force. For the oxidized surfaces, the adhesion force is in the range of 1.7~2.8 nN and thus comparable to the applied loads (the maximum load is 2.7 nN). The effect of adhesion is significant and cannot be neglected in the analysis of friction forces.

The change in adhesion of the inner layer (**Figure 3.8c**) can be understood as effect of the surface charge. Sato<sup>98,99</sup> suggested that anodic polarization imparts a net positive surface charge in the presence of sulfate/phosphate, due to the concentration of the dissolved metal cations at the anode interface. A positive surface charge has been previously observed on the passivated surface of nickel in sulfuric acid<sup>100</sup> and iron in a borate-phosphate buffer solution (pH < 8.5)<sup>101</sup>. Therefore, a positively charged surface of the inner layer can be expected in our measurements. The oxidized surface of the silicon AFM tip is negatively charged<sup>102,103</sup>. The opposite charges generated at the tip and oxidized surface compared to the original surface strengthen the adhesion. At a higher film-formation potential, the higher concentration of dissolved metal ions on the surface of the inner layer generates more surface charge and leads to the increased adhesion on films formed at a potential increasing from 0.2 to 0.6 V. Above a potential of 0.6 V, the adhesion force is constant within error. This observation is explained by the enhanced growth of the outer layer at high potentials. The dissolved metal ions migrate as hydrates towards the solution and partially

transform as precipitates into the outer layer<sup>46,47,51,91,93</sup>. This process probably inhibits the further concentration of metal ions on the surface of the inner layer, resulting in a stable surface charge and constant adhesion.

We compare friction of the inner and outer layer by means of a friction coefficient which is calculated as the slope of a linear fit to the friction force versus normal force data. **Figure 3.8d** presents the variation in friction coefficient with the film-formation potential. Data for the original surface (no electrochemical polarization) are shown for comparison. We observe a linear increase of the friction coefficient of the inner layer with increasing film-forming potential. For the outer layer, the friction coefficient increases exponentially with potential up to 1.5 V.

In the passivation region, low valence insoluble oxide species are increasingly enriched in the inner layer upon further oxidation at a higher film-formation potential<sup>49,50,104</sup>, with a increased thickness and lower defect density of the inner layer<sup>46,90,91,92,94,104</sup>. This growth of the inner layer improves the protective effect, however, accompanied by an increased surface roughness of the layer at higher potentials<sup>46,93</sup>. On crystalline gold electrodes, higher roughness after electrochemical oxidation led to a higher friction coefficient in AFM experiments<sup>72,73</sup>. Such oxidation-induced roughness may also contribute to the increase in friction coefficient of the inner layer (**Figure 3.8d**), although we cannot quantify an increase of molecular-scale roughness on the amorphous metallic glass surfaces. Other mechanisms which may contribute to the increase in friction coefficient include the

attractive interaction of surface charge distribution on the oxidized surfaces<sup>105</sup>, the excitation of rotation in adsorbed dipoles on the surface<sup>106,107</sup>, or the chemical interaction contrast on different oxidation states<sup>74</sup>.

Passivity breakdown occurs at a potential of 1.5 V, where the passive oxide film becomes unstable and loses its barrier effect<sup>50,90,92,93,108</sup>. From a nanomechanical point of view, there is still a compact layer on the surface in the transpassive state, which remains stable during continuous scanning. The inner layer of the transpassive surface exhibits similar friction performance as that of a surface oxidized at 1.0 V, although its structure and composition are expected to be different from the passive state. Oxygen and corrosive ions penetrate the inner layer of the transpassive surface and access the surface of the MG substrate.

We will finish this section by a discussion of the potential dependence of friction forces. A schematic summary is shown in **Figure 3.8e**. Passivity is a kinetic phenomenon in which oxide formation and dissolution occur simultaneously. The growth of the surface film depends on the relationship between formation and dissolution of surface oxides<sup>50,90,92</sup>. The outer layer originates from the dissolution of the inner layer oxides and the substrate. Consequently, it can be found on all surfaces including the original surface. The decay of friction force under continuous scanning on all surfaces confirms the existence of the outer layers. Stronger dissolution produces more precipitates towards the outer layer, leading to more material to be removed per pass of the tip and thus a higher ploughing force. As a result, friction in

the outer layer depends on the dissolution process. When the potential is lower than 0.6 V, the dissolution is weak compared to the growth of the film and the outer layer contributes significantly less to the friction coefficient than the inner layer (**Figure 3.8d**).

Above a film-forming potential of 0.6 V, the friction coefficient of the outer layer increases faster with potential and gradually approaches that of the inner layer (**Figure 3.8d**), indicating that the dissolution becomes stronger. As mentioned above, the tip does not fully penetrate the outer layer in the low-load regime during the 1st scan cycle on surfaces oxidized at 1.0 and 1.5 V, while the tip penetrates the entire outer layer at all loads for lower potentials. This difference indicates a denser outer layer formed at 1.0 and 1.5 V and thus enhanced dissolution. The onset of transpassive dissolution can occur at elevated passive potentials just below the transpassive potential<sup>48,50,94,97</sup>. We believe that the enhanced dissolution above 0.6 V reflects the onset of transpassive dissolution. Transpassive dissolution is characterized by rapid dissolution of metal elements at high potentials<sup>93,50</sup>. These elements contribute to the enhanced growth of the outer layer and cause the significant increase in friction while the film remains passive. At the transpassive potential of 1.5 V, passivity breakdown occurs when the oxide dissolution becomes faster than its formation. In this regime, the outer layer contributes more to the friction coefficient than the inner layer. The potential dependence of friction of the outer layer reported in this work provides an excellent probe of the nonlinear change in the dissolution process with increasing potential, consistent with the results of corrosion research.

Passive films are often investigated by X-ray photoelectron spectroscopy (XPS) and scattering ion mass spectrometry (SIMS)<sup>49,50,52,53</sup>. While these methods provide valuable insights into oxidation states and elemental distribution, their interpretation is hampered by changes of the surface chemistry and structure upon rinsing off the electrolyte, transfer to the surface analytical equipment, and exposure to vacuum conditions. AFM has emerged as a method to study passive films on metals at nanometer scale immersed in corrosive environments. Recent applications of AFM have focused on the topographic structure of passive films<sup>109,110</sup>. Our results demonstrate how the combination of topographic imaging and friction measurements resolves structure and properties of passive films *in situ* and advances the understanding of corrosion mechanisms.

### 3.3 Conclusion

Nanoscale friction experiments on a  $Zr_{63}Ni_{22}Ti_{15}$  metallic glass after potentiostatic polarization are introduced as an in-situ tool to study the structure of electrochemically formed surface oxide films. The surface oxide film has a bilayer structure with a mechanically stable inner layer underlying an instable outer layer. The latter is gradually removed during repeated scanning with the tip of an atomic force microscope. The removal causes an exponential decay of the friction force with number of scan cycles towards a steady state, in which the tip slides on the bare inner layer. The inner layer can be identified with the compact protective layer discussed in corrosion science, and the outer layer with the porous dissolution layer. These in-situ

results thus confirm concepts for the oxide film structure which were derived from ex-situ surface analytics.

The dependence of friction forces on the film-formation potential reflects the growth mechanism of the surface film. At low polarization potentials, oxide growth and weak dissolution of the passive film lead to higher friction force on the rougher inner layer and significantly lower friction of the outer layer. At higher polarization potentials, the transpassive dissolution causes a rapid growth of the outer layer and a corresponding increase of its friction contribution. The findings thus reveal mechanisms of nanoscale friction on a metallic glass in an aqueous environment and contribute to the understanding of nanotribological properties of metallic glasses required for miniature applications in corrosive conditions. Moreover, the variation in friction of the inner and outer layer as function of the film-formation potential reflects the dynamic nature of passivity, i.e. the competitive processes of oxide film formation and dissolution, and confirms the relevance of nanotribological in-situ experiments for the study of microscopic corrosion mechanisms.



## **Chapter 4: Effect of Corrosive Electrolytes**

This chapter presents friction studies of MGs in different corrosive solutions, focusing on the effect of different corrosive electrolytes. The chapter begins with the investigation of nanoscale friction with different immersion times and the discussion of the corresponding friction mechanisms. We continue with a study of atomic-scale stick-slip motion on corroded surfaces. Finally, the tribochemical processes at high loads in corrosive environments are discussed.

### **4.1 The Time Evolution of Nanoscale Friction**

The previous chapter investigated nanoscale friction after electrochemical polarization. Our results demonstrated a new method to investigate *in situ* the structure of surface oxide films on MGs in aqueous solutions. This chapter presents friction studies of MGs after different immersion times in two different corrosive solutions, i.e. without electrochemical polarization, using the same experimental method. On the one hand, the influence of corrosion on nanoscale friction on MGs is evaluated. On the other hand, nanotribological in-situ experiments are implemented to reveal microscopic corrosion processes.

This chapter has been submitted for publication with a few modifications:

Ma, H. R.; Bennewitz, R., Relationship between corrosion and nanoscale friction on a metallic glass. *Friction* (submitted)

### 4.1.1 Experimental Details

All friction experiments were conducted at room temperature in 0.2 M phosphate buffer ( $\text{Na}_2\text{HPO}_4 + \text{NaH}_2\text{PO}_4$ , pH~7) and 0.2 M NaCl solution. Friction experiments were carried out after immersing a new sample into the solution for 1, 24 and 72 h, respectively. The exposed area of the samples was  $\sim 2.0 \text{ cm}^2$  and  $\sim 1.0 \text{ mL}$  of corrosive solution was added. For these experiments, we used the oxidized tip of a single crystalline Si cantilever (PPP-CONT, see **Chapter 2.6**). The AFM tip sliding velocity was  $8.0 \mu\text{m s}^{-1}$  and the scan field was  $1.0 \times 0.125 \mu\text{m}^2$ . Sixteen cycles of repetitive scans, each 64 scan lines, were performed in each scan field at a constant applied load and repeated on different surface areas with different loads, while the friction force was recorded.

In order to establish differences in corrosion of ZrNiTi MGs between the solutions using a standard procedure, potentiodynamic polarization experiments were performed in the range of -0.5 to 1.5 V at a potential sweep rate of  $1.0 \text{ mV s}^{-1}$ , in a home-made cell with three-electrode setup. The MG ribbon, a miniature Ag/AgCl electrode, and a Au wire served as working, reference and counter electrode, respectively. The polarization test was a separate experiment and subsequent friction experiments were performed using new samples which were immersed without applying a potential.

## 4.1.2 Results and Discussion

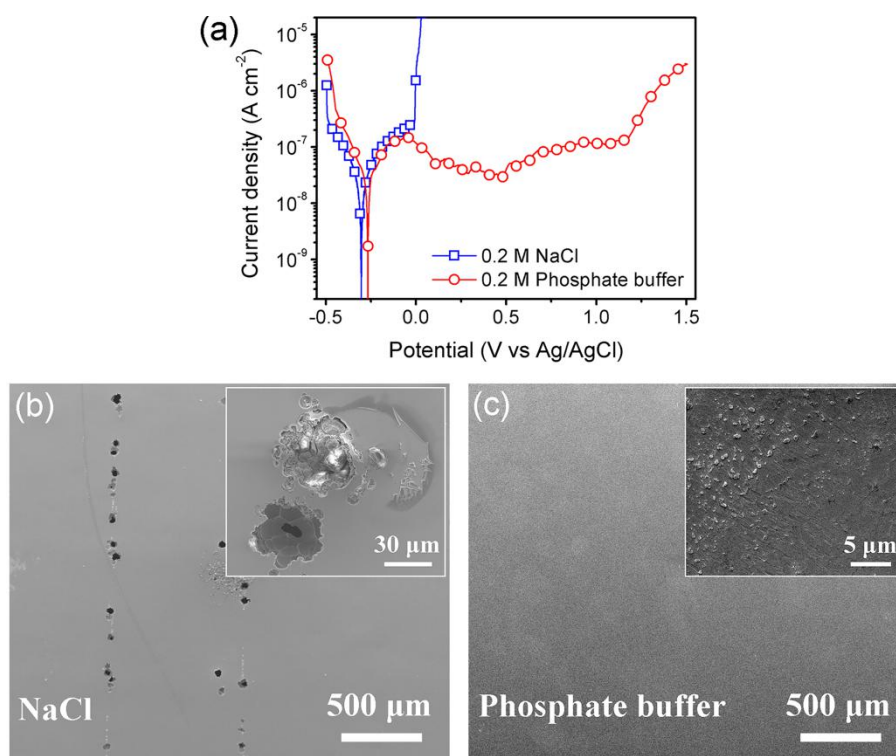


**Figure 4.1.1** (a) Potentiodynamic polarization curves of ZrNiTi MG in 0.2 M NaCl solution and 0.2 M phosphate buffer recorded in the electrochemical AFM cell. SEM images of corroded surface after potentiodynamic polarization test in (b) NaCl solution and (c) phosphate buffer.

The phosphate buffer and NaCl solution were selected as test solutions because of their differences in corrosion of ZrNiTi MGs. **Figure 4.1.1a** shows potentiodynamic polarization curves of ZrNiTi MGs in NaCl solution and phosphate buffer recorded in the electrochemical AFM cell. In NaCl solution, no passivity is observed during anodic polarization. The current density increases rapidly even at a low applied potential ( $\sim 0$  V). In contrast, the ZrNiTi MG in phosphate buffer is passivated spontaneously with a wide passivation region (-0.05 to 1.2 V). These results indicate a significantly higher corrosion resistance of the MG in phosphate

buffer compared to NaCl solution.

After potentiodynamic polarization, the corroded surfaces of ZrNiTi MGs were investigated by scanning electron microscopy (SEM), images are shown in **Figure 4.1.1b** and **c**. Corrosion pits with a lateral extension of tens of micrometers were observed on the surface polarized in NaCl solution, indicating that the chloride-containing solution initiates localized pitting. The inset in **Figure 4.1.1b** shows the magnified image of typical corrosion pits. No such pits are found after polarization in phosphate buffer (**Figure 4.1.1c**). The surface is mostly smooth and only some parts exhibit signs of increased roughness (the inset in **Figure 4.1.1c**). We conclude that the polarization-induced surface modifications proceed uniformly in phosphate buffer.

Pitting has been reported for many MG surfaces after polarization in chloride solutions<sup>44,111,112,113</sup>. Pitting corrosion is induced by heterogeneity or discontinuity of the amorphous matrix, for example by crystalline inclusions<sup>112</sup>. On the surfaces shown in **Figure 4.1.1b**, pitting is always distributed along a line. Wang et al. found<sup>114</sup> that pitting occurs preferentially at the shear offsets on a pre-deformed Zr-based MGs due to the higher chemical activity of offset sites compared with the surrounding flat region. This influence of surface morphology was also shown for copper surfaces, where it was suggested that more electrons escape in the vicinity of a peak than in a valley<sup>115</sup>. A surface undulation with parallel valleys on our ZrNiTi MG ribbons may be the reason for distribution of pits along lines. Another possible reason is residual

stress, indicated by the strip curled state of MG ribbons after preparation. In contrast, the ZrNiTi MG is not susceptible to pitting corrosion in phosphate buffer. Phosphates are generally used as effective inhibitors to minimize the risk of rebar corrosion<sup>116,117</sup>. The phosphate ions hinder the initiation of pitting by their buffering capacity, which impedes acidification inside the pits and promotes the repassivation of initially metastable pits<sup>116</sup>. The stability and protection effect of the surface film is also improved when phosphates are involved in the film formation<sup>117</sup>.

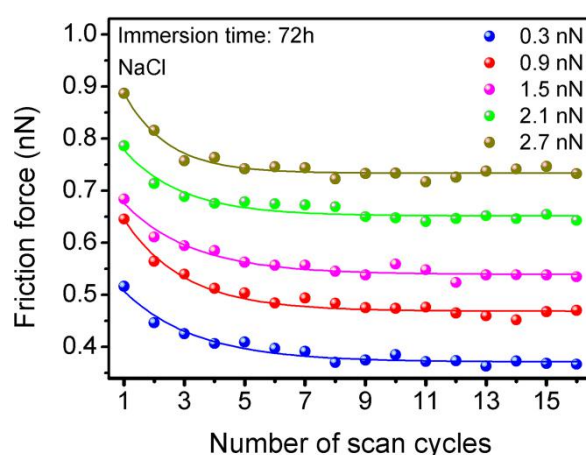


**Figure 4.1.2.** Friction force as a function of number of scan cycles on ZrNiTi after immersion into 0.2 M NaCl solution for 72h. The smooth curves are fits of Eq. (3.2) and (3.3) to the data.

The development of friction force with the number of scan cycles after immersion in NaCl solution for 72h is shown in **Figure 4.1.2** for experiments at different applied loads. Please note that all friction experiments are performed in the immersion solution without applying a potential. Similar to the previous results in **Chapter 3**, the friction force initially decreases with number of scan cycles and then reaches a steady value at all loads. This decay of friction is also found for all other parameters, i.e. after immersion in NaCl solution for 1h and 24h, and in phosphate

buffer for all immersion times. Different from the polarization result (**Figure 4.1.1b**), there are no pits on the sample surface even after immersion for 72h in NaCl solution. This weak corrosion during immersion without applied potential will be discussed in more detail below.

**Figure 4.1.3a** shows the topography of the slide track and corresponding friction force images after 16 scan cycles in the central  $1.0 \times 0.125 \mu\text{m}^2$  region at an applied normal load of 1.5 nN. There is no measurable height difference between the central slide track and the surrounding area in the topography image. However, we do observe a contrast between these two areas in the friction force image, revealing the position of the slide track. The corresponding line-scan profiles across the slide track and surrounding area are presented in **Figure 4.1.3b**. The friction force is significantly smaller on the slide track, while the height of slide track and surrounding area do not differ.

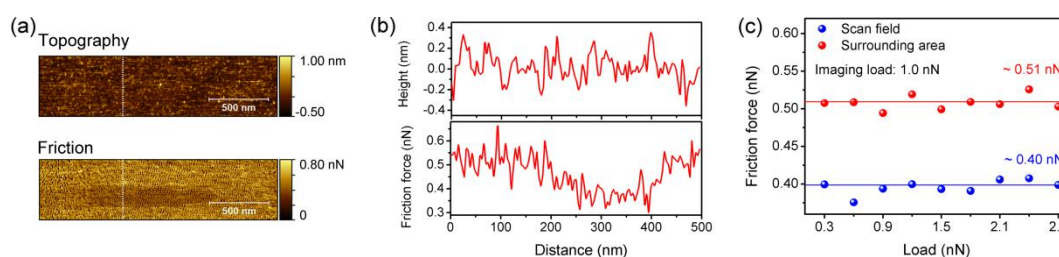


**Figure 4.1.3.** (a) AFM topography and friction force images recorded on ZrNiTi MG after immersion into 0.2 M NaCl solution for 72h and after scanning the central area ( $1.0 \times 0.125 \mu\text{m}^2$ ) 16 times at a normal load of 1.5 nN (imaging load: 1.0 nN); (b) Cross section of the topography and friction image corresponding to the lines drawn in (a); (c) Friction force of the slide track and surrounding area as a function of the normal load applied during 16 repetitive scans in the slide track. Friction data were extracted from images recorded at an imaging load of 1.0 nN.

In **Figure 4.1.3c**, the friction force on the slide track after 16 repetitive scans and on the surrounding area are plotted as a function of the normal load applied to the slide track during the repetitive scans. The friction values were calculated from images like the one shown in **Figure 4.1.3a**. Please note that each slide track was produced with the respective load on a different surface area. The friction force of the surrounding area is constant about 0.51 nN. This is expected because the imaging load is constant and the area surrounding the slide tracks is not altered by preceding scans. The friction forces of the slide tracks produced at different normal loads are also similar, but with about 0.40 nN lower than that on the surrounding area. This observation lets us conclude that the tip slides on a surface which has the same characteristics after repetitive scanning at different loads.

Surface oxide films formed during corrosion have been reported to exhibit a bilayer structure with a dense, protective inner layer and a porous, precipitated outer layer<sup>22,45,47,49,53</sup>. The outer layer originates from the dissolution of the underlying dense layer and the MG substrate. The characteristics of the friction results reported in **Figure 4.1.2** and **4.1.3** reflect the bilayer structure of surface oxide films. A similar correspondence between friction and topography on the one hand and bilayer structure was observed for MG surfaces after polarization in phosphate buffer (see **Chapter 3**).

We will now discuss our experimental results in view of the bilayer structure of the surface oxide film formed during immersion. The lack of height contrast in **Figure**

4.1.3a is explained by penetration of the AFM tip into the soft outer layer surrounding the slide track. No height difference can be measured between the surrounding area, where the tip penetrates the outer layer, and the slide track, where the outer layer was removed. Friction, however, is higher in the surrounding area, where the tip is still plowing the outer layer.

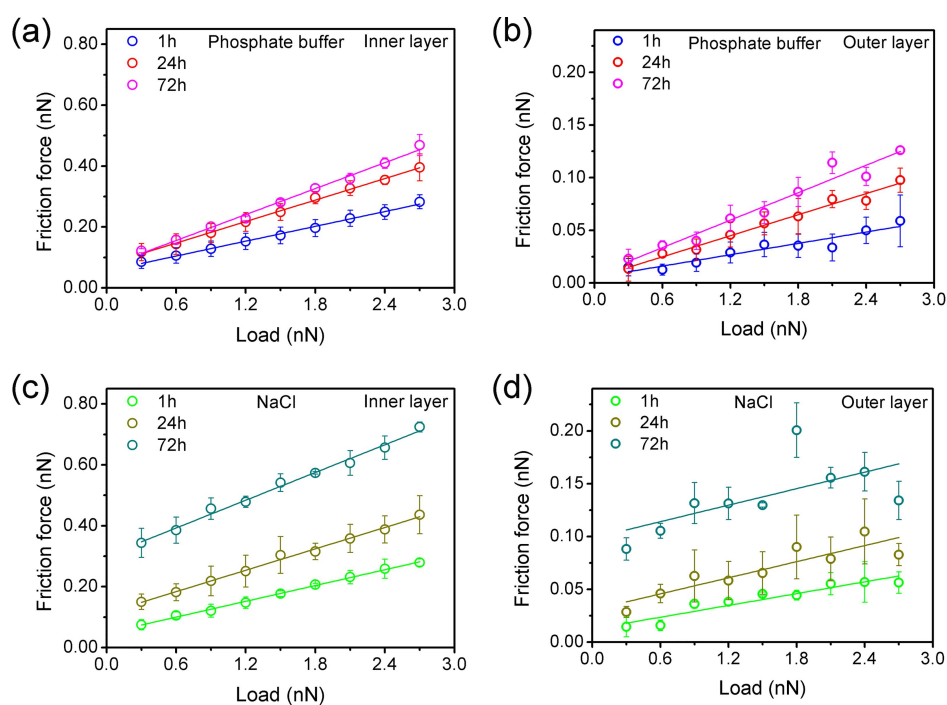


**Figure 4.1.4.** The dependence on the applied normal load during the repetitive scans of: (a) friction force of the inner layer and (b) friction force of the outer layer in phosphate buffer; (c) friction force of the inner layer and (d) friction force of the outer layer in NaCl solution. Solid lines are linear fits. Each data point is the average value of three replica experiments and error bars represent the standard deviation.

The decay of friction with number of scan cycles (**Figure 4.1.2**) is modeled with Eq. (3.2) and (3.3) from **Chapter 3**. The friction forces are compared for inner and outer layer in **Figure 4.1.4** for the different normal loads applied during respective scanning. For both solutions and all immersion times, the friction force of the inner



layer increases linearly with the normal load (**Figure 4.1.4a** and **c**). Adhesion contributes significantly to the friction force, i.e. a friction force is measured even at zero externally applied load. A linear increase of the friction force with the applied load is also observed for the outer layer after immersion in phosphate buffer (**Figure 4.1.4b**). We attribute the increase in friction for the outer layer to the lateral contact area between outer layer and tip, which grows in parallel to the increased contact area of inner layer and tip apex at a higher normal load. The regularity of linear dependence of friction in the outer layer indicates a laterally uniform outer layer and thus a uniform dissolution process on the surface in phosphate buffer, even after immersion for 72h. This is not the case for the NaCl solution (**Figure 4.1.4d**), where a significant scattering of friction values is observed, especially after a longer immersion. The general trend is still towards higher friction forces of the outer layer for increasing load. The outer layer formed during immersion in NaCl solution is non-uniform, indicating an inhomogeneous dissolution process on the surface. This difference in corrosion processes between phosphate buffer and NaCl solution agrees well with the results of potentiodynamic polarization (**Figure 4.1.1**), although the inhomogeneity of dissolution is still not sufficient to induce pits on the sample surface after immersion in NaCl solution.

We will now compare friction results in phosphate buffer and NaCl solution. **Figure 4.1.5a-c** displays the dependence of the friction coefficient and the adhesion force on immersion time for inner and outer layers. The friction coefficient is calculated as the slope of a linear fit to the friction force versus normal load data

(**Figure 4.1.4**). The adhesion force of the inner layer versus the AFM tip is determined as the abscissa intercept of the linear fit at the zero friction force (**Figure 4.1.4a and c**). Data of the corroded surface in phosphate buffer after polarization for 80 minutes at 1.0 V vs Ag/AgCl (see **Chapter 3**) are shown for comparison. When a potential is applied in NaCl solution, the solution turns cloudy after a few minutes with a large amount of corrosion products released into the solution suggesting a serious corrosion. This degradation impedes AFM friction experiments which are based on optical detection through the solution.

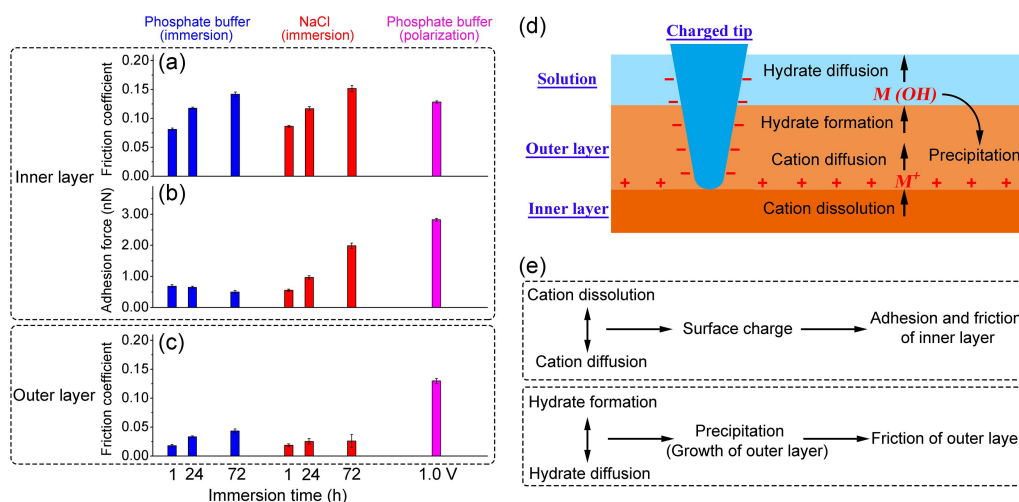


**Figure 4.1.5.** The dependence on immersion time of: (a) friction coefficient of the inner layer; (b) adhesion force of the inner layer; (c) friction coefficient of the outer layer. Data are obtained from linear fits in Figure 4 and error bars represent the errors in the fits. Data for corroded surfaces after polarization in phosphate buffer for 80 minutes at 1.0 V vs Ag/AgCl are shown for comparison. (d) Schematic illustration of physicochemical processes at the interfaces of the surface oxide film related to the surface dissolution during corrosion.  $M^+$  represents dissolved metal cations,  $M(OH)$  denotes hydrates formed by reactions of metal cations with the solution. (e) Summary of the influence of corrosion on friction and adhesion of the inner layer and friction of the outer layer.

After immersion for the same time in phosphate buffer and NaCl solution, the

friction coefficients of the inner layer are equal within error. After immersion for 72h, they become comparable with the friction coefficient after polarization in phosphate buffer (**Figure 4.1.5a**). Passivation is a kinetic process in which the growth and dissolution of oxide films occur simultaneously. Consequently, the inner layers in these three cases can be expected to be different in structure and composition, in view of the different dissolution processes which will be discussed in detail below. It is therefore important to note that the frictional response of the inner layer develops similarly during immersion in NaCl and phosphate buffer and that the friction coefficient of the inner layer is similar after long immersion and after polarization in phosphate buffer.

The adhesion force remains constant with increasing immersion time in phosphate buffer and is much smaller than after polarization (**Figure 4.1.5b**). The anodic polarization results a net positive surface charge<sup>100,101</sup>, caused by the accumulation of the dissolved metal cations on the inner layer and strengthens the adhesion of the negatively charged silicon AFM tip<sup>102,103</sup>. **Figure 4.1.5d** depicts schematically this charge buildup at the surface of the inner layer, which involves two physicochemical processes. Metal cations are generated at the interface between inner and outer layer by dissolution of the inner layer oxides and of the metal substrate, and then diffuse away from the interface. In the case of immersion, the constant small adhesion reveals a stable surface charge with different immersion times. We conclude that there is an equilibrium between production of metal cations by dissolution and diffusion of the ions into the solution which entails the constant surface charge. In

other words, during immersion in phosphate buffer, the ion transfer is limited by dissolution rate. Anodic polarization in phosphate buffer with its stronger metal ion dissolution leads to an accumulation of cations on the surface and thus to a higher surface charge.

In NaCl solution, adhesion increases with immersion time, indicating an increased surface charge. We conclude that dissolution of metal ions occurs faster than their diffusion into solution in NaCl solution, i.e. the ion transfer is limited by diffusion. The lack of passivation is in agreement with reports about a decrease in corrosion resistance in NaCl solution with immersion time due to the development of defects in the surface film<sup>118,119</sup>.

The increase in the friction coefficient of the outer layer indicates the growth of the outer layer with increasing immersion time. More material is in lateral contact with the sliding tip which experiences thus a higher ploughing resistance. The outer layer grows by precipitation of metal hydrates which are formed when dissolved metal ions diffuse towards the solution. This growth of outer layer involves the three physicochemical processes depicted in **Figure 4.1.5d**, which have been invoked to explain the bilayer structure found after polarization<sup>45,47,120</sup>. Metal cations react with water, or anions present in the solution, and form hydrated oxides and hydroxides at the interface between outer layer and solution. These hydrates diffuse into the bulk solution, or partially transform as precipitates into the outer layer. The latter process may be enhanced as a result of hydrate accumulation into supersaturation close to the

surface. As the immersion continues, the friction coefficient of the outer layer increases sub-linearly with immersion time in phosphate buffer (**Figure 4.1.5c**). The corrosion resistance of the oxide film in passivating solutions was reported to increase with time during the first stage and then remain almost constant after longer immersion time<sup>121,122,123</sup>. We suggest a similar development for MGs in phosphate buffer, where the protective effect of the inner layer becomes stronger with the immersion time, the dissolution becomes slower, and the growth rate of the outer layer decreases.

In NaCl solution, the friction coefficient of the outer layer is constant at a value smaller than that of the outer layer in phosphate buffer after long immersion. During immersion, the outer layer does not grow significantly in NaCl solution, although the adhesion data indicated stronger dissolution than in phosphate buffer. Compared to chloride ions, phosphate ions adsorb more efficiently to the surface. Their buffering effects create a higher pH value near the surface, which favors the formation and precipitation of metal hydrates<sup>116,117</sup>. Such an accumulation of hydrates does not proceed in NaCl solution and we conclude that the formation of metal hydrates is in equilibrium with their diffusion into the solution, or that the existing outer layer prevents the precipitation of further hydrates.

The friction coefficient for the outer layer after anodic polarization in phosphate buffer is much higher than that after immersion. During electrochemical polarization, a great quantity of dissolved ions diffuses as hydrates towards the solution in a short

time, which become supersaturated near the metal surface and precipitate into the outer layer. This supersaturation leads to the enhanced growth of the outer layer during polarization. Combined with the adhesion data, the whole processes in **Figure 4.1.5d** is diffusion control after polarization.

In summary, the key processes affecting the frictional response of MGs during corrosion are metal cation dissolution and diffusion as well as hydrate formation and diffusion. It has been established that these processes constitute the surface dissolution process during corrosion<sup>45,120</sup>. **Figure 4.1.5e** illustrates how these physicochemical processes affect the friction force of the inner and outer layer. After immersion for 72h in phosphate buffer and NaCl solution and after polarization, the friction coefficients of the inner layer are similar (**Figure 4.1.5a**). The difference in friction force of the inner layer mainly depends on the variation of adhesion, which is determined by the competitive processes of metal cations dissolution and diffusion on the inner layer. The competitive processes of hydrates formation and diffusion at the outer layer/solution interface determine the growth and thereby the friction coefficient of the outer layer.

### **4.1.3 Conclusion**

Our results reveal the instructive connection between nanoscale friction and surface processes on a metallic glass upon immersion in corrosive solutions. Friction coefficients indicate the development of the passivated inner layer of the surface and the growth of a precipitated and displaceable outer layer. Adhesion indicates the

accumulation of charge at their interface. The evolution of friction with increasing immersion time reveals the interrelation of relevant physicochemical processes: the production of metal cations by surface dissolution at the interfaces of two layers, the diffusion of ions to the interface of outer layer and solution, the formation of hydrates at the surface, and the competition between diffusion of hydrates into solution and their precipitation into a growing outer layer. Understanding the mechanisms of nanoscale friction on metallic glasses is a basis for applications involving mechanical contacts in corrosive conditions. On the other hand, nanotribology offers unique methods to resolve microscopic corrosion process in situ.

Although results were reported here for metallic glasses, we suggest that the study of surfaces layers and charges by nanotribology can be extended to the understanding of corrosion mechanisms in other metal and alloy systems. Future studies can exploit the lateral resolution of scanning force microscopy to detect dissolution and precipitation on selected areas of interest such as different phases, grains and inclusions<sup>70</sup>.

## 4.2 Atomic-scale Stick-slip Motion

Two previous chapters presented friction results which demonstrated the role of the surface oxide layer during corrosion. Atomic-scale stick-slip can contribute to a deeper understanding of the fundamental mechanisms of friction for a single-asperity contact (see **Chapter 1.3.1**). This chapter transitions to this new topic. We examined the stick-slip events on the oxidized surfaces to study the influence of corrosion on atomic-scale friction processes and the corresponding mechanisms.

### 4.2.1 Experimental Details

We conducted friction experiments on MG ribbons immersed in 0.2 M borate buffer ( $\text{H}_3\text{BO}_3 + \text{Na}_2\text{B}_4\text{O}_7$ , pH~7) and 0.2 M phosphate buffer ( $\text{Na}_2\text{HPO}_4 + \text{NaH}_2\text{PO}_4$ , pH~7) at room temperature. Each friction experiment was started after immersing a new MG ribbon into the solution for 1 h equilibration. A single crystalline Si cantilevers (PPP-CONT, see **Chapter 2.6**). The tip scanning velocity was  $24 \text{ nm s}^{-1}$ .

To know differences in corrosion of ZrNiTi MGs between the solutions, potentiodynamic polarization experiments were performed in a home-made liquid cell with three-electrode setup (see **Chapter 2.5**). The working, reference and counter electrode were the MG ribbon, a miniature Ag/AgCl electrode, and a Au wire, respectively. The polarization test was a separate experiment and subsequent friction measurements were carried out on new ribbons without applying a potential.



## 4.2.2 Results and Discussion

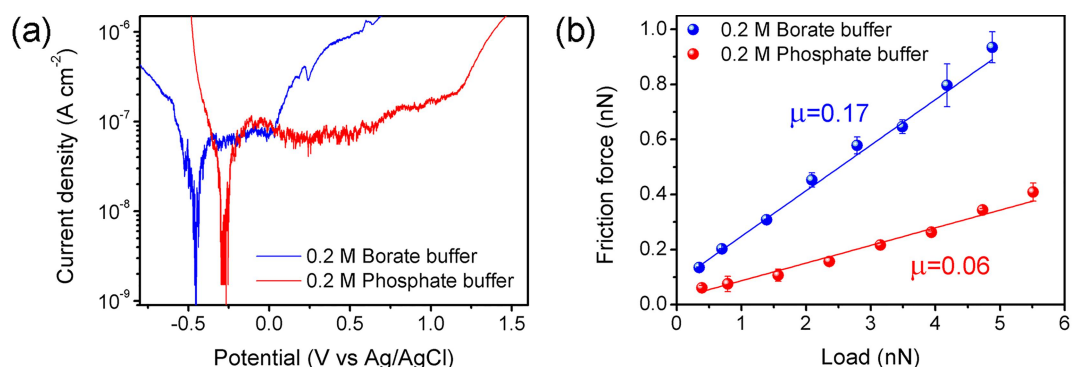


**Figure 4.2.1** ZrNiTi MGs in 0.2 M borate buffer and 0.2 M phosphate buffer: (a) potentiodynamic polarization curves recorded in the ECAFM cell; (b) variation of friction force with normal load recorded on the corroded surfaces after immersion for 1h without applying a potential. Solid lines are linear fits.

Potentiodynamic polarization curves of ZrNiTi MGs in borate buffer and phosphate buffer are shown in **Figure 4.2.1a** recorded in the electrochemical AFM liquid cell. The sample is passivated in phosphate buffer with a wider passivation region (-0.05 to 1.2 V) than that in borate buffer (-0.3 to 0.0 V), which indicates a higher corrosion resistance of MGs in phosphate buffer. This difference in corrosion properties would exert an important influence on nanoscale friction on MGs. Corroded surfaces in NaCl solution usually become rougher with some small particles attached to the surface, which hamper a clear observation of stick-slip phases. Thus, here we use the borate buffer instead of NaCl solution.

**Figure 4.2.1b** presents the friction force as a function of the applied normal load on the corroded surfaces without applying a potential. The friction coefficients are determined as the slopes of linear fits to the data. The friction coefficient is  $\mu = 0.17$  in

borate buffer and  $\mu = 0.06$  in phosphate buffer. Friction increases more significantly in borate buffer. This difference in friction will be discussed in more detail below. As similar with **Chapter 4.1**, the bilayer structure of surface oxide films in this case is expected and friction forces in **Figure 4.2.1b** are the sum contribution of the inner and outer layer while the tip slides on the inner part. In this work, we focus on the evolution of stick-slip friction with load, friction force is thus recorded on a same area at all applied loads. However, the influence of the outer layer is small because of the low friction contribution compared to the inner part (see **Chapter 4.1**).

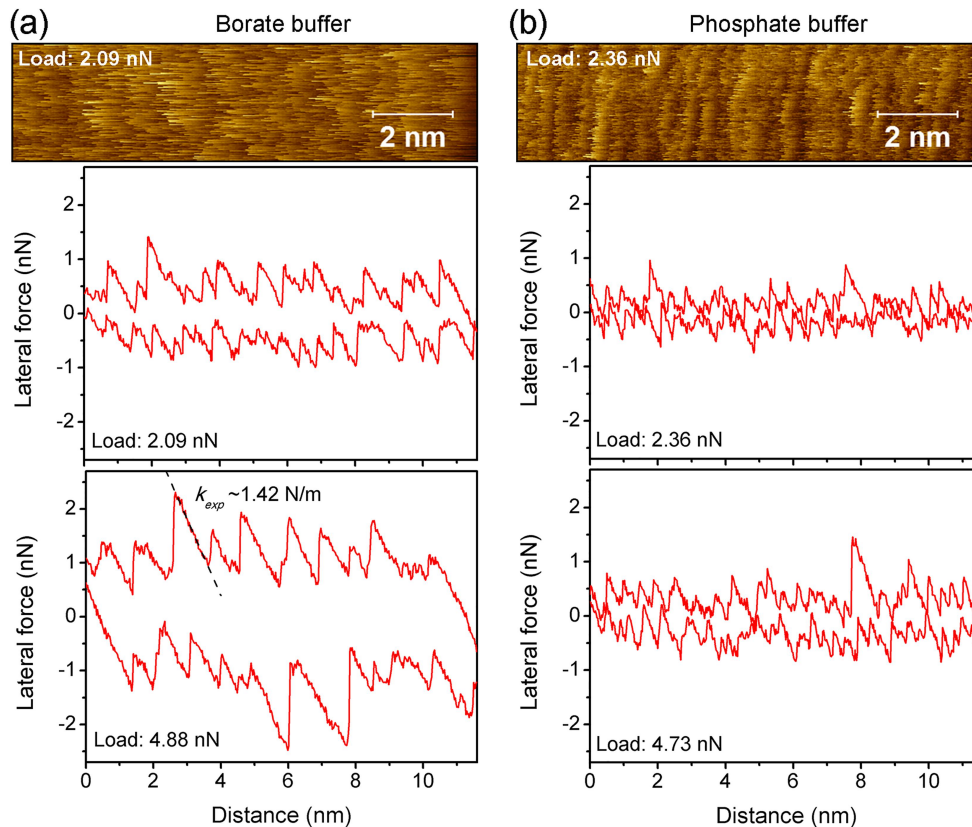


**Figure 4.2.2.** Friction loops acquired on ZrNiTi MG at two different normal loads: (a) in borate buffer; (b) in phosphate buffer. The typical retrace lateral force images in both solutions are shown, reflecting a stick-slip pattern.

**Figure 4.2.2** shows two typical lateral force images (retrace) in two solutions,

which reflect the stick-slip patterns. The images show similar positions of slip in adjacent scan lines, which proves that the stick-slip behavior follows the molecular-scale topographic features and is not just random. Friction loops at two different normal loads are also given in **Figure 4.2.2**, obtained from the line profile of the corresponding lateral force images. At a higher load, the hysteresis between the retrace and trace scans increases, i.e. the average lateral force and the dissipative energy increase with increasing load. All loops are comprising of irregular nanometer-scale stick-slip patterns. The passive oxide films formed during corrosion are mostly amorphous<sup>124,125</sup>. A similar observation of the irregular stick-slip friction was made on the corroded gold surface upon electrochemical oxidation<sup>72</sup> and various oxide surfaces in native conditions<sup>126</sup>. Therefore, we attribute this irregular stick-slip motion to the amorphous nature of corroded surfaces.

For the crystalline surface, the periodicity of the stick-slip pattern often corresponds to the spacing of one lattice site, which can be regarded as the basic slip unit. The slip over one lattice site is identified as “single slip”. Slip can also occur over an integer number of lattice sites, called “multiple slip”<sup>127,128,129</sup>. Here, we treat the slip over one basic slip unit on the amorphous surface as “single slip”. Local dense atomic packings, such as the icosahedral and crystal-like packing, known as the short- or medium-range order, were always found in the amorphous matrix and caused the intrinsic structural inhomogeneity of MGs at the nanoscale<sup>1,2</sup>. A small amount of nanocrystals were reported to be embedded in the amorphous passive films<sup>124,125</sup>. These ordered structures can form lattice-like sites similar with those in a crystal at

local positions of the amorphous surface, which change the basic slip units in these positions with different lengths. Therefore, on the amorphous surface, the size of basic slip units is not a single value but distributed over a range, which could be one reason for the distribution of the separations between slips (slip length). The stronger corrosion in borate buffer is expected to increase the crystallinity of the amorphous corroded surface<sup>125</sup>, resulting in a higher structural heterogeneity and thus a wider distribution of the basic slip length than in phosphate buffer.

We extracted the maximal lateral slip force,  $F_L^{max}$  (referred to as the slip force hereafter), the slip length,  $\Delta x$  and the experimental lateral contact stiffness,  $k_{exp}$  of slip events at all normal loads. **Figure 4.2.3a** and **b** show the average value of slip length,  $\langle \Delta x \rangle$ , and slip force,  $\langle F_L^{max} \rangle$ , as a function of load. In both solutions,  $\Delta x$  and  $F_L^{max}$  display a linear increase in the average value with load. As the load increases, more “multiple slip” events occur and the tip tends to slip over more basic slip units in one slip event, causing the increase in the average slip length. From **Figure 4.2.3a**,  $\langle \Delta x \rangle$  increases more significantly in borate buffer, indicating the occurrence of more and longer “multiple slip” events in borate buffer, compared to the phosphate buffer.  $\langle F_L^{max} \rangle$  also increases more significantly in borate buffer than in phosphate buffer, shown in **Figure 4.2.3b**.

The lateral contact stiffness between the tip and the sample surface is calculated as the slope of the lateral force versus the corresponding distance during each sticking phase<sup>130,131</sup> (see the lateral contact stiffness indicated as an example in **Figure 4.2.2a**):

$$k_{\text{exp}} = \frac{dF_L}{dx}, \quad (4.2.1)$$

**Figure 4.2.3c** shows the average value of these slopes,  $\langle k_{\text{exp}} \rangle$  at different normal loads. The contact stiffness is mainly determined by the nanometre-scale contact, therefore, is much weaker than the lateral force constant for the cantilever<sup>130</sup>.  $\langle k_{\text{exp}} \rangle$  is nearly constant and appears to weakly increase with increasing load, which is consistent with the observations in other works<sup>131,132</sup>. A significant increase in  $\langle k_{\text{exp}} \rangle$  was found only at high normal loads ( $\sim 40$  nN) caused by a sudden increase of the contact area<sup>131</sup>. In this work, due to the low applied load range, we conclude that there is only a small change in the contact.

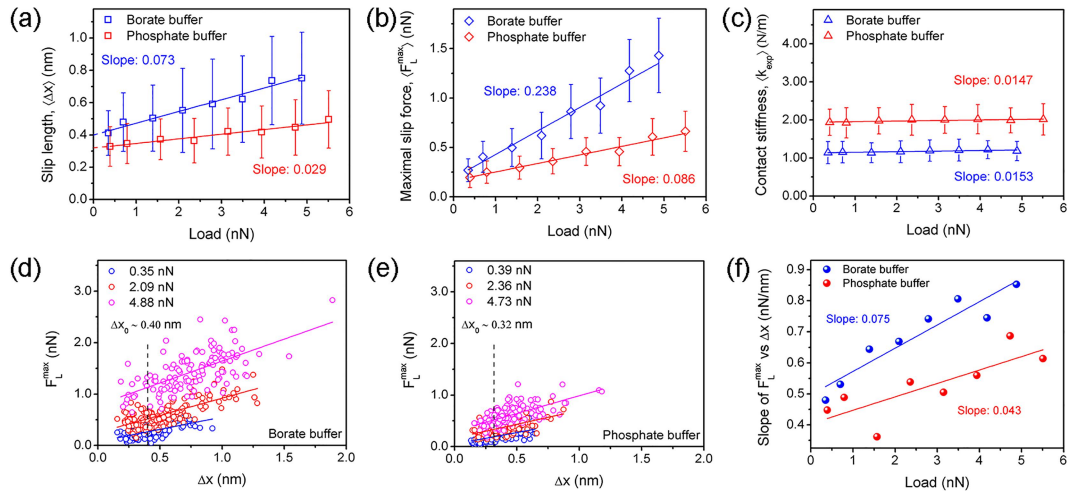


**Figure 4.2.3** The dependence on applied normal load of: (a) average slip length; (b) average value of maximal slip force; (c) average experimental contact stiffness. The contact stiffness depends weakly on the applied load (linear regression ANOVA test  $p < 0.014$ ,  $R = 0.78$  (borate buffer);  $p < 0.016$ ,  $R = 0.77$  (phosphate buffer)). Maximal lateral slip force vs the corresponding recorded length of slip events at different loads: (d) in borate buffer; (e) in phosphate buffer. (f) slopes of maximal slip force vs slip length in (d) and (e) as a function of load.

In order to see the connection between the slip force and slip length, **Figure**

**4.2.3d** and **e** plot  $F_L^{max}$  against the corresponding  $\Delta x$  in borate buffer and phosphate buffer. For both solutions and at all loads, the minimum slip lengths are similar, about 0.2 nm, the size of one single atom. For the amorphous surface, one single atom can be the basic slip unit. The maximum slip length can reach  $\sim 1.88$  nm at a high load of 4.88 nN in borate buffer, shown in **Figure 4.2.3d**. The slip occurs over a certain number of basic slip units, regarded as “multiple slip”. A strong correlation between the slip force and the slip length can be seen: the slip force increases approximately linearly with the slip length. Thus the larger increase in the slip length in borate buffer leads to the more significantly increased slip force than the phosphate buffer (**Figure 4.2.3b**). The slope of linear fit to the slip force versus slip length data (**Figure 4.2.3d** and **e**) is plotted against the normal load in **Figure 4.2.3f**. The slope increases more rapidly in borate buffer than that in phosphate buffer.

We will now discuss multiple slips on the amorphous surface. The Prandtl-Tomlinson (PT) model (see **Chapter 1.3.1**) is extensively used to explain atomic stick-slip friction behavior<sup>60</sup>, in which the surface is modeled as a series of periodically-arranged energy barriers that the tip must overcome as it slides over the surface. Medyanik et al.<sup>127</sup> has interpreted the transition between various stick-slip regimes for periodic surface potentials. Based on this method, we propose an analytical model to explain multiple slips on the amorphous surface.

In PT mode, the effective interaction potential  $U_{eff}$ , describing the friction system, contains two terms:

$$U_{eff} = U_{int} + U_{el} , \quad (4.2.2)$$

$$U_{int} = -U_0 \cos\left(\frac{2\pi x_{tip}}{a}\right), \quad (4.2.3)$$

$$U_{el} = \frac{1}{2} k_{eff} (x_{tip} - x_{el})^2 \quad (4.2.4)$$

where  $U_{int}$  is the corrugation potential of the tip-surface interaction,  $U_{el}$  is the elastic energy of the lateral spring,  $U_0$  is the corrugation energy amplitude,  $a$  is the lattice constant of the surface,  $k_{eff}$  is the effective lateral contact stiffness,  $x_{tip}$  is the tip position,  $x_{el}$  is the support position of the spring. localized energy minimums are with respect to the tip positions:  $\partial U_{eff} / \partial x_{tip} = 0$ , thus:

$$\frac{2\pi U_0}{a} \sin\left(\frac{2\pi x_{tip}}{a}\right) = -k_{eff} (x_{tip} - x_{el}), \quad (4.2.5)$$

where the left term corresponds to the interaction force,  $F_{int}$ , between the tip and the surface, and the right term corresponds to the elastic force of the spring,  $F_{el}$ .

**Figure 4.2.4** gives an example of transition between smooth sliding, single and double slip, which shows the interaction force,  $F_{int}$  of the sample surface. The tip “slip” occurs while the locally stable state ( $\partial^2 U_{eff} / \partial^2 x_{tip} > 0$ ) changing to unstable ( $\partial^2 U_{eff} / \partial^2 x_{tip} \leq 0$ ) states, until the tip “sticks” to a locally stable position. The number of available locally stable positions depends on the relation between  $k_{eff}$  and critical values  $k = k_i$  with respect to the elastic forces  $F_i = k_i(x_{el} - x_{tip})$ . The tip may slip over several stable positions, i.e. multiple slip. These critical stiffness values can

be calculated as<sup>127</sup>:

$$k_i = \left( \frac{2\pi}{a} \right)^2 U_0 k_i', \quad (4.2.6)$$

where  $k_i' = 1.0, 0.2172, \dots$  for  $i = 1, 2, \dots$ .  $k_1$  is the tangent of  $F_{int}$  in the position of first lattice site.

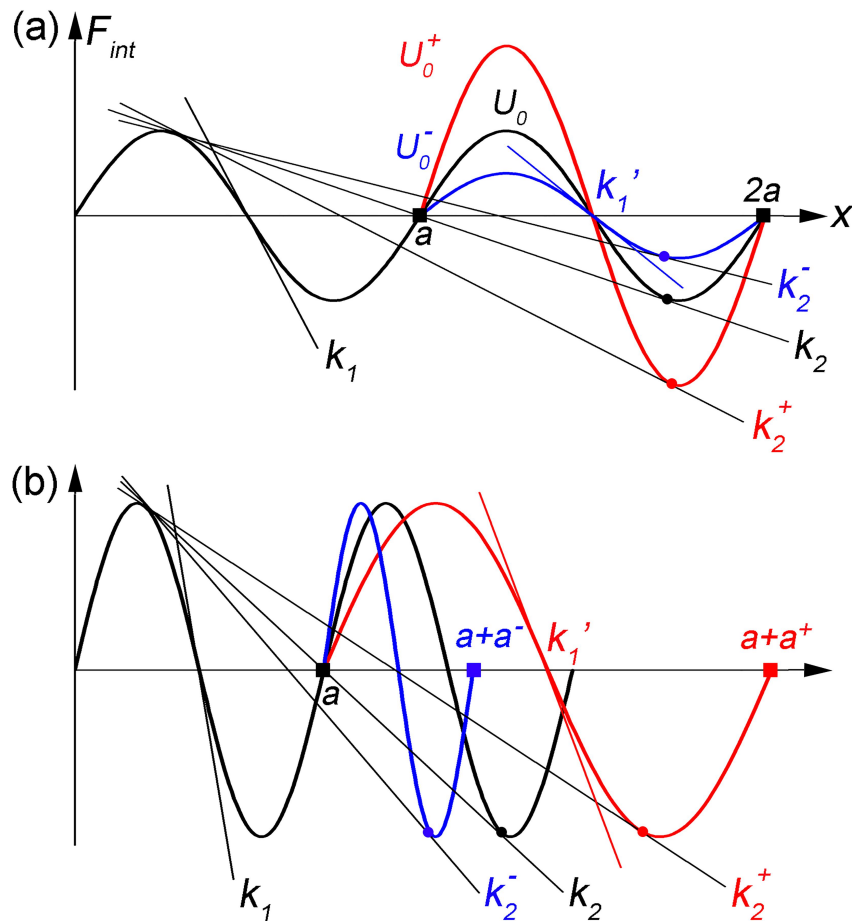


**Figure 4.2.4.** An explanation for transitions between different stick-slip regimes on the amorphous surface.  $F_{int}$  represents the tip-surface interaction force.  $U$ ,  $U^+$  and  $U^-$  represent the amplitude of the surface corrugation potential.  $a$ ,  $a^+$  and  $a^-$  represent the lattice constant.  $k_1$ ,  $k_1'$ ,  $k_2$ ,  $k_2^+$  and  $k_2^-$  are critical stiffness values for transitions between different stick-slip regimes.

- (1) When  $k_{eff} > k_1$ , the tip movement is continuous and no stick-slip occurs



(smooth sliding).

(2) When  $k_{eff} \leq k_1$ , the tip can slip to another available locally stable position.

Now we only consider the transition between single to double slip. For a periodic interaction potential, the next lattice site is still with spacing  $a$ . When  $k_{eff} > k_2$ , the tip can only slip to the second lattice (single slip).

(3) When  $k_{eff} \leq k_2$ , now the tip can directly jump two lattice sites (double slip).

For a amorphous surface, the corrugation energy amplitude  $U_0$  and the spacing  $a$  are the position dependent disordered parameters. We still follow the methodology in Eq.(4.2.2) to (4.2.4):

$$U_{\text{int}} = -U(x) \cos\left(\frac{2\pi x_{\text{tip}}}{a(x)}\right), \quad (4.2.7)$$

$$U(x) = U_0 + \delta U_0(x), \quad (4.2.8)$$

$$a(x) = a + \delta a(x) \quad (4.2.9)$$

where  $U_0$  is the average value of corrugation energy amplitudes, with the position dependent deviation  $\delta U_0(x)$ .  $a$  is the average value of lattice spacings with the position dependent deviation  $\delta a(x)$ . Therefore, in **Figure 4.2.4**, the corrugation energy and the spacing of second lattice site could be different from those of first site. For simplicity, we discuss the effects of  $U(x)$  and  $a(x)$  separately.

In **Figure 4.2.4a**, the corrugation energy of second lattice site is different from the

first site:

(1)  $U^+ > U$ , in this case, we can see  $k_2^+ > k_2$ . The tip is easier to slip over these two sites, i.e. double slip is more likely to occur.

(2)  $U^- < U$ , in this case,  $k_2^- < k_2$ . Double slip is more difficult to occur. In addition, the tangent  $k_1' < k_1$ . When  $k_2^- < k_{eff} < k_1$ , the tip slip to the second lattice. However, if  $k_{eff} > k_1'$ , this means a transition from a single slip to smooth sliding.

In **Figure 4.2.4b**, the lattice spacing of the second site is different from the first site:

(1)  $a^+ > a$ , in this case, we can see  $k_2^+ < k_2$ . Double slip is more difficult to occur. In addition, the tangent  $k_1' < k_1$ . When  $k_2^+ < k_{eff} < k_1$ , the tip slip to the second lattice. However, if  $k_{eff} > k_1'$ , this means a transition from a single slip to smooth sliding.

(2)  $a^- < a$ , in this case,  $k_2^- > k_2$ . double slip occur more easily.

The physical basis underlying transitions of other multiple slips (triple slip, quadruple slip and so on) is similar with the double slip described in **Figure 4.2.4**. Based on the discussion above, due to the irregular surface energy potential, there is a greater variation of critical stiffness values on the amorphous surface compared to the regular crystalline surface. For a given lateral spring constant  $k_{eff}$ , slips over several minima are sometimes more probably and sometimes less probable than for a regular periodic potential with a similar corrugation and periodicity. The transition between

smooth sliding to single slips and then multiple slip regimes on the crystalline surface usually depends on the applied load<sup>127,128,133</sup>. However, the criterium for the transition is also a position-dependent characteristic on the amorphous surface.

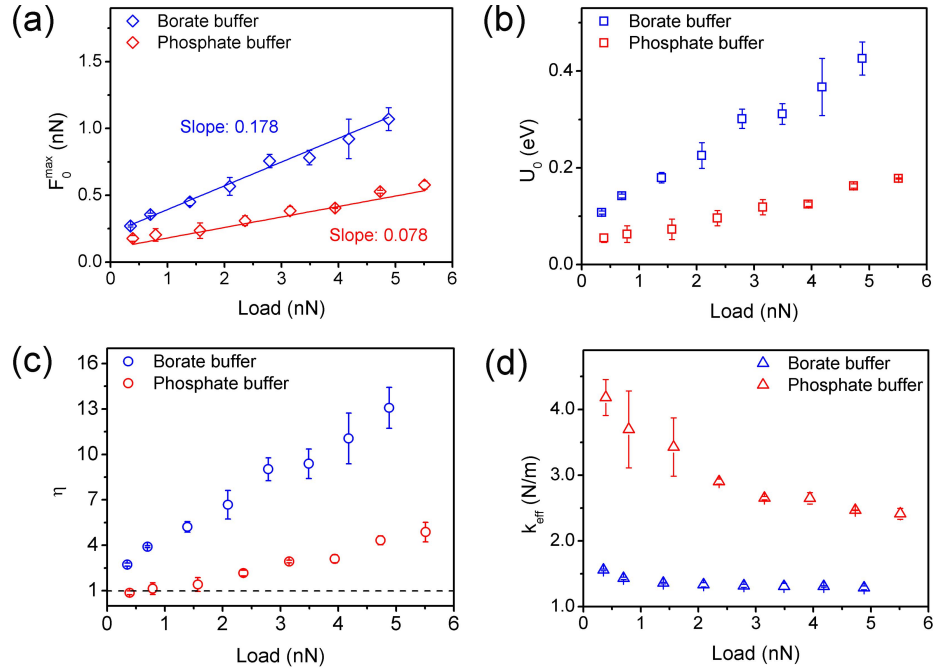


**Figure 4.2.5** The dependence on applied normal load of: (a) slip force corresponding to the single slips,  $F_0^{\max}$ ; (b) corrugation energy amplitude,  $U_0$ ; (c) PT parameter,  $\eta$ ; (d) effective contact stiffness,  $k_{eff}$ .

According to the explanation in **Figure 4.2.4**, the probability of multiple slips increases with a higher corrugation energy  $U_0$  and lower effective contact stiffness  $k_{eff}$ . The determination of  $U_0$  and  $k_{eff}$  in PT mode is based on a periodic interaction potential, which is not the case for our results. In order to estimate the difference in  $U_0$  and  $k_{eff}$  between the borate buffer and phosphate buffer, we assume that only single slips occur at zero load. The average value of slip length,  $\langle \Delta x \rangle$ , increases linearly with the load (**Figure 4.2.3a**). The basic slip length at zero load,  $\Delta x_0$ , can be obtained by extrapolating the fitting lines to zero load ( $\Delta x_0 \sim 0.40$  nm in borate buffer and  $\sim 0.32$

nm in phosphate buffer). The larger  $\Delta x_0$  in borate buffer agrees well with our previous inference that the stronger corrosion in borate buffer increases the crystallinity of the amorphous corroded surface and thus leads to a wider distribution of the basic slip length than in phosphate buffer. The corresponding slip force of single slips,  $F_0^{max}$ , can be calculated by the linear dependence of slip force on slip length (indicated in **Figure 4.2.3d** and **e**), as shown in **Figure 4.2.5a**. The slopes of slip force vs load in **Figure 4.2.3b** are larger than those in **Figure 4.2.5a** in both solutions due to the occurrence of multiple slips.

The corrugation energy amplitude can be calculated as<sup>131,133</sup>:

$$U_0 = \frac{F_0^{max} \cdot \Delta x_0}{2\pi}, \quad (4.2.10)$$

$U_0$  is strongly correlated with the applied load. As a result, The probability of multiple slips is increased at a higher load. The transitions from single to multiple slips with increasing load have been reported in other works<sup>127,128,134</sup>. Rivas et al.<sup>134</sup> reported a simulation study which predicted that higher values of  $U_0$  lead to longer jumps of the tip on amorphous surfaces. Thus, the increased slip length is observed with increasing the load (**Figure 4.2.3a**).  $U_0$  increases more significantly in borate buffer than in phosphate buffer (**Figure 4.2.5b**), indicating a higher corrugation energy in borate buffer. Agmon et al.<sup>135</sup> observed a higher corrugation energy of Fe–Al–O spinel catalyst compared to NaCl under identical conditions, due to the higher activity of the catalyst surface while NaCl is an inert material. In this work, the different chemical

activity of corroded surfaces can be expected in view of the different corrosion resistance of MGs in these two solutions. The higher chemical activity of the corroded surface in borate buffer contributes to the increase in corrugation energy. In borate buffer, the increased surface roughness caused by the more serious corrosion may also contributes to the higher corrugation energy, compared to the phosphate buffer.

A longer multiple slip tends to induce a higher slip force (**Figure 4.2.3c and d**). A larger lateral force is required when the tip jumps over more basic slip units in a slip event due to the higher energy barrier that the tip has to overcome. The slopes in **Figure 4.2.3c and d** represent the increase rate of corrugation energy. In borate buffer, the larger slope of the linear dependence on load (**Figure 4.2.3e**) indicates the more strongly increased corrugation energy compared to the phosphate buffer.

The effective lateral stiffness can be determined by the measured experimental stiffness through<sup>131,133</sup>:

$$k_{eff} = \left( 1 + \frac{1}{\eta} \right) \cdot k_{exp} , \quad (4.2.11)$$

$$\eta = \left( \frac{2\pi}{a} \right)^2 \frac{U_0}{k_{eff}} \quad (4.2.12)$$

$$\eta = \frac{2\pi F_0^{\max}}{\langle k_{exp} \rangle \cdot \Delta x_0} - 1 \quad (4.2.13)$$

The PT parameter  $\eta$  describes the relation between the corrugation energy and the

elastic energy of the contact (Eq. (4.2.12)). Different stick-slip regimes can be distinguished by the value of  $\eta$ , where the tip movement is continuous ( $\eta < 1$ ), presents the stick-slip motion with single slip ( $1 \leq \eta < 4.6$ ), or possibly with double slip ( $4.6 \leq \eta < 7.79$ ), triple slip ( $7.79 \leq \eta < 10.95$ ), or even longer multiple slip ( $\eta \geq 10.95$ )<sup>128,129</sup>. In PT mode, we can use the experimentally measured values to directly derive  $\eta$  according to Eq. (4.2.13), which is plotted against the applied load in **Figure 4.2.5c**. Roth et al. observed<sup>128</sup> more and longer multiple slips on a NaCl(001) surface accompanied by a larger  $\eta$  with increasing load. The value of  $\eta$  increases much stronger in borate buffer than that in phosphate buffer with the applied load. At the highest load, the value of  $\eta$  is  $\sim 13.07$  in borate buffer and  $\sim 4.87$  in phosphate buffer, indicating the increased probabilities of longer multiple slips in the former solution. The variation of  $\eta$  in two solutions is in good agreement with our experimental results (**Figure 4.2.3**).

**Figure 4.2.5d** presents the variation of effective lateral contact stiffness,  $k_{eff}$ , with the load. In phosphate buffer,  $k_{eff}$  shows a decrease with increasing the load and then approaches a stable value at high loads. For the borate buffer, we see only a slightly decreased  $k_{eff}$  in the beginning. At the lowest load of 0.39 nN in phosphate buffer, the value of  $\eta$  is  $\sim 1.0$ . Considering the large deviation of surface state on the amorphous surface,  $\eta$  is expected to be lower than 1.0 on many local positions, revealing a smooth sliding on these positions. As the load increases with a increased  $\eta$ , fewer positions experience smooth sliding. For the borate buffer, only at the low loads in the beginning, the smooth sliding would occur in some positions due to a larger value of  $\eta$ .

This trend of transition from smooth sliding to stick-slip friction agrees well with the variation of  $k_{eff}$ , which may be one of the reasons for the decrease in  $k_{eff}$ . The contact stiffness of smooth sliding is larger than that in stick-slip friction. The frictionless sliding was observed on the surface of W(011)<sup>136</sup> and graphite<sup>137</sup> due to the incommensurate contact between the tip and surface, and the commensurate contact caused a significant friction. In this work, the contact of the tip and surface in smooth sliding could be also different from that in stick-slip regimes, while the details are still unclear. However, the variation of the contact stiffness with load is still small in both solutions, which can be explained by that there is no significant change in the atomic structure or the area of the contact in this range of normal loads<sup>133</sup>. Thus, we conclude that the effect of the change in the contact is small in this work. More importantly,  $k_{eff}$  is also higher in phosphate buffer than that in borate buffer, similar with  $k_{exp}$  (**Figure 4.2.3c**). The difference in contact stiffness could be caused by the different surface properties in these two solutions: the surface in borate buffer might be softer due to corrosion.

As a summary, the corroded surface in borate buffer exhibits a higher corrugation energy than that in phosphate buffer. Meanwhile, the effective contact stiffness is higher in phosphate buffer than that in borate buffer. As mentioned before, the more serious corrosion in borate buffer increases the heterogeneity of the amorphous corroded surface. Consequently, a larger fluctuation of surface potential is expected and also leads to a higher probability of multiple slips in borate buffer than the phosphate buffer. Therefore, we can see the larger average value of slip length in

borate buffer.

### **4.2.3 Conclusion**

AFM friction experiments were performed on Zr-based metallic glasses in borate buffer and phosphate buffer to study the effect of corrosion on atomic-scale friction. An irregular stick-slip motion is observed and attributed to the amorphous nature of the corroded surfaces. We provide an approach to explain the irregular stick-slip motion within the framework of the Prandtl-Tomlinson model, which takes into account the disordered surface interaction potential. The approach captures transitions between smooth sliding, single and multiple slips, and gives helpful guidance to understand the atomic-scale friction on amorphous surfaces.

The friction coefficient of the corroded surface is larger in borate buffer than the phosphate buffer. In borate buffer, a higher surface corrugation energy, a lower effective contact stiffness and a higher structural heterogeneity causes the significant increase in the probability of multiple slips accompanied by larger slip forces than that in the phosphate buffer, which are attributed to the lower corrosion resistance of MGs in borate buffer.



### 4.3 Tribochemical Processes at High Loads

In previous chapters, all friction experiments were performed in a low-load regime. In engineering applications, mechanical components may be subject to harsh working conditions involving high load, which induce surface deformation and damage or displacement of materials, i.e. wear. Thus, the tribological properties of MGs at high loads should be investigated. The high-load friction experiments were performed with diamond tips because of their excellent hardness and wear-resistance.

#### 4.3.1 Experimental Details

All experiments were performed in 0.2 M phosphate buffer ( $\text{Na}_2\text{HPO}_4 + \text{NaH}_2\text{PO}_4$ , pH~7) and 0.2 M NaCl solution at room temperature. Friction experiments were started by immersing a new sample into the solution for 1 h equilibration and carried out with the diamond coated AFM tip (CDT-FMR, see **Chapter 2.6**). The AFM tip sliding velocity was  $8.0 \mu\text{m s}^{-1}$  and the scan field was  $1.0 \times 0.125 \mu\text{m}^2$ . Sixteen cycles of repetitive scans, each 64 scan lines, were performed in each scan field at a constant applied load and repeated on different surface areas with different loads, while the friction force was recorded.

#### 4.3.2 Results and Discussion

**Figure 4.3.1** displays the evolution of friction force on ZrNiTi MG in 0.2 M phosphate buffer with number of scan cycles at different applied loads. In previous chapters (see **Chapter 3** and **4.1**), we observed a decay of friction force with repeated

scanning in the low-load regime. Here, at higher loads, the friction force increases with number of scan cycles and then approaches a stable value.

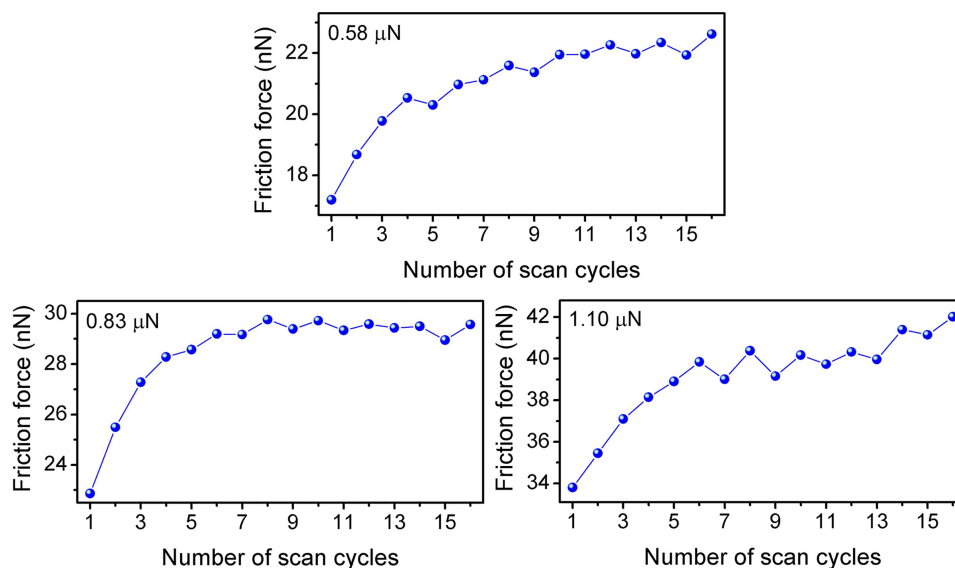


**Figure 4.3.1.** Friction force as a function of number of scan cycles on ZrNiTi MG in 0.2 M phosphate buffer for different normal loads indicated in the respective frames.

**Figure 4.3.2** shows the topography of the scan track and corresponding friction force images after 16 scan cycles in the central  $1.0 \times 0.125 \mu\text{m}^2$  region at an applied normal load of 20 nN. Friction is increased by a factor of about 1.3 within the central slide track compared to the surrounding area for all loads. However, the topography differs significantly after experiments at different loads. At a load of 0.58 μN, the slide track is difficult to distinguish in the topography, while there is strong contrast between the central and surrounding area in the friction signal. At a higher load of 1.10 μN, a topography with ridges and valleys distinguishes the slide track from the surrounding area. The line-scan height profile in **Figure 4.3.2c** reveals a pattern of ripples 0.4~0.8 nm high and ~50 nm apart. A similarly rippled topography has been

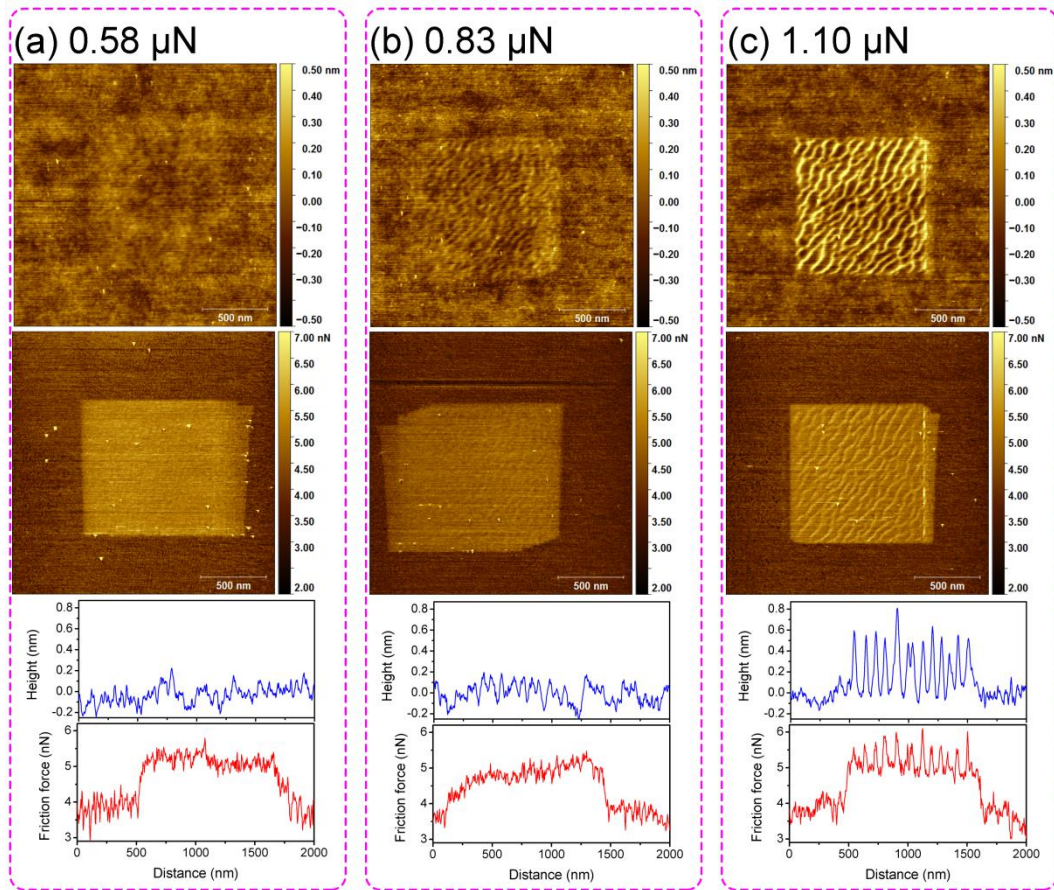


**Figure 4.3.2.** AFM topography and friction force images recorded on ZrNiTi MG in phosphate buffer after scanning the central area ( $1 \times 1 \mu\text{m}^2$ ) 16 times and the corresponding line profiles at a applied normal load: (a)  $0.58 \mu\text{N}$ ; (b)  $0.83 \mu\text{N}$ ; (c)  $1.10 \mu\text{N}$ . The imaging load is  $20 \text{ nN}$ .

reported for friction measurements on surfaces of different materials, such as metals<sup>138,139</sup>, ionic crystals<sup>140,141</sup> and polymers<sup>142</sup>. Several mechanisms have been suggested for the ripples formation: interplay between the developing surface corrugation and the frictional stress produced by the moving tip<sup>143,144</sup>, an erosion process induced by a periodic increase of the strain produced by the scanning tip<sup>141</sup> and others. There is no noticeable wear accompanying the ripples formation. Thus, we attribute it to surface deformation caused by mechanical interaction with the tip. The surface deformation is a load dependent process that cause the topographical

evolution from surface scanned at 0.58 to 1.10  $\mu\text{N}$ . Periodicity and amplitude of ripple patterns are affected by the size and shape of the scanning tip<sup>141,143</sup>.

This rippled topography exhibits a higher friction force, as revealed by the line-scan height and friction profiles in **Figure 4.3.2c**. However, topography is not the main factor for increased friction on the slide track. The track also shows a higher friction force than the surrounding area at the load of 0.58  $\mu\text{N}$ , where the topography is hardly changed by the scanning tip (**Figure 4.3.2a**). In previous chapters, we have shown that the growth of oxide film on the surface by electrochemical polarization (see **Chapter 3**) or immersion in corrosive solutions (see **Chapter 4.1**) increases friction. Tribofilms are known to form on tribologically stressed surfaces, as a result of complex mechanochemical interactions between surface materials and chemical components of surrounding environment, usually called “tribochemical reaction”. Gosvami et al.<sup>139</sup> reported a significant increase of friction force within the region of tribofilm growth compared to the surrounding iron oxide substrate and found that repeated sliding at sufficiently high loads leads to abundant tribochemical reactions and the associated nucleation and growth of tribofilms. Cai et al.<sup>145</sup> found that mechanical stimulation changes the reaction pathway with a lower activation energy for the corrosion of aluminum. Therefore, we conclude that the repeated scanning at a high applied load leads to the enhanced growth of the surface oxide film as a result of tribochemical reactions at the tip-sample interface and thereby increase the friction.

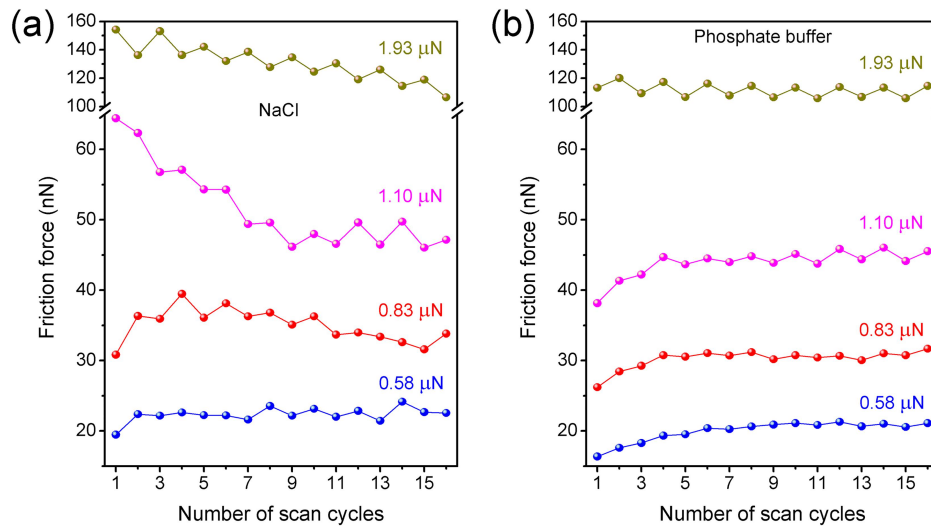


**Figure 4.3.3.** Friction force as a function of number of scan cycles on ZrNiTi MG in (a) NaCl solution and (b) phosphate buffer.

Now we will compare the results in NaCl solution and phosphate buffer at high loads. For all measurements shown below, we scan a smaller region  $1 \times 0.125 \mu\text{m}^2$ . **Figure 4.3.3a** shows the friction force on ZrNiTi MG in 0.2 M NaCl solution as a function of number of scan cycles at three different normal loads. Different from friction results in phosphate buffer (**Figure 4.3.1**), we see a transition from friction increase to friction decay with repeated scanning when the load is increased. At a load of  $0.58 \mu\text{N}$ , friction force increases with number of scan cycles. At a load of  $0.83 \mu\text{N}$ , the friction force first increases and then decreases with repeated scanning. When the load is  $1.10 \mu\text{N}$ , the friction force only decreases with repeated scanning. Friction results in phosphate buffer (**Figure 4.3.3b**) are similar with those obtained in large scan regions (**Figure 4.3.1**). At the load of  $0.58$  and  $0.83 \mu\text{N}$ , the friction values are similar in two solutions. However, at the load of  $1.10 \mu\text{N}$ , the initial value of friction in borate buffer becomes much higher than that in phosphate buffer.

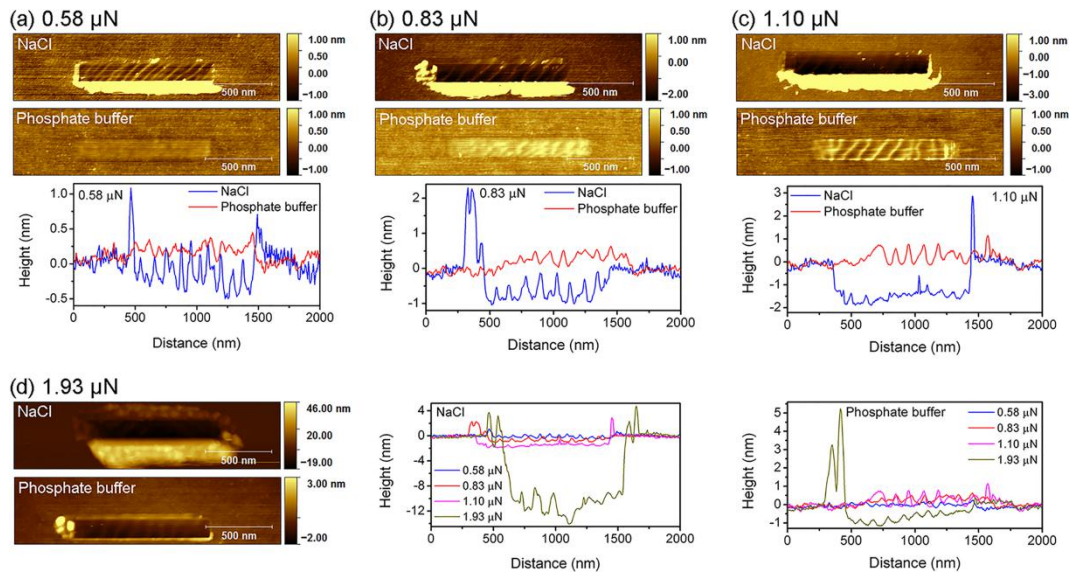


**Figure 4.3.4.** AFM topography images recorded on ZrNiTi MG in NaCl solution and phosphate buffer after scanning the central area ( $1 \times 0.125 \mu\text{m}^2$ ) 16 times and the corresponding line profiles at a normal load of (a) 0.58  $\mu\text{N}$ ; (b) 0.83  $\mu\text{N}$ ; (c) 1.10  $\mu\text{N}$ ; (d) 1.93  $\mu\text{N}$  in NaCl solution.

**Figure 4.3.4** presents AFM topography images of the slide tracks after 16 scan cycles in NaCl solution and phosphate buffer, corresponding to the friction results in **Figure 4.3.3**. In phosphate buffer, we see the rippled topography with the load increasing from 0.58  $\mu\text{N}$  to 1.10  $\mu\text{N}$ . Wear can be clearly observed with ploughing of material aside of the tracks in NaCl solution. At the load of 1.93  $\mu\text{N}$ , the depth of the wear track in NaCl solution is  $\sim 12.6$  nm, while the depth of the track is only  $\sim 1.0$  nm in phosphate buffer. ZrNiTi MG exhibits a higher corrosion resistance in phosphate buffer than that in NaCl solution (see **Chapter 4.1**). Corrosion in NaCl solution is governed by serious pitting, while the sample is passivated spontaneously in phosphate buffer. Therefore, we conclude that the more corrosive electrolyte significantly enhances the wear of MGs.

Mechanical stimulation reduces the activation energy for corrosion and enhances

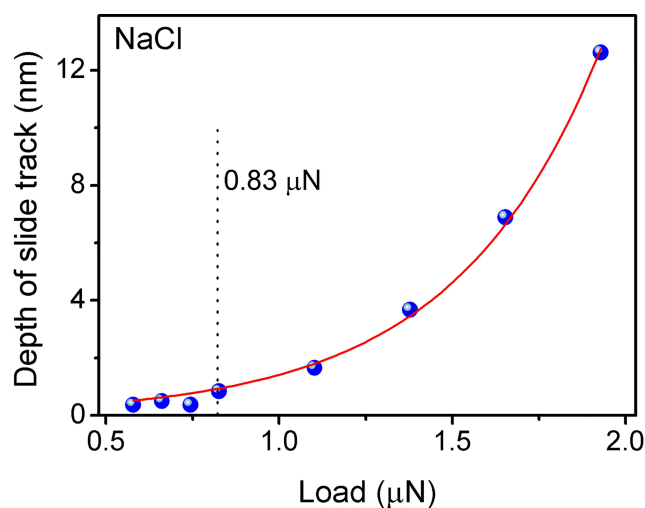


**Figure 4.3.5.** Depth of slide track as a function of the load applied to the AFM tip during 16 repetitive scans. The smooth curve is fit of the data to an exponential function.

corrosion under tribological load<sup>145</sup>. The friction results have shown that repeated scanning leads to the enhanced growth of the surface oxide film (**Figure 4.3.2**). The accelerated corrosion in NaCl solution results in a stronger dissolution, which is more likely to cause severe wear compared to the phosphate buffer. In **Chapter 4.2**, we found that the surface in borate buffer is softer than that in phosphate buffer. Similarly, a softer surface can be expected for the NaCl solution compared to the phosphate buffer. The oxide film formed in NaCl solution is then more susceptible to removal by the sliding tip. The depth of slide track after 16 repetitive scans in NaCl solution is plotted as a function of the applied normal load in **Figure 4.3.5**. The depth increases exponentially with the load. An exponentially increased rate of the tribochemical reaction with the applied stress has been reported<sup>132</sup>, which could be the reason for the increase in the depth of slide track. The wear in NaCl solution depends on the stress-assisted tribochemical reaction (tribochemical wear). When the load is lower than 0.83 μN, the depth is kept at a low value (< 1.0 nm). Ripples can be observed on



the bottom of the wear tracks. The tribo-oxidation is still the main friction process in these loads. Above the load of  $0.83 \mu\text{N}$ , the depth increases significantly. Here, we conclude that the tribochemical wear occurs from the load of  $0.83 \mu\text{N}$ . As shown in **Figure 4.3.3a**, the transition from friction increase to friction decay with repeated scanning can be seen at the load of  $0.83 \mu\text{N}$ . Therefore, the decay of friction with scanning in **Figure 4.3.3** should be due to the onset of wear in NaCl solution.

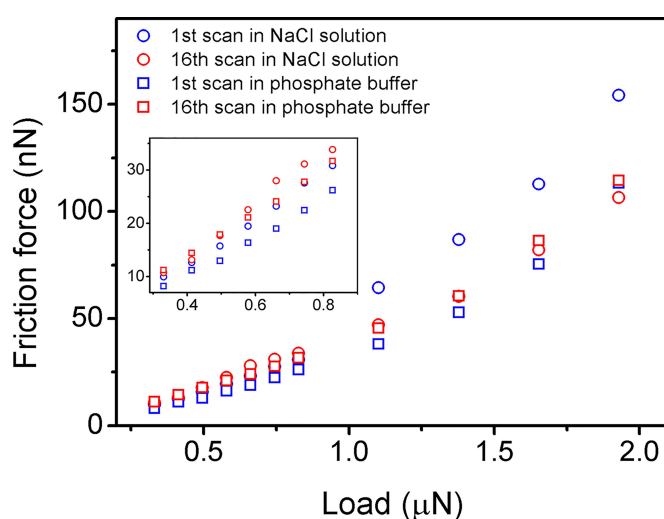


**Figure 4.3.6.** Friction force as a function of the load applied to the AFM tip at the first and last scan on ZrNiTi MG in 0.2 M NaCl solution and phosphate buffer.

Friction forces at the first and last scan are plotted against the load applied to the AFM tip on ZrNiTi MG in **Figure 4.3.6**. In phosphate buffer, the friction force at the first scan is always lower than that at the last scan, due to the tribo-oxidation. Only at the load of  $1.93 \mu\text{N}$ , the initial value of friction becomes very close to the final value, due to the weak wear in this case, revealed in **Figure 4.3.4d**. In NaCl solution, When the load is lower than  $0.83 \mu\text{N}$ , the lower initial value of friction forces can be seen, similar with those in phosphate buffer. After the onset of wear at the load of  $0.83 \mu\text{N}$ ,



the initial value of friction becomes higher than the final value and larger significantly than those in phosphate buffer. The increased friction force in wear regime is caused by the significantly increased contribution of plowing to friction<sup>67</sup>. A decreased wear rate with number of scans has been observed on the aluminum surface in NaCl solution<sup>145</sup>, indicating a decreased plowing depth with scanning. Therefore, the friction decay with number of scan cycles in wear regime can be understood as reduced plowing contribution.

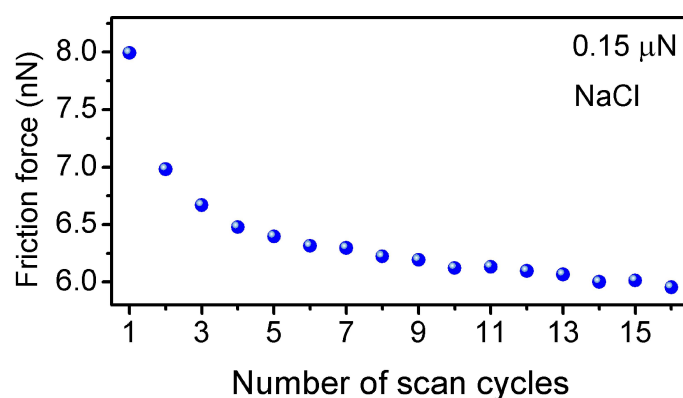


**Figure 4.3.7.** Friction force as a function of number of scan cycles on ZrNiTi MG in NaCl solution at a normal load of 0.15  $\mu\text{N}$ .

In order to confirm the existence of the phenomenon of friction decay described in previous chapters (see **Chapter 3** and **4.1**), **Figure 4.3.7** shows the friction force on ZrNiTi MG in 0.2 M NaCl solution as a function of number of scan cycles at a low applied load. Now the decay of friction force with number of scan cycles can be observed, which demonstrates that tribochemical reactions or tribo-oxidation induced by mechanical interaction can only occur at a sufficiently high load.

To summarize, **Figure 4.3.8** provides a schematic illustration of the

load-dependent friction processes:

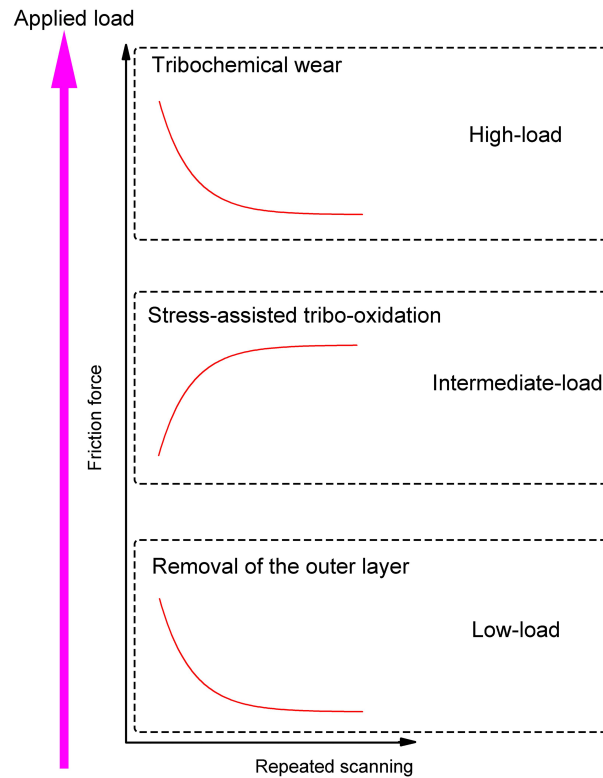


**Figure 4.3.8.** Schematic illustration of load-dependent friction processes on ZrNiTi MG in corrosive environments.

(1) Low-load regime: At a low load, no tribochemical reactions occur and the surface is in a natural corrosion state. The surface oxide film has a bilayer structure with a protective inner layer underlying a precipitated outer layer. This outer layer can be gradually removed during repeated scanning, resulting in a decay of the friction force with number of scan cycles towards a steady state, in which the tip slides on the stable inner layer. The growth of the outer layer, originating from the surface dissolution, depends on corrosion properties in corrosives environments.

(2) Intermediate-load regime: Mechanical stimulation leads to the enhanced growth of the surface oxide film as a result of tribochemical reactions or

tribo-oxidation at the tip-sample interface. Consequently, the friction force increases with repeated scanning. A surface deformation with formation of quasiperiodic ripples can also be observed which is attributed to mechanical interaction between the surface and the scanning tip. Friction in this regime is load-dependent and has no significant difference in different corrosive environments, in terms of the stability of the surface oxide film.

(3) High-load regime: Friction is high in this regime due to onset of wear. However, it decreases with repeated scanning, caused by a decreased wear rate with number of scans. The wear process strongly depends on the corrosive environment. More aggressive corrosive electrolytes significantly enhance the wear and thus leads to strong friction, which can be attributed to the accelerated dissolution.

### **4.3.3 Conclusion**

Nanoscale friction experiments on ZrNiTi MG in phosphate buffer and NaCl solution are performed with an increased applied normal load. Three different mechanisms can be identified for three different load regimes: removal of the outer layer of native oxide films in corrosive solutions at low load, stress-assisted tribo-oxidation and surface deformation in the intermediate-load regime, and tribochemical wear in the high-load regime. The tribo-oxidation leads to the enhanced growth of the surface oxide film and an increase of friction force with number of scans. The two solutions do not exhibit significant difference in friction due to the stability of the oxide film in this load regime. The tribochemical wear increases

friction and results in a friction decay with number of scans. The wear strongly depends on the corrosive electrolyte: the accelerated dissolution in NaCl solution significantly enhance the wear.

## Chapter 5: Conclusions and Outlook

### 5.1 Conclusions

Metallic glasses (MGs) have attracted widespread interest for their successful applications in micromechanical systems, where tribological performance of microcomponents involving mechanical contact is crucially important. In this thesis, nanotribological experiments are performed on MGs in corrosive solutions by means of an atomic force microscope (AFM). Our findings advance the understanding of microscopic mechanisms controlling friction and wear of MGs in corrosive environments. The main conclusions obtained in this thesis are summarized at a glance:

(1) We provided a new method to investigate *in situ* the structure of surface oxide films formed in corrosive environments using friction force microscopy. The oxide film has a bilayer structure with a mechanically stable inner layer underlying a mechanically unstable outer layer. The latter can be gradually removed during repeated scanning with the AFM tip, as evident from an exponential decay of friction force with number of scan cycles towards a steady state, in which the tip slides on the bare inner layer. The inner layer is identified with a compact protective layer, and the outer layer with a precipitated dissolution layer, which have been described in the literature of MG corrosion.

(2) Nanoscale friction was studied on oxidized surfaces of MGs after

potentiostatic polarization. The dependence of friction forces on the film-formation potential reveals the growth mechanism of the oxide film and highlights the role for the frictional response of MGs. At low polarization potentials, oxide growth and weak dissolution of the surface film lead to higher friction force on the rougher inner layer and significantly lower friction of the outer layer. At higher polarization potentials, the transpassive dissolution causes a rapid growth of the outer layer and a corresponding increase of its friction contribution.

(3) We investigated nanoscale friction on MGs upon immersion in corrosive solutions to elucidate the influence of corrosion on friction. The evolution of friction and adhesion with increasing immersion time in different solutions reveal the interrelation of the physicochemical processes of surface dissolution at the interfaces of the two layers and of friction on MGs. The competitive processes of metal cation dissolution and diffusion determine the accumulation of surface charge on the inner layer and thereby the adhesion. The competitive processes of hydrate formation at the outer layer and diffusion into solution determine the growth and thus the friction coefficient of the outer layer.

(4) We examined atomic-scale friction processes on MGs under corrosion conditions. An irregular stick-slip motion is observed and attributed to the amorphous nature of the corroded surfaces. A simple model based on the disordered surface interaction potential provides an explanation for the load dependence of slip lengths and general guidance to understand atomic-scale friction on amorphous surfaces. The

stronger corrosion leads to a significant increase in the probability of multiple slips accompanied by larger slip forces and thus a higher friction force on the corroded surface.

(5) High-load friction experiments were performed to study tribochemical processes. Beyond the removal of the outer oxide layer in low-load regime, we found two other processes at increasing load: stress-assisted tribo-oxidation in an intermediate load regime and tribochemical wear in the high-load regime. The tribo-oxidation leads to enhanced growth of the surface oxide film and thus an increase of friction force with scan repetitions. Tribochemical wear leads to strong initial plowing friction which decreases when the deepening wear track supports the load of the tip's slopes. The wear strongly depends on the corrosive electrolyte: the accelerated dissolution in a more aggressive electrolyte significantly enhances the wear.

## **5.2 Outlook**

(1) This work introduces methods to explore fundamental aspects of corrosion of MGs by nanoscale friction experiments. Understanding corrosion is of great importance for technological applications of MGs in micro-devices. Although the results are based on MGs, we suggest that the methods can be extended to the understanding of corrosion mechanisms in other metal and alloy systems. For example, friction force microscopy could be used to investigate surface oxide films on different phases of multiphase alloys and their growth in corrosive environments.

(2) In our experiments, the atomic-scale stick-slip friction on MGs was studied after immersing the samples into the solution for 1 h, but experiments at larger scale have demonstrated that friction force microscopy can reveal mechanism of oxide growth with time of polarization or immersion. Therefore, future investigations should analyze the microscopic mechanisms of electrochemical oxidation through measurements of frictional stick-slip motion.

(3) Friction experiments at high load led to tribo-oxidative stress and to tribochemical wear. It can be expected that the evolution of wear is accompanied by formation of a tribofilm, whose structure and chemical composition should be addressed in an extension of this works in order to elucidate the interplay of mechanical stress and electrochemical reactions on metallic glasses.



## References

1. Miracle, D. B., A structural model for metallic glasses. *Nature materials* **2004**, *3* (10), 697-702.
2. Sheng, H. W.; Luo, W. K.; Alamgir, F. M.; Bai, J. M.; Ma, E., Atomic packing and short-to-medium-range order in metallic glasses. *Nature* **2006**, *439* (7075), 419-25.
3. Jun., W. K.; Willens, R. H.; Duwez, P., Non-Crystalline structure in solidified gold-silicon. *Nature* **1960**, *187*, 869-870.
4. Chen, M., A brief overview of bulk metallic glasses. *NPG Asia Materials* **2011**, *3* (9), 82-90.
5. Inoue, A.; Takeuchi, A., Recent development and application products of bulk glassy alloys☆. *Acta Materialia* **2011**, *59* (6), 2243-2267.
6. Khan, M. M.; Nemati, A.; Rahman, Z. U.; Shah, U. H.; Asgar, H.; Haider, W., Recent Advancements in Bulk Metallic Glasses and Their Applications: A Review. *Critical Reviews in Solid State and Materials Sciences* **2017**, *43* (3), 233-268.
7. Johnson, W. L., Bulk glass-forming metallic alloys Science and technology. *MRS Bulletin* **1999**, *24* (10), 42-56.
8. Inoue, A.; Shen, B. L.; Chang, C. T., Super-high strength of over 4000 MPa for Fe-based bulk glassy alloys in  $[(\text{Fe}_{1-x}\text{Co}_x)_{0.75}\text{B}_{0.2}\text{Si}_{0.05}]_{96}\text{Nb}_4$  system. *Acta Materialia* **2004**, *52* (14), 4093-4099.
9. Trexler, M. M.; Thadhani, N. N., Mechanical properties of bulk metallic glasses. *Progress in Materials Science* **2010**, *55* (8), 759-839.
10. Eckert, J.; He, G.; Zhang, Z. F.; Löser, W., Fracture-Induced Melting in Glassy and Nanostructured Composite Materials. *Journal of Metastable and Nanocrystalline Materials* **2004**, *20-21*, 357-365.

11. Wang, W. H., The elastic properties, elastic models and elastic perspectives of metallic glasses. *Progress in Materials Science* **2012**, *57* (3), 487-656.
12. Duarte, M. J.; Klemm, J.; Klemm, S. O.; Mayrhofer, K. J. J.; Stratmann, M.; Borodin, S.; Romero, A. H.; Madinehei, M.; Crespo, D.; Serrano, J.; Gerst, S. S. A.; Choi, P. P.; Raabe, D.; Renner, F. U., Element-Resolved Corrosion Analysis of Stainless-Type Glass-Forming Steels. *Science* **2013**, *341*, 372-376.
13. Si, J. J.; Chen, X. H.; Cai, Y. H.; Wu, Y. D.; Wang, T.; Hui, X. H., Corrosion behavior of Cr-based bulk metallic glasses in hydrochloric acid solutions. *Corrosion Science* **2016**, *107*, 123-132.
14. Greer, A. L.; Rutherford, K. L.; Hutchings, I. M., Wear resistance of amorphous alloys and related materials. *International Materials Reviews* **2013**, *47* (2), 87-112.
15. Shen, T. D.; Schwarz, R. B., Bulk ferromagnetic glasses in the Fe-Ni-P-B system. *Acta Materialia* **2001**, *49*, 837-847.
16. Herzer, G., Modern soft magnets: Amorphous and nanocrystalline materials. *Acta Materialia* **2013**, *61* (3), 718-734.
17. Greer, A. L., Metallic Glasses. *Science* **1995**, *267*, 1947-1953.
18. Bulatov, V.; Abraham, F. F.; Kubin, L.; Devincere, B.; Yip, S., Connecting atomistic and mesoscale simulations of crystal plasticity. *Nature* **1998**, *391*, 669-672.
19. Weinberger, C. R.; Cai, W., Surface-controlled dislocation multiplication in metal micropillars. *Proceedings of the National Academy of Sciences* **2008**, *105* (38), 14304-14307.
20. Chen, H.; Het, Y.; Shiflet, G. J.; Poon, S. J., Deformation-induced nanocrystal formation in shear bands of amorphous alloys. *Nature* **1994**, *367*, 541-543.
21. Zhang, Z. F.; He, G.; Eckert, J.; Schultz, L., Fracture mechanisms in bulk metallic glassy materials. *Physical review letters* **2003**, *91* (4), 045505.

22. Schuh, C.; Hufnagel, T.; Ramamurty, U., Mechanical behavior of amorphous alloys. *Acta Materialia* **2007**, *55* (12), 4067-4109.
23. Bei, H.; Xie, S.; George, E. P., Softening caused by profuse shear banding in a bulk metallic glass. *Physical review letters* **2006**, *96* (10), 105503.
24. Xie, S.; George, E. P., Hardness and shear band evolution in bulk metallic glasses after plastic deformation and annealing. *Acta Materialia* **2008**, *56* (18), 5202-5213.
25. Yoo, B.-G.; Park, K.-W.; Lee, J.-C.; Ramamurty, U.; Jang, J.-i., Role of free volume in strain softening of as-cast and annealed bulk metallic glass. *Journal of Materials Research* **2011**, *24* (4), 1405-1416.
26. Narayan, R. L.; Singh, P. S.; Hofmann, D. C.; Hutchinson, N.; Flores, K. M.; Ramamurty, U., On the microstructure–tensile property correlations in bulk metallic glass matrix composites with crystalline dendrites. *Acta Materialia* **2012**, *60* (13-14), 5089-5100.
27. Zhang, Y.; Wang, W. H.; Greer, A. L., Making metallic glasses plastic by control of residual stress. *Nature materials* **2006**, *5* (11), 857-60.
28. Scudino, S.; Surreddi, K. B.; Khoshkhoo, M. S.; Sakaliyska, M.; Wang, G.; Eckert, J., Improved Room Temperature Plasticity of Zr<sub>41.2</sub>Ti<sub>13.8</sub>Cu<sub>12.5</sub>Ni<sub>10</sub>Be<sub>22.5</sub> Bulk Metallic Glass by Channel-Die Compression. *Advanced Engineering Materials* **2010**, *12* (11), 1123-1126.
29. Cao, Q. P.; Liu, J. W.; Yang, K. J.; Xu, F.; Yao, Z. Q.; Minkow, A.; Fecht, H. J.; Ivanisenko, J.; Chen, L. Y.; Wang, X. D.; Qu, S. X.; Jiang, J. Z., Effect of pre-existing shear bands on the tensile mechanical properties of a bulk metallic glass. *Acta Materialia* **2010**, *58* (4), 1276-1292.
30. Joshi, S. S.; Katakam, S.; Singh Arora, H.; Mukherjee, S.; Dahotre, N. B., Amorphous Coatings and Surfaces on Structural Materials. *Critical Reviews in Solid State and Materials Sciences* **2015**, *41* (1), 1-46.

31. Saotome, Y.; Okaniwa, S.; Kimura, H.; Inoue, A., Superplastic Nanoforging of Pt-Based Metallic Glass with Dies of Zr-BMG and Glassy Carbon Fabricated by Focused Ion Beam. *Materials Science Forum* **2007**, 539-543, 2088-2093.
32. Kumar, G.; Desai, A.; Schroers, J., Bulk metallic glass: the smaller the better. *Adv Mater* **2011**, 23 (4), 461-76.
33. Lin, Y.-C.; Tsai, Y.-C.; Ono, T.; Liu, P.; Esashi, M.; Gessner, T.; Chen, M., Metallic Glass as a Mechanical Material for Microscanners. *Advanced Functional Materials* **2015**, 25 (35), 5677-5682.
34. Kumar, G.; Tang, H. X.; Schroers, J., Nanomoulding with amorphous metals. *Nature* **2009**, 457 (7231), 868-72.
35. Schroers, J.; Nguyen, T.; O’Keeffe, S.; Desai, A., Thermoplastic forming of bulk metallic glass—Applications for MEMS and microstructure fabrication. *Materials Science and Engineering: A* **2007**, 449-451, 898-902.
36. Shi, Y., Size-dependent mechanical responses of metallic glasses. *International Materials Reviews* **2018**, 64 (3), 163-180.
37. Guo, H.; Yan, P. F.; Wang, Y. B.; Tan, J.; Zhang, Z. F.; Sui, M. L.; Ma, E., Tensile ductility and necking of metallic glass. *Nature materials* **2007**, 6 (10), 735-9.
38. Jang, D. C.; Greer, J. R., Transition from a strong-yet-brittle to a stronger-and-ductile state by size reduction of metallic glasses. *Nature Materials* **2010**, 9, 215-219.
39. Li, Y.; Ng, S.C.; Ong, C.K.; Hng, H.H.; Goh, T.T., Glass forming ability of bulk glass forming alloys. *Scruta Materialia* **1991**, 36. 783-787.
40. Nieh, T.; Wadsworth, J., Homogeneous deformation of bulk metallic glasses. *Scruta Materialia* **2006**, 54 (3), 387-392.

41. Duan G.; Wiest, A.; Lind, M. L.; Li, J.; Rhim, W. K.; Johnson, W. L., Bulk Metallic Glass with Benchmark Thermoplastic Processability. *Adv. Mater.* **2007**, *19*, 4272-4275.
42. Hu, Q.; Fu, M. W.; Zeng, X. R., Thermostability and thermoplastic formability of  $(\text{Zr}_{65}\text{Cu}_{17.5}\text{Ni}_{10}\text{Al}_{7.5})_{100-x}\text{RE}_x$  ( $x=0.25-3.25$ , RE: Y, Gd, Tb, Dy, Ho, Er, Tm, Yb, Lu) bulk metallic glasses. *Materials & Design* **2014**, *64*, 301-306.
43. McCafferty, E., Introduction to Corrosion Science. Springer 2010.
44. Wang, D. P.; Wang, S. L.; Wang, J. Q., Relationship between amorphous structure and corrosion behaviour in a Zr–Ni metallic glass. *Corrosion Science* **2012**, *59*, 88-95.
45. Macdonald, D. D., The Point Defect Model for the Passive State. *Journal of the Electrochemical Society* **1992**, *139*, 3434.
46. Scherer, J.; Ocko, B. M.; Magnussen, O. M., Structure, dissolution, and passivation of Ni(111) electrodes in sulfuric acid solution: an in situ STM, X-ray scattering, and electrochemical study. *Electrochimica Acta* **2003**, *48* (9), 1169-1191.
47. Sennour, M.; Marchetti, L.; Martin, F.; Perrin, S.; Molins, R.; Pijolat, M., A detailed TEM and SEM study of Ni-base alloys oxide scales formed in primary conditions of pressurized water reactor. *Journal of Nuclear Materials* **2010**, *402* (2-3), 147-156.
48. Luo, H.; Dong, C. F.; Xiao, K.; Li, X. G., Characterization of passive film on 2205 duplex stainless steel in sodium thiosulphate solution. *Applied Surface Science* **2011**, *258* (1), 631-639.
49. Maurice, V.; Peng, H.; Klein, L. H.; Seyeux, A.; Zanna, S.; Marcus, P., Effects of molybdenum on the composition and nanoscale morphology of passivated austenitic stainless steel surfaces. *Faraday discussions* **2015**, *180*, 151-70.

50. Långberg, M.; Örnek, C.; Evertsson, J.; Harlow, G. S.; Linpé, W.; Rullik, L.; Carlà, F.; Felici, R.; Bettini, E.; Kivisäkk, U.; Lundgren, E.; Pan, J., Redefining passivity breakdown of super duplex stainless steel by electrochemical operando synchrotron near surface X-ray analyses. *npj Materials Degradation* **2019**, *3* (1).
51. Li, Y.; Macdonald, D. D.; Yang, J.; Qiu, J.; Wang, S., Point defect model for the corrosion of steels in supercritical water: Part I, film growth kinetics. *Corrosion Science* **2020**, *163*, 108280.
52. Song, Q.-T.; Xu, J., (TiZrNbTa)<sub>90</sub>Mo<sub>10</sub> high-entropy alloy: Electrochemical behavior and passive film characterization under exposure to Ringer's solution. *Corrosion Science* **2020**, *167*, 108513.
53. Wang, Y.; Jiang, S. L.; Zheng, Y. G.; Ke, W.; Sun, W. H.; Wang, J. Q., Electrochemical behaviour of Fe-based metallic glasses in acidic and neutral solutions. *Corrosion Science* **2012**, *63*, 159-173.
54. Kawashima, A.; Ohmura, K.; Yokoyama, Y.; Inoue, A., The corrosion behaviour of Zr-based bulk metallic glasses in 0.5M NaCl solution. *Corrosion Science* **2011**, *53* (9), 2778-2784.
55. The area of contact between stationary and moving surfaces. *Proceedings of the Royal Society of London. Series A. Mathematical and Physical Sciences* **1997**, *169* (938), 391-413.
56. Zhou, L. X., Mechanisms Controlling Friction and Adhesion at the Atomic Length-Scale **2015** Publicly Accessible Penn Dissertations. 1086.
57. Szlufarska, I.; Chandross, M.; Carpick, R. W., Recent advances in single-asperity nanotribology. *Journal of Physics D: Applied Physics* **2008**, *41* (12), 123001.
58. Butt, H.-J.; Cappella, B.; Kappl, M., Force measurements with the atomic force microscope: Technique, interpretation and applications. *Surface Science Reports* **2005**, *59* (1-6), 1-152.

59. Gnecco, E.; Bennewitz, R.; Gyalog, T.; Loppacher, Ch.; Bammerlin, M.; Meyer, E.; Güntherodt, H. J., Velocity Dependence of Atomic Friction. *Physical review letters* **2000**, *84*, 1172.
60. Popov, V. L.; Gray, J. A. T., Prandtl-Tomlinson Model: A Simple Model Which Made History. **2014**, *1*, 153-168.
61. Tian, P.; Khun, N. W.; Tor, S. B.; Liu, E.; Tian, Y., Tribological behavior of Zr-based bulk metallic glass sliding against polymer, ceramic, and metal materials. *Intermetallics* **2015**, *61*, 1-8.
62. Li, Y. C.; Zhang, C.; Xing, W.; Guo, S. F.; Liu, L., Design of Fe-Based Bulk Metallic Glasses with Improved Wear Resistance. *ACS applied materials & interfaces* **2018**, *10* (49), 43144-43155.
63. Jiang, X.; Song, J.; Fan, H.; Su, Y.; Zhang, Y.; Hu, L., Sliding friction and wear mechanisms of Cu<sub>36</sub>Zr<sub>48</sub>Ag<sub>8</sub>Al<sub>8</sub> bulk metallic glass under different sliding conditions: dry sliding, deionized water, and NaOH corrosive solutions. *Tribology International* **2020**, *146*, 106211.
64. Togashi, N.; Ishida, M.; Nishiyama, N.; Inoue, A., Wear resistance of metallic glass bearings. *Reviews on Advanced Materials Science* **2008**, *18*, 93-97.
65. Caron, A.; Louzguine-Luzguin, D. V.; Bennewitz, R., Structure vs chemistry: friction and wear of Pt-based metallic surfaces. *ACS applied materials & interfaces* **2013**, *5* (21), 11341-7.
66. Zhao, Y. Y.; Ye, Y. X.; Liu, C. Z.; Feng, R.; Yao, K. F.; Nieh, T. G., Tribological behavior of an amorphous Zr<sub>20</sub>Ti<sub>20</sub>Cu<sub>20</sub>Ni<sub>20</sub>Be<sub>20</sub> high-entropy alloy studied using a nanoscratch technique. *Intermetallics* **2019**, *113*, 106561.
67. Kang, S. J.; Rittgen, K. T.; Kwan, S. G.; Park, H. W.; Bennewitz, R.; Caron, A., Importance of surface oxide for the tribology of a Zr-based metallic glass. *Friction* **2017**, *5* (1), 115-122.

68. Louzguine-Luzgin, D. V.; Ito, M.; Ketov, S. V.; Trifonov, A. S.; Jiang, J.; Chen, C. L.; Nakajima, K., Exceptionally high nanoscale wear resistance of a  $\text{Cu}_{47}\text{Zr}_{45}\text{Al}_8$  metallic glass with native and artificially grown oxide. *Intermetallics* **2018**, *93*, 312-317.
69. Caron, A.; Sharma, P.; Shluger, A.; Fecht, H. J.; Louzguine-Luzguin, D. V.; Inoue, A., Effect of surface oxidation on the nm-scale wear behavior of a metallic glass. *Journal of Applied Physics* **2011**, *109* (8), 083515.
70. Caron, A.; Qin, C. L.; Gu, L.; Gonzalez, S.; Shluger, A.; Fecht, H.-J.; Louzguine-Luzguin, D. V.; Inoue, A., Structure and nano-mechanical characteristics of surface oxide layers on a metallic glass. *Nanotechnology* **2011**, *22*, 095704.
71. Zhang, M.; Yao, D.; Cao, Z.; Li, P.; Zhou, P.; Wang, X., Influence of oxidation on the performance of  $\text{Zr}_{55}\text{Cu}_{30}\text{Al}_{10}\text{Ni}_5$  BMG. *Intermetallics* **2016**, *79*, 20-27.
72. Labuda, A.; Hausen, F.; Gosvami, N. N.; Grutter, P. H.; Lennox, R. B.; Bennowitz, R., Switching atomic friction by electrochemical oxidation. *Langmuir* **2011**, *27* (6), 2561-6.
73. Hausen, F.; Zimmet, J. A.; Bennowitz, R., Surface structures and frictional properties of Au(100) in an electrochemical environment. *Surface Science* **2013**, *607*, 20-24.
74. Argibay, N.; Sawyer, W. G., Frictional Voltammetry with Copper. *Tribology Letters* **2012**, *46* (3), 337-342.
75. Shockley, J. M.; Horton, D. J.; Wahl, K. J., Effect of aging of 2507 super duplex stainless steel on sliding tribocorrosion in chloride solution. *Wear* **2017**, *380-381*, 251-259.
76. Meyer, E.; Hug, H. J.; Bennowitz, R., Scanning probe microscopy: The Lab on a Tip (Springer, 2004) pp. 46-49.



77. Sweeney, J.; Hausen, F.; Hayes, R.; Webber, G. B.; Endres, F.; Rutland, M. W.; Bennewitz, R.; Atkin, R., Control of nanoscale friction on gold in an ionic liquid by a potential-dependent ionic lubricant layer. *Physical review letters* **2012**, *109* (15), 155502.
78. Rapuc, A.; Simonovic, K.; Huminiuc, T.; Cavaleiro, A.; Polcar, T., Nanotribological Investigation of Sliding Properties of Transition Metal Dichalcogenide Thin Film Coatings. *ACS applied materials & interfaces* **2020**.
79. Binnig, G.; Quate, C. F.; Gerber, C., Atomic force microscope. *Physical review letters* **1986**, *56* (9), 930-933.
80. Lang, S. Y.; Shi, Y.; Guo, Y. G.; Wang, D.; Wen, R.; Wan, L. J., Insight into the Interfacial Process and Mechanism in Lithium-Sulfur Batteries: An In Situ AFM Study. *Angewandte Chemie* **2016**, *55* (51), 15835-15839.
81. Rubio-Sierra, F.J.; Heck, W.M.; Stark, R.W., Nanomanipulation by Atomic Force Microscopy. *Advanced Engineering Materials* **2005**, *7*, 4.
82. Tseng, A. A.; Notargiacomo, A.; Chen, T. P., Nanofabrication by scanning probe microscope lithography: A review. *Journal of Vacuum Science & Technology B* **2005**, *23* (3), 877.
83. Jalili, N.; Laxminarayana, K., A review of atomic force microscopy imaging systems: application to molecular metrology and biological sciences. *Mechatronics* **2004**, *14* (8), 907-945.
84. Bao, G.; Suresh, S., Cell and molecular mechanics of biological materials. *Nature Materials* **2003**, *2*, 715–725.
85. Kada, G.; Kienberger, F.; Hinterdorfer, P., Atomic force microscopy in bionanotechnology. *Nano Today* **2008**, *3* (1-2), 12-19.

86. Sader, J. E.; Chon, J. W. M.; Mulvaney, P., Calibration of rectangular atomic force microscope cantilevers. *Review of Scientific Instruments* **1999**, *70* (10), 3967-3969.
87. Herzer, G., Modern soft magnets: Amorphous and nanocrystalline materials. *Acta Materialia* **2013**, *61*, 718–734..
88. Liu, Y. H.; Wang, D.; Nakajima, K.; Zhang, W.; Hirata, A.; Nishi, T.; Inoue, A.; Chen, M. W., Characterization of nanoscale mechanical heterogeneity in a metallic glass by dynamic force microscopy. *Physical review letters* **2011**, *106* (12), 125504.
89. Garcia, R.; Gomez, C. J.; Martinez, N. F.; Patil, S.; Dietz, C.; Magerle, R., Identification of nanoscale dissipation processes by dynamic atomic force microscopy. *Physical review letters* **2006**, *97* (1), 016103.
90. Macdonald, D. D., The Point Defect Model for the Passive State. *Journal of The Electrochemical Society* **2019**, *139* (12), 3434-3449.
91. Jiang, Z.; Dai, X.; Middleton, H., Investigation on passivity of titanium under steady-state conditions in acidic solutions. *Materials Chemistry and Physics* **2011**, *126* (3), 859-865.
92. Macdonald, D. D., Passivity: enabler of our metals based civilisation. *Corrosion Engineering, Science and Technology* **2014**, *49* (2), 143-155.
93. Karayan, A. I.; Maya-Visuet, E.; Castaneda, H., Transpassivity characterization of the alloy UNS N08367 in a chloride-containing solution. *Journal of Solid State Electrochemistry* **2014**, *18* (11), 3191-3202.
94. Ma, H. R.; Chen, X. Y.; Li, J. W.; Chang, C. T.; Wang, G.; Li, H.; Wang, X. M.; Li, R. W., Fe-based amorphous coating with high corrosion and wear resistance. *Surface Engineering* **2016**, 1-7.

95. Schwarz, U. D.; Zwörner, O.; Köster, P.; Wiesendanger, R., Quantitative analysis of the frictional properties of solid materials at low loads. I. Carbon compounds. *Physical Review B* **1997**, *56*, 6997..
96. Skal, S.; Kerroum, Y.; Guenbour, A.; Bellaouchou, A.; Tabyaoui, H.; Idrissi, H.; Zarrouk. A.; García-Antón, J., Effect of abrasive particles on electrochemical behaviour of passive film. *Journal of Materials and Environmental Sciences* **2017**, *8* (9), 3234-3246..
97. Rodríguez, M. n. A.; Carranza, R. M., Properties of the Passive Film on Alloy 22 in Chloride Solutions Obtained by Electrochemical Impedance. *Journal of The Electrochemical Society* **2011**, *158* (6), C221.
98. Sato, N., Surface oxides affecting metallic corrosion. *Corrosion Science and Technology* **2001**, *31* (4), 265-274.
99. Sato, N., Surface oxides affecting metallic corrosion. *Corrosion Science and Technology* **2001**, *31* (4), 265-274.
100. Gregori, J.; García-Jareño, J. J.; Giménez-Romero, D.; Vicente, F., Effect of Anions and Oxygen on the Kinetics of the Anodic Dissolution of Nickel. *Journal of The Electrochemical Society* **2006**, *153* (6), B206.
101. Ha, H.-Y.; Kwon, H.-S., Effects of pH Levels on the Surface Charge and Pitting Corrosion Resistance of Fe. *Journal of The Electrochemical Society* **2012**, *159* (9), C416-C421.
102. Kumar, N.; Andersson, M. P.; van den Ende, D.; Mugele, F.; Siretanu, I., Probing the Surface Charge on the Basal Planes of Kaolinite Particles with High-Resolution Atomic Force Microscopy. *Langmuir* **2017**, *33* (50), 14226-14237.
103. Guo, Y.; Siretanu, I.; Zhang, Y.; Mei, B.; Li, X.; Mugele, F.; Huang, H.; Mul, G., pH-Dependence in facet-selective photo-deposition of metals and metal oxides on semiconductor particles. *Journal of Materials Chemistry A* **2018**, *6* (17), 7500-7508.

104. Dong, Z. H.; Shi, W.; Zhang, G. A.; Guo, X. P., The role of inhibitors on the repassivation of pitting corrosion of carbon steel in synthetic carbonated concrete pore solution. *Electrochimica Acta* **2011**, *56* (17), 5890-5897.
105. Jing, D.; Pan, Y.; Li, D.; Zhao, X.; Bhushan, B., Effect of Surface Charge on the Nanofriction and Its Velocity Dependence in an Electrolyte Based on Lateral Force Microscopy. *Langmuir* **2017**, *33* (8), 1792-1798.
106. de Wijn, A. S.; Fasolino, A.; Filippov, A. E.; Urbakh, M., Nanoscopic friction under electrochemical control. *Physical review letters* **2014**, *112* (5), 055502.
107. Podgaynyy, N.; Wezislá, S.; Molls, C.; Iqbal, S.; Baltruschat, H., Stick-slip behaviour on Au(111) with adsorption of copper and sulfate. *Beilstein journal of nanotechnology* **2015**, *6*, 820-30.
108. Soltis, J., Passivity breakdown, pit initiation and propagation of pits in metallic materials – Review. *Corrosion Science* **2015**, *90*, 5-22.
109. Díez-Pérez, I.; Gorostiza, P.; Sanz, F.; Müller, C., First Stages of Electrochemical Growth of the Passive Film on Iron. *Journal of The Electrochemical Society* **2001**, *148* (8), B307.
110. Zhang, S. D.; Liu, Z. W.; Wang, Z. M.; Wang, J. Q., In situ EC-AFM study of the effect of nanocrystals on the passivation and pit initiation in an Al-based metallic glass. *Corrosion Science* **2014**, *83*, 111-123.
111. Green, B. A.; Steward, R. V.; Kim, I.; Choi, C. K.; Liaw, P. K.; Kihm, K. D.; Yokoyama, Y., In situ observation of pitting corrosion of the Zr50Cu40Al10 bulk metallic glass. *Intermetallics* **2009**, *17* (7), 568-571.
112. Zhang, C.; Chan, K. C.; Wu, Y.; Liu, L., Pitting initiation in Fe-based amorphous coatings. *Acta Materialia* **2012**, *60* (10), 4152-4159.

113. Ma, H. R.; Li, J. W.; Chang, C. T.; Wang, X. M.; Li, R. W., Passivation Behavior of Fe-Based Amorphous Coatings Prepared by High-Velocity Air/Oxygen Fuel Processes. *Journal of Thermal Spray Technology* **2017**.
114. Wang, Y. M.; Zhang, C.; Liu, Y.; Chan, K. C.; Liu, L., Why does pitting preferentially occur on shear bands in bulk metallic glasses? *Intermetallics* **2013**, *42*, 107-111.
115. Li, W.; Li, D. Y., Influence of surface morphology on corrosion and electronic behavior. *Acta Materialia* **2006**, *54* (2), 445-452.
116. Reffass, M.; Sabot, R.; Jeannin, M.; Berziou, C.; Refait, P., Effects of phosphate species on localised corrosion of steel in NaHCO<sub>3</sub>+NaCl electrolytes. *Electrochimica Acta* **2009**, *54* (18), 4389-4396.
117. Yohai, L.; Schreiner, W.; Vázquez, M.; Valcarce, M. B., Phosphate ions as effective inhibitors for carbon steel in carbonated solutions contaminated with chloride ions. *Electrochimica Acta* **2016**, *202*, 231-242.
118. Liu, J.-C.; Park, S.; Nagao, S.; Nogi, M.; Koga, H.; Ma, J.-S.; Zhang, G.; Sugauma, K., The role of Zn precipitates and Cl<sup>-</sup> anions in pitting corrosion of Sn–Zn solder alloys. *Corrosion Science* **2015**, *92*, 263-271.
119. Boudellioua, H.; Hamlaoui, Y.; Tifouti, L.; Pedraza, F., Effects of polyethylene glycol (PEG) on the corrosion inhibition of mild steel by cerium nitrate in chloride solution. *Applied Surface Science* **2019**, *473*, 449-460.
120. Macdonald, D. D., The history of the Point Defect Model for the passive state: A brief review of film growth aspects. *Electrochimica Acta* **2011**, *56* (4), 1761-1772.
121. BenSalah, M.; Sabot, R.; Triki, E.; Dhouibi, L.; Refait, P.; Jeannin, M., Passivity of Sanicro28 (UNS N-08028) stainless steel in polluted phosphoric acid at different temperatures studied by electrochemical impedance spectroscopy and Mott–Schottky analysis. *Corrosion Science* **2014**, *86*, 61-70.

122. Choudhary, L.; Wang, W.; Alfantazi, A., Electrochemical Corrosion of Stainless Steel in Thiosulfate Solutions Relevant to Gold Leaching. *Metallurgical and Materials Transactions A* **2015**, *47* (1), 314-325.
123. Wang, X.; Wang, B.; Zhang, L.; Yang, C.; Yang, Y., Effect of Different Welding Processes on Electrochemical and Corrosion Behavior of Pure Nickel in 1 M NaCl Solution. *Metals* **2017**, *7* (12), 532.
124. Zhang, B.; Wang, J.; Wu, B.; Guo, X. W.; Wang, Y. J.; Chen, D.; Zhang, Y. C.; Du, K.; Oguzie, E. E.; X. L. Ma, X. L., Unmasking chloride attack on the passive film of metals. *Nature communications* **2018**, *9*, 2559.
125. Örnek, C.; Långberg, M.; Evertsson, J.; Harlow, G.; Linpé, W.; Rullik, L.; Carlà, F.; Felici, R.; Kivisäkk, U.; Lundgren, E.; Pan, J., Influence of Surface Strain on Passive Film Formation of Duplex Stainless Steel and Its Degradation in Corrosive Environment. *Journal of The Electrochemical Society* **2019**, *166* (11), C3071-C3080.
126. Craciun, A. D.; Gallani, J. L.; Rastei, M. V., Stochastic stick-slip nanoscale friction on oxide surfaces. *Nanotechnology* **2016**, *27* (5), 055402.
127. Medyanik, S. N.; Liu, W. K.; Sung, I. H.; Carpick, R. W., Predictions and observations of multiple slip modes in atomic-scale friction. *Physical review letters* **2006**, *97* (13), 136106.
128. Roth, R.; Glatzel, T.; Steiner, P.; Gnecco, E.; Baratoff, A.; Meyer, E., Multiple Slips in Atomic-Scale Friction: An Indicator for the Lateral Contact Damping. *Tribology Letters* **2010**, *39* (1), 63-69.
129. Counts, I.; Gangloff, D.; Bylinskii, A.; Hur, J.; Islam, R.; Vuletic, V., Multislip Friction with a Single Ion. *Physical review letters* **2017**, *119* (4), 043601.
130. Carpick, R. W.; Ogletree, D. F.; Salmeron, M., Lateral stiffness: A new nanomechanical measurement for the determination of shear strengths with friction force microscopy. *Applied Physics Letters* **1997**, *70* (12), 1548-1550.

131. Skuratovsky, S.; Agmon, L.; Berkovich, R., Comparative Study of Dimensionality and Symmetry Breaking on Nanoscale Friction in the Prandtl–Tomlinson Model with Varying Effective Stiffness. *Tribology Letters* **2020**, *68* (4).
132. Ptak, F.; Almeida, C. M.; Prioli, R., Velocity-dependent friction enhances tribomechanical differences between monolayer and multilayer graphene. *Scientific reports* **2019**, *9* (1), 14555.
133. Socoliuc, A.; Bennewitz, R.; Gnecco, E.; Meyer, E., Transition from stick-slip to continuous sliding in atomic friction: entering a new regime of ultralow friction. *Physical review letters* **2004**, *92* (13), 134301.
134. Rivas, A. M. F.; Zamora, R. R. M.; Prioli, R., Lateral force microscopy profiles for amorphous potentials. *Ultramicroscopy* **2003**, *97* (1-4), 315-320.
135. Agmon, L.; Shahar, I.; Birodker, B.-E.; Skuratovsky, S.; Jopp, J.; Berkovich, R., Application of Static Disorder Approach to Friction Force Microscopy of Catalyst Nanoparticles to Estimate Corrugation Energy Amplitudes. *The Journal of Physical Chemistry C* **2019**, *123* (5), 3032-3038.
136. Motohisa, H.; Kazumasa S.; Reizo K.; Yoshitada M., Observation of Superlubricity by Scanning Tunneling Microscopy. *Physical review letters* **1997**, *78*, 1448.
137. Dienwiebel, M.; Verhoeven, G. S.; Pradeep, N.; Frenken, J. W.; Heimberg, J. A.; Zandbergen, H. W., Superlubricity of graphite. *Physical review letters* **2004**, *92* (12), 126101.
138. Pendergast, M. E.; Volinsky, A. A.; Pang, X. L., Pattern Formation During Nanowear of Gold Films. *Materials Research Society Symposium Proceedings* **2007**, 1059.

139. Gosvami, N. N.; Bares, J. A.; Mangolini, F.; Konicek, A. R.; Yablon, D. G.; Carpick, R. W., Mechanisms of antiwear tribofilm growth revealed in situ by single-asperity sliding contacts. *Science* **2015**, *348*, 102-106.
140. Bennewitz, R.; Dickinson, J.T., Fundamental Studies of Nanometer-Scale Wear Mechanisms. *MRS Bulletin* **2008**, *33*, 1174 - 1180.
141. Socoliuc, A.; Gnecco, E.; Bennewitz, R.; Meyer, E., Ripple formation induced in localized abrasion. *Physical Review B* **2003**, *68* (11).
142. Gnecco, E.; Riedo, E.; King, W. P.; Marder, S. R.; Szoszkiewicz, R., Linear ripples and traveling circular ripples produced on polymers by thermal AFM probes. *Physical Review B* **2009**, *79* (23).
143. Filippov, A. E.; Popov, V. L.; Urbakh, M., Mechanism of wear and ripple formation induced by the mechanical action of an atomic force microscope tip. *Physical review letters* **2011**, *106* (2), 025502.
144. Yu, J.; Kim, S. H.; Yu, B.; Qian, L.; Zhou, Z., Role of tribochemistry in nanowear of single-crystalline silicon. *ACS applied materials & interfaces* **2012**, *4* (3), 1585-93.
145. Cai, M.; Langford, S. C.; Dickinson, J. T., Tribochemical wear of single crystal aluminum in NaCl solution studied by atomic force microscopy. *Journal of Applied Physics* **2011**, *110* (6), 063509.



## Acknowledgments

I would like to acknowledge all the people who supported me during this PhD work.

This thesis is completed under the guidance of Prof. Dr. Roland Bennewitz. Thanks to my supervisor for helping me develop my research ideas during my doctoral period and make the experiments proceed smoothly. His rigorous and serious attitude towards research, innovative scientific accomplishment and open-minded life style impressed and inspired me.

The continuous support of the project by Prof. Dr. Eduard Arzt is gratefully acknowledged.

A large part of AFM experiments were completed with the help of Dr. Gunther Kramer in our group. I sincerely thank Gunther for his guidance and help in AFM operation and data analysis.

Special thanks to Laurent Marot, Ernst Meyer, and Peter Reimann (*University of Basel*) for generously providing the metallic glass samples.

I would like to thank my teammates in “Interactive Surfaces” group for the friendly atmosphere: Dr. Johanna Blass, Bartosz Henryk Szczefanowicz, Kordula Schellnhuber and the former colleagues: Dr. Kai Thomas Rittgen, Dr. Riad Sahli, Dr. Xianqiang Pei, Dr. Novaf Ozgun and Dr. Arzu Colak.

I am grateful to the technical staff in INM for XRD and SEM characterization, Rudolf Karos, Dr. Marcus Koch and Aude Haettich. I would also like to thank the administrative staff, Sabine Müller for her help with administrative requirements during my PhD studies and my life in Saarbrücken. In addition, thanks to the entire INM for this pleasant time.

Thanks to the financial support from China Scholarship Council (CSC) and German Academic Exchange Service (DAAD).

## **Personal Resume**

**MA, HAORAN**

---

### **Personal Information**

Date of Birth: 1991.2.8                      Nationality: China              Phone: +49 17635967004

Gender: Male                                      Email: haoran.ma@leibniz-inm.de

Address: Hofweg 127, 66125 Saarbrücken, Germany

### **Education**

- 2016.10-Present, Doctoral Candidate  
Saarland University, Germany  
Major in Materials Science and Engineering  
Interactive Surfaces group, INM – Leibniz Institute for New Materials
- 2013.9-2016.7, Master Degree  
Shanghai University, China (joint training with Ningbo Institute of Materials Technology and Engineering, Chinese Academy of Sciences )  
Major in Materials Science and Engineering
- 2009.9-2013.7, Bachelor Degree  
Central South University, China  
Major in Materials Science and Engineering

### **Research topic**

Tribology and corrosion of metals, specific topics:

- Nanotribology on metallic glasses in corrosive solutions using an electrochemical atomic force microscope
- Corrosion and wear properties of Fe-based amorphous coatings

## **Publications**

1. **Ma HR**, Bennewitz R. Nanoscale friction and growth of surface oxides on a metallic glass under electrochemical polarization. *Tribology International* **2021**, *158*, 106925.
2. **Ma HR**, Li JW, Jiao J, Chang CT, Wang G, et al. Passivation behavior of Fe-based amorphous coatings prepared by high-velocity air/oxygen fuel processes, *Journal of Thermal Spray Technology* **2017**, *26*, 2040-2047
3. **Ma HR**, Chen XY, Li JW, Chang CT, Wang G, et al. Fe-based amorphous coatings with high corrosion and wear resistance, *Surface Engineering* **2017**, *33*(1), 56-62
4. **Ma HR**, Li JW, Jiao J, Chang CT, Wang G, et al. Wear resistance of Fe-based amorphous coatings prepared by AC-HVAF and HVOF, *Materials Science and Technology* **2017**, *33*(1), 65-71